Universitat Politècnica de Catalunya

Path Integral Monte Carlo and Bose-Einstein condensation in quantum fluids and solids

Ph.D. thesis by

Riccardo Rota

Thesis Advisor: Prof. Jordi Boronat

Departament de Física i Enginyeria Nuclear

October 13, 2011

Contents

Chapter 1

Introduction

Bose-Einstein condensation (BEC) is a quantum phenomenon in which the lowest energy single-particle state of a quantum many-body system becomes, below a certain temperature, macroscopically occupied. The occurrence of such a peculiar behavior has been predicted in 1924 by Satyendra Nath Bose and Albert Einstein in the study of the thermodynamic properties of a noninteracting gas of particles obeying Bose statistics.

Although this behavior, at first, was thought to be a pathology of the ideal gas, which would disappear as soon as an interatomic potential is taken into account, the hypothesis that BEC could appear also in strongly interacting systems such as quantum liquids was formulated by London in 1938, after the experimental discovery of superfluidity in liquid helium. In the same year, Allen and Misener in Cambridge [1] and Kapitza in Moscow [2] measured the resistance to the flow of liquid ^{4}He clamped in narrow channels and subjected to a pressure drop. They found that, below a characteristic temperature $T_\lambda \simeq 2.17$ K, ^{4}He flows so easily that it cannot be described in terms of conventional viscosity: after this evidence, Kapitza introduced for the first time the term "superfluidity" to refer to this anomalous behavior.

To describe this effect, Tisza proposed the so called "two-fluid" model: he suggested that below T_λ liquid ^{4}He could be described by a fluid in which a fraction of the system, namely the superfluid component, behaves completely without friction, while the rest of the liquid, defined the normal component, behaves qualitatively as a normal liquid. To give an explanation of the Tisza's phenomenological model, London pointed out that ^{4}He atoms, having total spin $S = 0$, obey Bose statistics and, thus, he associated the observed transition at T_λ to the occurrence of BEC, suggesting that the superfluid component is constituted by the atoms occupying the lowest energy single-particle state.

In opposition to London's conjecture, Landau proposed another explanation of the superfluidity phenomenon introducing the notion of "quasiparticle", that is an excitation of the system from the ground state characterized by a definite energy and momentum. Making use of this concept (and without recalling explicitly the idea of BEC), he postulated that in the two-fluid model the superfluid component represents the liquid which remains in its ground state, while the normal component can be seen as a fluid of quasiparticles: at very low temperature, if the velocity of the system is not sufficiently high to excite a quasiparticle, the system remains in its ground state and is able to flow without dissipation.

The most important work to solve the controversy between London's and Landau's hypothesis was made by Bogoliubov in 1947. He studied a Bose gas with

weak repulsive interaction making the assumption that it would undergo BEC, and showed that the low energy excitations for this system are collective modes with a non-zero velocity. This means that, as a weak interaction is turned on in a Bose system presenting BEC, the excited states can be described in terms of the "quasi-particles" conjectured in the Landau's description of the superfluid phase.

Some years later, Penrose and Onsager proposed a generalization of the concept of BEC applicable to interacting systems, thus also to liquid ^{4}He. They considered the eigenvalues of the one-body density matrix $\rho_1(r)$ in the limit of r going to infinity, indicating that these eigenvalues correspond to the occupation of the various eigenstates of the whole liquid. BEC is present whenever one of these eigenvalues, namely N_0, is comparable with the total number N of atoms in the liquid. In other words, BEC is present if the fraction $n_0 = N_0/N$, usually indicated as the condensate fraction, is finite in the thermodynamic limit.

Nowadays, there is a general consensus that superfluidity in a bulk liquid has to be seen as a consequence of BEC. Even if the first London's conjecture of associating the condensate fraction to the superfluid one has proven wrong (superfluid fraction, that is the fraction of the liquid which does not respond to the movements of the walls of its vessel, is almost 1 for liquid ^{4}He at zero temperature, but the condensate fraction is only about 8%), many evidences point out that superfluid effects in liquid ^{4}He are accompanied by a non-zero condensate fraction.

However, the connection between superfluidity and BEC is still now a matter of debate and study. The experimental evidences pointing out the existence of a condensate in the superfluid phase of ^{4}He are only indirect. The condensate fraction n_0 can be inferred from deep inelastic neutron scattering experiments, but its measurement depends on the assumption that a condensate exists in the ground state and also on the particular shape of the distribution function for the excited states with non-zero momentum [3]. From the theoretical point of view, accurate estimations of the one-body density matrix are accessible. In particular, microscopic simulations based on realistic interatomic potentials represent a powerful method of investigation of quantum fluids and provide values of n_0 for liquid ^{4}He at saturated vapor pressure in nice agreement with experimental results [4, 5, 6, 7]. For these reasons, the liquid phase of ^{4}He is still now a topic of big interest in condensed matter physics and important efforts are required, both theoretically and experimentally, to give a complete description of its BEC properties over all the range of temperatures and pressures for which the superfluid phase is stable.

Nevertheless, the present understanding of superfluidity in condensed (i.e. non gaseous) systems comes from the study of liquid helium, because no other condensed Bose system is known to become superfluid below a certain temperature. To give a deeper insight on superfluidity and on the occurrence of BEC in quantum liquids, it is fundamental to investigate other systems than liquid helium. Among condensed systems, the most plausible candidate for superfluidity is molecular para-hydrogen (pH$_2$) because its small mass should in principle enhance the zero-point effects up to rather large temperatures, in comparison with other elements [8]. However, the temperature at which BEC is expected to appear in pH$_2$ is lower than the triple point

and the superfluid transition is hindered by the appearance of the crystalline phase. Several attempts to metastabilize liquid $p\mathrm{H}_2$ down to low temperature have been made but none of them has proven to be successful in reaching the temperatures estimated for the superfluid transition [9]. The interest in this topic is kept alive by the evidences of some anomalies in small clusters of $p\mathrm{H}_2$ pointing out a superfluid behavior [10]. An investigation of non crystalline states in $p\mathrm{H}_2$ at low temperature is possible through microscopic simulations. These numerical studies are aimed to understand whether $p\mathrm{H}_2$ can present BEC or not and, eventually, which are the condition for BEC to appears, with particular interest in the estimation of the transition temperature to a superfluid phase.

Another intriguing question that is far from a complete answer concerns the interplay between superfluidity and crystallization. The possibility that atoms can flow without dissipation even inside a rigid crystalline structure, although being counterintuitive, has been proposed more than forty years ago [11, 12, 13]. A similar behavior, which cannot occur in classical solids where atoms are well localized around their lattice positions, is not in principle prohibited in quantum solids where the atoms can be delocalized on distances comparable with the interatomic separation and thus where the indistinguishability of the particles plays a fundamental role. The best example of quantum solid can be found in the crystalline phase of helium, which is stable only if the sample at low temperature is subjected to an external pressure higher than 25 bar. The interest in the properties of an eventual supersolid phase, that is a state of matter characterized at the same time by superfluidity and crystalline order, has gained a huge interest in the last years, after the experimental evidence of non classical rotational inertia effects in solid ^{4}He below temperatures of the order of 100 mK [14, 15]. However, even if this behavior has been detected in other experiments, the data reported are often controversial and their interpretation is a delicate issue. Many theoretical models have been proposed so far for solid ^{4}He, but none of them has been able to reproduce all the experimental findings.

Performing a theoretical study of quantum fluids and solids, with the objective of investigating their BEC and their superfluid properties, is not an easy task. Perturbative approaches, often used in the study of many-body systems, reveal themselves useless for this purpose because of the strong correlations between the atoms arising from the interatomic interaction and from the quantum nature of the system. Thus, microscopic simulations appear as one of the most powerful theoretical tools to provide a reliable description of these phenomena. In particular, Monte Carlo methods are very appropriate to deal with this topic, especially for their generality and for their huge versatility which allow to apply them in a wide set of many-body problems.

The development of Monte Carlo techniques aimed at the study of condensed ^{4}He has a long history. McMillan in 1965 was the first in calculating the properties of helium by means of Variational Monte Carlo [16], making use of the many-body wave function suggested by Jastrow which considers only pair correlation. Later on,

the variational results have been improved in more accurate computational methods, in which it is possible to control the approximation and give, in principle, exact estimation for the ground state properties of quantum systems. Among these methods, we can mention the Green's-function Monte Carlo and the Diffusion Monte Carlo [17].

Nowadays, it is becoming particularly relevant, in the simulation of quantum fluids and solids, the Path Integral Monte Carlo method [18]. Within this approach, it is possible to map the quantum system onto a classical model of interacting polymers, which can be considered as the ring exchanges of bosons in imaginary time, and thus to give easily a classical picture for superfluidity. Thanks to this isomorphism, the quantum system can be simulated by means of conventional Monte Carlo methods. The definition of the effective potential acting on the classical system of polymers is completely specified by the Hamiltonian and by the temperature of the quantum system, resulting thus in an *ab-initio* approach able to furnish exact estimations of all the relevant properties of helium, including the condensate and superfluid fractions.

Contrarily to the other quantum Monte Carlo methods, which provide results only for the ground state of the quantum system, PIMC is a finite temperature method, in which the system at the thermodynamic equilibrium is simulated considering a propagation in configuration space for a finite imaginary time. However, the same formalism can be extended also to zero temperature calculations, in the so called Path Integral Ground State method, which still presents the possibility of providing exact results for the averages of the quantum observables in a completely general way, where the correlations between atoms arise only by the definition of the many-body Hamiltonian.

In conclusion, PIMC is able to bring several advantages in dealing with quantum many-body problems: it provides an easy picture for superfluidity and BEC in many-bosons system; it presents an intuitive way to take the approximations under control and, thus, to give exact results for the averages of the physical observables, both at zero and finite temperature; it requires only the knowledge of the Hamiltonian of the many-body system, with no need of specifying any importance sampling. These features make undoubtedly PIMC the most powerful method in the study of BEC properties of quantum fluids and solids.

1.1 Objectives and outline of the thesis

The main objective of this thesis is to study some of the most interesting issues concerning the occurrence of Bose-Einstein condensation in quantum fluids and solids by means of a computational approach based on Path Integral Monte Carlo methods.

In order to accomplish these purposes, we have at first developed Path Integral Monte Carlo codes, both at finite and zero temperature, making use of the most recent tools to improve the efficiency and the reliability of these simulations. Among

them, we have implemented in our code the high-order Chin factorization [19, 20], which permits a very accurate approximation for the thermal density matrix in the limit of low temperatures, and the worm algorithm [21, 7], which provides a very efficient sampling scheme for the quantum system in condition of high-degeneracy, where the effect of the permutations between identical particles becomes significant even on a macroscopic level.

The outline of the thesis is the following:

2. In chapter 2, we present all the details of Path Integral Monte Carlo method, in its original formulation at finite temperature. After the introduction of the basic notions of the Monte Carlo methodology and of the path integral formalism, we describe the more advanced technique aimed to improve the sampling scheme and the estimators implemented in the code for the computation of the physical observables. Finally, we also show the results for some model systems used to test the computational method.

3. Chapter 3 is devoted to the study of the feasibility of Path Integral Ground State calculations with a high-order approximation for the imaginary time propagator. After a previous discussion on the formalism of the methodology, we present highly accurate calculations for the ground state energy and for the most relevant properties of liquid ^{4}He at its equilibrium density.
Part of this work has been published in:
R. Rota, J. Casulleras, F. Mazzanti and J. Boronat, "High-order time expansion path integral ground state", *Physical Review E*, **81**, 016707 (2010).

4. In chapter 4, we present calculations of the one-body density matrix $\rho_1(r)$ in liquid ^{4}He over a wide range of densities. The unbiased calculation of ρ_1 provided by PIMC methods allows us to obtain precise result for the condensate fraction n_0 and for the momentum distribution $n(k)$, which present a good agreement with the most recent experimental measurement.
Most of these results are presented also in:
R. Rota and J. Boronat, "Condensate fraction in liquid ^{4}He at zero temperature", *Journal of Low Temperature Physics*, on press.

5. Chapter 5 is the most significant part of this thesis. It deals with the relevant topic of supersolidity and its occurrence in solid ^{4}He. We performed simulations of different configurations of solid ^{4}He, such as the commensurate crystal, the crystal presenting vacancies or the disordered amorphous configuration. We compare the temperature behavior of the one-body density matrix and of the superfluid fraction obtained numerically with the experimental results, in order to test whether these models are able to provide a reliable description of the properties detected experimentally in the analysis of solid ^{4}He samples. The results presented in this chapter are the content of different published or submitted papers:
R. Rota and J. Boronat, "Path Integral Monte Carlo Calculation of Momentum Distribution in Solid ^{4}He", *Journal of Low Temperature Physics*, **162**, 146

(2011).
Y. Lutsyshyn, R. Rota and J. Boronat, "On the Stability of Small Vacancy Clusters in Solid ^{4}He", *Journal of Low Temperature Physics*, **162**, 455 (2011).
R. Rota and J. Boronat, "Microscopic approach to the bcc phase of solid ^{4}He", *Molecular Physics*, on press (DOI: 10.1080/00268976.2011.620025)).
R. Rota and J. Boronat, "Onset temperature of Bose-Einstein condensation in incommensurate solid ^{4}He", submitted to *Physical Review Letters*.

6. In chapter 6, we present a study of a metastable liquid phase of pH$_2$, aimed at investigating if this system may support superfluidity at low temperatures. Although at low temperatures it is difficult to frustrate the formation of the crystal in microscopic simulations, we have been able to make metastable a glass configuration which presents a non-zero superfluid fraction at temperatures below 1 K.

7. Chapter 7 comprises the main conclusions of this thesis and some ideas for a further development of the studies presented in it.

Chapter 2

Path Integral Monte Carlo

This chapter is devoted to Path Integral Monte Carlo, that is the computational method used to accomplish the objectives of the present thesis. We will describe at first the general basis of Monte Carlo methods and how these can be implemented within the path integral formalism. Later, we will present also more advanced techniques, such as the high-order approximations for the thermal density matrix and the worm algorithm. Finally, we will show results for some model systems used to test the computational method.

2.1 The Monte Carlo methods

The term Monte Carlo is widely understood as any computational method which makes use of stochastic sampling. In the last decades, the popularity of Monte Carlo methods has increased enormously, thanks especially to their huge versatility, which allows to use them in several applications, even of different nature. For instance, Monte Carlo methods are employed in the simulations of stochastic events, such as the trend of financial stocks, or in solving non probabilistic problems, such as the calculation of multidimensional integrals [22].

Monte Carlo methods are widely used in condensed matter physics, where the systems studied are characterized by an extremely high number of degrees of freedom and it is necessary to describe them within a statistical approach. In particular, for every state μ of the physical system, we need to define a statistical weight w_μ, which indicate the probability of finding the system in that state (it follows that $\sum_\mu w_\mu = 1$). Therefore, the average of any physical observable O is given by the sum

$$\langle O \rangle = \sum_\mu O_\mu w_\mu \tag{2.1}$$

This sum, however, is performed over an infinite number of states and can be solved analytically only in few cases. A useful approximation in order to give a reliable result for $\langle O \rangle$ is to consider just a finite number of degrees of freedom of the system and compute numerically the sum in Eq. 2.1. Nevertheless, even for systems made up of a small number of particles, the number of possible states can be huge and can make the computation extremely demanding.

Monte Carlo methods, instead, can provide more efficient algorithms for the computation of the properties of many-body systems simulating stochastically the random fluctuation of the physical system. Let us take the example of a classical system at a temperature T: the probability distribution of the states is given by the

Boltzmann distribution $w_\mu = Z^{-1}e^{-\beta E_\mu}$, where β is the inverse of the temperature, E_μ represents the energy for the state μ and $Z = \sum_\mu e^{-\beta E_\mu}$ is the partition function. If we are able to sample M states μ_i of the system according to a probability distribution p_μ, therefore, according to the central limit theorem, the variable

$$\langle O \rangle_{M,p_\mu} = \frac{\sum_{i=1}^{M} O_{\mu_i} p_{\mu_i}^{-1} e^{-\beta E_{\mu_i}}}{\sum_{i=1}^{M} p_{\mu_i}^{-1} e^{-\beta E_{\mu_i}}} \tag{2.2}$$

is a gaussian variable with mean value $\langle O \rangle$ defined in Eq. 2.1 and with standard deviation proportional to $1/\sqrt{M}$. This means that, increasing the number of sampling points M, the variable $\langle O \rangle_{M,p_\mu}$ becomes a better and better approximation for $\langle O \rangle$.

It is easy to understand that the choice of the probability distribution used in the sampling p_μ strongly affects the efficiency of the calculation. Indeed, in the sum in Eq. 2.1, only a small fraction of states μ of the system contributes, while most of the states give a negligible contribution to $\langle O \rangle$. If in our simulation we would be able to sample the states μ_i according to the Boltzmann distribution $p_\mu = Z^{-1}e^{-\beta E_\mu}$, during the simulation the states which contribute most would appear more frequently than others and, therefore, the estimation of $\langle O \rangle$ given by Eq. 2.2 would converge more quickly to the expected value. The device of selecting the sampled states according to a probability distribution which is similar to the one of the simulated system is called *importance sampling* and is fundamental to develop an efficient Monte Carlo calculation.

2.1.1 The Metropolis Algorithm

A good choice of the importance sampling can considerably improve the efficiency of the calculation of $\langle O \rangle$, but we are still far from a complete solution of the problem. In the previous discussion, we have taken as hypothesis the possibility of sampling an arbitrary probability distribution $p(x)$. The pseudo-random number generators commonly used in computer applications are able to sample uniformly the real numbers in the interval $[0, 1)$ (see for instance Chapter 7 of Ref. [23]) and it is not trivial to use them in order to sample any $p(x)$.

The *Metropolis algorithm* [24] provides a simple and effective method to sample an arbitrary probability distribution function, despite of its analytical complexity or the dimensionality of the problem. This algorithm is based on the theory of Markov chains and makes use, in order to sample a distribution probability $p(x)$, of the evolution of a stochastic process $\Pi(x|y)$ which satisfies with $p(x)$ the detailed balance condition:

$$\Pi(x|y)p(y) = \Pi(y|x)p(x) \ . \tag{2.3}$$

This only condition allows us a certain freedom in the choice of $\Pi(x|y)$: in particular, it is convenient to decompose the stochastic process as

$$\Pi(x|y) = T(x|y)A(x|y) \ ,$$

where $T(x|y)$ is a stochastic process that we can sample and $A(x|y)$ indicates the probability of accepting the move from the configuration y to x sampled according to T.

Generally, the choice of T is arbitrary, while A is defined from T in order to satisfy Eq. 2.3. The main feature of the Metropolis algorithm is to fix A according to the formula

$$A(x|y) = \min\left(1; \frac{T(y|x)p(x)}{T(x|y)p(y)}\right) . \tag{2.4}$$

Commonly, T is chosen so that $T(y|x) = T(x|y)$ (symmetric model): in this case, we recover the simpler definition of A

$$A(x|y) = \min\left(1; \frac{p(x)}{p(y)}\right) . \tag{2.5}$$

For practical purposes, the implementation of this algorithm consists of few steps:

- given a variable x_i, i-th element of a sequence of random variables, we generate a new variable x' using the stochastic process $T(x'|x_i)$
- we evaluate $A(x'|x_i) = \alpha \leq 1$, according to the definition given in Eq. 2.4
- we accept the movement $x_i \to x'$ with probability α: this means that, generating a random number $r \in [0, 1)$, if $r < \alpha$, we accept the movement and we put $x_{i+1} = x'$; otherwise, we reject the movement and we put $x_{i+1} = x_i$
- We repeat the procedure to generate the following variables $x_{i+2}, x_{i+3}, \ldots$

The Metropolis algorithm is able to sample any probability distribution in a rather simple way, but nonetheless presents two weak points: at first, the sampling is correct only asymptotically; secondly, two following variables in the sampled sequence are strongly correlated between each other.

The first problem can be avoided with an equilibration of the system, that is discarding the first variables of the sequence, in order to use in the calculation of the averages only the variables which we expect sampled according to the correct probability distribution. However, there is no general method in order to establish the number of steps to discard. Usually, we observe the disappearance of transient regimes in the estimation of the variables computed, even though this method is rather empirical and does not consider the possibility for the system to remain stuck in eventual metastable states.

The second problem, i.e. the correlation between the sampled variables, affects the estimation of the statistical error of the averages. An efficient method for solving this problem is called *data blocking*. It consists in collecting a sequence of M variables in n blocks, each one made up of $K = M/n$ elements. If we average the estimations of the observable O on each of these blocks, we will obtain a set of n values O_j. The average of these O_j is independent of n and it is still an estimation of $\langle O \rangle$. Furthermore, if K is large enough, the values for O_j can be considered statistically

independent and therefore the statistical error can be computed easily with the formula

$$\sigma_O = \sqrt{\frac{1}{n(n-1)} \sum_{j=1}^{n} (O_j - \langle O \rangle)^2} \ . \tag{2.6}$$

A last trick we have to take into account, in order to make the Metropolis algorithm work properly, concerns the choice of the stochastic process $T(x|y)$. If T proposes "big" updates which change notably the configuration of the system, most of these updates will be rejected since the new configuration will land in a region of low probability density: therefore the acceptance rate of these updates will be small and the stochastic process Π will converge slowly to the desired probability distribution $p(x)$. On the other hand, if T allows just for "small" updates, the acceptance rate will be higher but the algorithm will not be able to explore properly the region of low probability density and the sampling may lose ergodicity. A good compromise between these two opposite cases can be found in the choice of a stochastic process T with an acceptance rate close to 50%.

2.2 The Path Integral Monte Carlo method

2.2.1 The Feynman's Path Integral formalism

The properties of a quantum system in thermal equilibrium are obtainable from the thermal density matrix $\hat{\rho}$ [25]. For a system with Hamiltonian $\hat{H}$ at temperature T, the thermal density matrix is written

$$\hat{\rho} = \frac{e^{-\beta \hat{H}}}{Z} \ , \tag{2.7}$$

where $\beta = (k_B T)^{-1}$, with k_B the Boltzmann's constant, and $Z = \mathrm{Tr}\left(e^{-\beta \hat{H}}\right)$ is the partition function. Knowing the thermal density matrix, the expectation value of an observable operator $\hat{O}$ (for sake of simplicity, we choose a diagonal observable $\hat{O}$) is given by

$$\langle \hat{O} \rangle = \mathrm{Tr}\left(\hat{\rho}\, \hat{O}\right) = \int d\mathbf{R}\, \rho(\mathbf{R}, \mathbf{R}; \beta)\, O(\mathbf{R}) \ , \tag{2.8}$$

where in the last equation we have written the thermal density matrix in the coordinate representation $\rho(\mathbf{R}_1, \mathbf{R}_2; \beta) = \langle \mathbf{R}_2 | \hat{\rho} | \mathbf{R}_1 \rangle$, being $\mathbf{R}_i = \{\mathbf{r}_{1,i}, \mathbf{r}_{2,i}, \ldots, \mathbf{r}_{N,i}\}$ a set of the coordinates of the N particles of the system.

The key aspect of the Path Integral formalism is to make use of the convolution property of ρ

$$\rho(\mathbf{R}_1, \mathbf{R}_3; \beta_1 + \beta_2) = \int d\mathbf{R}_2\, \rho(\mathbf{R}_1, \mathbf{R}_2; \beta_1)\, \rho(\mathbf{R}_2, \mathbf{R}_3; \beta_2) \tag{2.9}$$

in order to rewrite the thermal density matrix as

$$\rho(\mathbf{R}_1, \mathbf{R}_{M+1}; \beta) = \int d\mathbf{R}_2 \ldots d\mathbf{R}_M \rho(\mathbf{R}_1, \mathbf{R}_2; \varepsilon) \rho(\mathbf{R}_2, \mathbf{R}_3; \varepsilon) \ldots \rho(\mathbf{R}_M, \mathbf{R}_{M+1}; \varepsilon) \tag{2.10}$$

with $\varepsilon = \beta/M$. We should notice that the thermal density matrix $\hat{\rho}$ is formally equivalent to an evolution operator in imaginary time $t = i\beta$. Then, we may read Eq. 2.10 as an evolution in imaginary time from the initial configuration $\mathbf{R}_1$ to the final $\mathbf{R}_{M+1}$, rewritten through a series of intermediate steps $\mathbf{R}_2, \dots \mathbf{R}_M$ which define a "path" in the space of the configurations. For a finite value of M, we have a discrete-time path. As the time increment ε is allowed to approach to zero, the number of integrations becomes infinite and the path becomes continuous. However, we have to notice that Eq. 2.10 if exact for any value $M \geq 1$.

2.2.2 Implementing Path Integral in Monte Carlo simulations

In the classical limit of high temperatures, it is possible to give an analytic approximation for the thermal density matrix. Suppose we have a quantum system made up of N particles of mass m interacting with a pair potential $v(\mathbf{r})$. The Hamiltonian of such a system can be split into two terms, $\hat{H} = \hat{K} + \hat{V}$, being

$$\hat{K} = -\frac{\hbar^2}{2m} \sum_{i=1}^{N} \nabla_i^2 \tag{2.11}$$

the kinetic part and

$$\hat{V} = \sum_{i<j} v(\mathbf{r}_i - \mathbf{r}_j) \tag{2.12}$$

the potential part of the Hamiltonian ($\hbar$ is the Planck's constant). If we want to give an analytical expression for the thermal density matrix, we should be able to estimate all the commutators between $\hat{K}$ and $\hat{V}$, in virtue of the Baker-Campbell-Hausdorff formula

$$e^{-\varepsilon(\hat{K}+\hat{V})} = e^{-\varepsilon\hat{K}} e^{-\varepsilon\hat{V}} e^{-\frac{\varepsilon^2}{2}[\hat{K},\hat{V}]} e^{-\frac{\varepsilon^3}{6}\left(2[\hat{V},[\hat{K},\hat{V}]]+[\hat{K},[\hat{K},\hat{V}]]\right)} \dots \ . \tag{2.13}$$

Nonetheless, we can notice that these commutators appear in Eq. 2.13 at order ε^2 or higher. Therefore, in the limit of small imaginary time ε (or equivalently, high temperatures), we can neglect them and recover the approximate form for the thermal density matrix usually called *primitive approximation*:

$$\rho_{PA}(\mathbf{R}_1, \mathbf{R}_2; \varepsilon) = \frac{1}{Z} \int d\mathbf{R}' \langle \mathbf{R}_2 | e^{-\varepsilon\hat{K}} | \mathbf{R}' \rangle \langle \mathbf{R}' | e^{-\varepsilon\hat{V}} | \mathbf{R}_1 \rangle \ . \tag{2.14}$$

The matrix elements of $e^{-\varepsilon\hat{K}}$ and $e^{-\varepsilon\hat{V}}$ can be easily determined in coordinate representation. Since the potential energy operator $\hat{V}$ is diagonal in the space of coordinates, we get

$$\langle \mathbf{R}_{j+1} | e^{-\varepsilon\hat{V}} | \mathbf{R}_j \rangle = e^{-\varepsilon V(\mathbf{R}_j)} \delta(\mathbf{R}_{j+1} - \mathbf{R}_j) \ , \tag{2.15}$$

where we have defined $V(\mathbf{R}_j) = \sum_{i_1<i_2} v(\mathbf{r}_{i_1,j} - \mathbf{r}_{i_2,j})$, where i_1 and i_2 are used to refer to the particle indexes. The kinetic energy propagator in the space of coordinates can be exactly evaluated,

$$\langle \mathbf{R}_{j+1} | e^{-\varepsilon\hat{K}} | \mathbf{R}_j \rangle = (4\pi\lambda\varepsilon)^{-dN/2} e^{-\frac{(\mathbf{R}_{j+1}-\mathbf{R}_j)^2}{4\lambda\varepsilon}} \ , \tag{2.16}$$

where d is the dimensionality of the system, $\lambda = \hbar^2/(2m)$, and we use the definition $(\mathbf{R}_{j+1} - \mathbf{R}_j)^2 = \sum_{i=1}^{N} (\mathbf{r}_{i,j+1} - \mathbf{r}_{i,j})^2$.

Once we have defined a high temperature approximation for ρ, we can obtain an approximation for any T increasing the number M of convolution terms in Eq. 2.10. The convergence to the exact value of the thermal density matrix is guaranteed by the Trotter formula [26]:

$$e^{-\beta(\hat{K}+\hat{V})} = \lim_{M\to\infty} \left(e^{-\varepsilon\hat{K}} e^{-\varepsilon\hat{V}} \right)^M \quad . \tag{2.17}$$

Therefore, the expectation value of the observable $\hat{O}$ (Eq. 2.8) can be rewritten

$$\langle \hat{O} \rangle = \int d\mathbf{R}\, \rho(\mathbf{R}, \mathbf{R}; \beta)\, O(\mathbf{R}) \simeq \int \prod_{j=1}^{M} d\mathbf{R}_j\, O(\mathbf{R}_j)\, \rho_{PA}(\mathbf{R}_{j+1}, \mathbf{R}_j; \varepsilon) \ , \tag{2.18}$$

with $\varepsilon = \beta/M$ and with the boundary condition $\mathbf{R}_{M+1} = \mathbf{R}_1$ which comes the trace, as defined in Eq. 2.8.

It is worth to make two considerations on these last results. At first, we have to notice that the product $p(\mathbf{R}_1, \ldots, \mathbf{R}_M) = \prod_{i=1}^{M} \rho_{PA}(\mathbf{R}_{i+1}, \mathbf{R}_i; \varepsilon)$ is positive definite and its integral over the whole space of configurations gives 1: thus, it can be thought as a distribution probability. This makes the last integral of Eq. 2.18 suitable for being computed with a *Monte Carlo* procedure: that is, sampling all the degrees of freedom according to $p(\mathbf{R}_1, \ldots, \mathbf{R}_M)$ with the Metropolis algorithm and averaging the value for the observables computed on the sampled configuration, one is able to estimate the quantum averages of relevant physical quantities in a rather simple way [27]. Furthermore, it is worth pointing out that the last equality in Eq. 2.18 is approximate for finite M, but becomes exact in the limit $M \to \infty$, in virtue of the Trotter formula (Eq. 2.17). This means that, increasing the number M, we are able to decrease the systematic error due to the approximation of the thermal density matrix: at sufficiently large M, it will be lower than the unavoidable statistical error associated to the Monte Carlo estimation and thus we could, in principle, recover the exact value of the expectation value $\langle \hat{O} \rangle$. For this reason, Path Integral Monte Carlo is often referred as an *exact method*.

2.2.3 The classical isomorphism

The key aspect of Path Integral Monte Carlo (PIMC) method is to describe the quantum N-body system by means of M different configurations $\mathbf{R}_j$ of the same system, whose sequence $\{\mathbf{R}_1, \ldots, \mathbf{R}_M\}$ constitutes a path in imaginary time in the space of configurations. This means that the quantum system made up of N atoms can be made equivalent to a classical system of $N \times M$ particles: each of these classical particles is usually called a *bead*.

The path integral expression Eq. 2.18, indeed, can be interpreted as a classical configuration integral, where the term

$$S(\mathbf{R}_{j+1}, \mathbf{R}_j; \varepsilon) = -\ln\left[\rho(\mathbf{R}_{j+1}, \mathbf{R}_j; \varepsilon)\right] \tag{2.19}$$

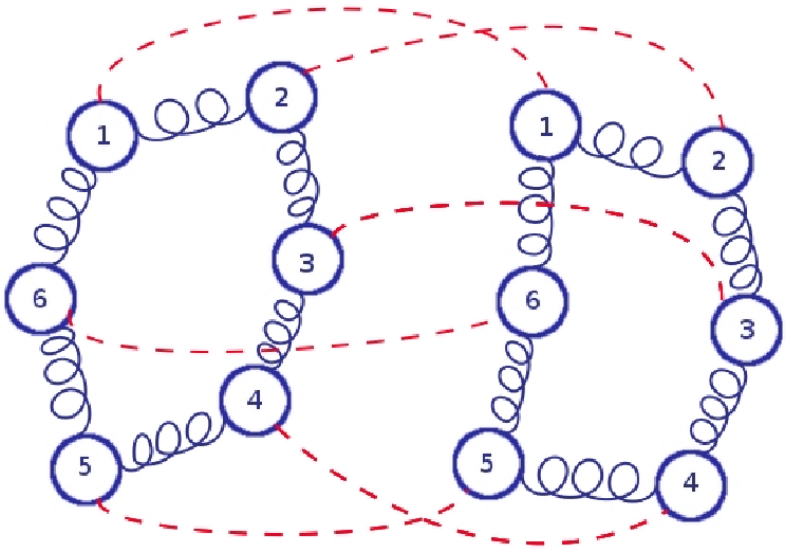

Figure 2.1: Schematic representation of the classical polymers describing the quantum atoms in the PIMC isomorphism: the numbered circles represent the beads; the blue springs represent the kinetic action acting on following beads of the same chain; the red dashed lines represent the potential action acting on beads with the same index.

is analogous to a classical potential energy function divided by a fictitious temperature [25, 28]. The function S defined in Eq. 2.19 is called *action* and specifies the interaction between the beads in the classical analog of the quantum system. The action depends on the choice of the analytical form used to approximate the thermal density matrix, but usually can be split into kinetic and potential contributions.

The kinetic contribution to the action can be derived directly from Eq. 2.16. In order to understand how this kinetic contribution is mapped onto the classical PIMC analog, let us consider the example of a free particle. A bead $\mathbf{r}_j$ of the free particle is correlated through the kinetic propagator Eq. 2.16 (which in this case represents exactly the thermal density matrix) only to the beads $\mathbf{r}_{j-1}$ and $\mathbf{r}_{j+1}$: this means that the quantum atom can be mapped onto a classical chain of beads, or *polymer*, where each constituent interacts only with two neighbors in the chain. The condition $\mathbf{r}_{M+1} = \mathbf{r}_1$ introduced in Eq. 2.18 indicates that the last bead is connected to the first one and thus the chain is closed on itself. Being the kinetic propagator a Gaussian, it follows that the kinetic action is a quadratic term and therefore corresponds, in the classical analog, to a harmonic potential between the two following beads.

When we consider a N-particle interacting quantum system, we should consider also the potential contribution to the thermal density matrix: this introduce, in the classical system of chains, an interaction between beads belonging to different chains. In the primitive approximation, the potential contribution is given by Eq.

2.15 and the interacting potential between the classical beads is equal to the two-body potential between the quantum atoms. Nonetheless, the peculiarity of this interaction is that it acts only on beads with the same imaginary time index j (Fig. 2.1).

Summarizing, the PIMC method consists in mapping the finite-temperature quantum system onto a classical system made up of interacting closed ring polymers, where every polymer is a necklace of beads connected by ideal springs. It is possible to give a physical meaning to this PIMC isomorphism: we can think about the different beads of the classical polymer as a way to represent the delocalization of the quantum particle due to its zero-point motion. In order to explain this observation, we can consider how the temperature T of the quantum system affects the kinetic action

$$S_K = \frac{M k_B T}{4\lambda}(\mathbf{R}_{j+1} - \mathbf{R}_j)^2 \tag{2.20}$$

At high temperature, the strength of the quadratic term is high and thus the harmonic potential between the different beads is strong. This does not allow the beads of a single chain to move far apart and the polymer is not spread over a big portion of the space, indicating that the quantum particle is not allowed to delocalize. As the temperature decreases, the strength of the springs between the beads decreases and the classical polymer is allowed to spread and therefore to recover the delocalization of the quantum particle.

These considerations make clear the fact that the number of beads M needed to give a good description of the quantum system depends on the temperature. At high temperature, since most of the beads will stay close to each other, the polymer occupies a small volume and therefore there is no need to use a high number of beads to describe the system. In the classical limit, where the zero-point motion of the atom can be neglected, the polymer shrinks to a point and the atom can be easily described by just $M = 1$ bead. On the contrary, at low temperature it is necessary to use higher number of beads, in order to let the classical polymer delocalize as the quantum atom does. To give a prediction on how the number of beads should scale with the temperature of the quantum system, we have to realize that the imaginary time step $\varepsilon = \beta/M$ is fixed by requiring that the action is accurate enough. This means that M should be proportional to β, or equivalently that M should scale as the inverse of the temperature. This scaling law represents a weak point of the PIMC method, since it means that, when approaching the interesting quantum regime at very low temperature, the number of beads increases fast making simulations hard, if not impossible, due to the very low efficiency in the sampling of the long chains involved. The only way to overcome this problem is to improve the approximation scheme for the thermal density matrix, in order to work with larger values of ε.

2.3 High-order approximations for the action

So far, the only approximation scheme for the thermal density matrix we have presented is the Primitive Approximation, Eq. 2.14. This is clearly the simplest

way to approximate the thermal density matrix at high temperature. However, $\rho_{PA}(\mathbf{R}_1, \mathbf{R}_2; \varepsilon)$ presents the disadvantage of being accurate to order ε^2, making thus its convergence to the exact density matrix particularly slow as the number of beads increases.

Primitive Approximation is accurate to study semiclassical systems, where the quantum effects are relatively small. If we are interested in the study of highly degenerate quantum system, like the ones presenting Bose-Einstein condensation, it is important to develop more complex forms for the action that will give correct results for much larger ε and will allow the use of fewer beads in the simulations. Of course, a more accurate approximation scheme will increase the complexity of the PIMC algorithm: it is therefore important to choose the approximation for the action in such a way that it could be evaluated quickly on a computer, in a time not too much slower than it takes to compute the pair potential.

In this section, we want to present high-order approximations obtained directly from the exponential of the Hamiltonian, $\exp(-\beta\hat{H})$. A different approach that generates also very accurate actions for low temperature studies relies on the *pair-product approximation*, in which the basic piece of the PIMC chain is the exact action for the two isolated particles [29]. The pair-product action has been extensively used in the study of superfluidity and it is especially accurate for hard-sphere-like systems such as ^{4}He [18]. However, its use for non radial interactions is much more difficult due to the complexity of the two-body density matrix.

2.3.1 The Takahashi-Imada approximation

In the development of high-order approximation for the thermal density matrix, a good starting point could be the Baker-Campbell-Hausdorff formula, Eq. 2.13. However, as showed by Raedt and Raedt [30], the terms of the expansion of order ε^2 or higher are not well suited to calculate the properties of the physical system because they lead to non-Hermitian approximations of the Hermitian operator $\exp(-\beta\hat{H})$. Nonetheless, since we are interested just in the thermodynamic properties of the quantum systems, there is no need to provide an approximation for the operator $\exp(-\beta\hat{H})$, but just an approximation for its trace. This latter would be simpler because, in developing it, we can take into account the property that the trace is similarity-invariant, that is

$$\mathrm{Tr}\left(e^{-\beta\hat{H}}\right) = \mathrm{Tr}\left(\hat{S}^{-1}e^{-\beta\hat{H}}\hat{S}\right) \tag{2.21}$$

being $\hat{S}$ an invertible operator. Thus, with a proper choice of $\hat{S}$, it would be possible, in principle, to improve the primitive approximation for the partition function Z and for any thermal average $\langle\hat{O}\rangle$ up to an order greater than 2.

According to this result, a convenient form to approximate the thermal density was developed by Takahashi-Imada [31, 32] and, later on, by Li and Broughton in an independent work [33]. In this scheme, the imaginary-time evolution operator is approximated as

$$e^{-\varepsilon\hat{H}} \simeq e^{-\varepsilon\hat{K}}e^{-\varepsilon\hat{V}}e^{-\frac{\varepsilon^3}{24}[[\hat{V},\hat{K}],\hat{V}]} \tag{2.22}$$

In comparison to the Primitive Approximation, the factorization in Eq. 2.22 presents an additional term containing the double-commutator $[[\hat{V},\hat{K}],\hat{V}]$ which improves the approximation for the trace up to ε^4. The evaluation of this double commutator is not particularly heavy, since the term

$$\left[[\hat{V},\hat{K}],\hat{V}\right] = \frac{\hbar^2}{m}|\nabla V|^2 \tag{2.23}$$

depends only on the gradient of the potential and, generally, is not difficult to evaluate.

For practical purposes, a PIMC simulation with Takahashi-Imada approximation is equivalent to a simulation with the Primitive Approximation where, in the potential contribution to the action, Eq. 2.15, we substitute $V(\mathbf{R})$, that is the sum over all the pairs of two-body interactive potential $v(r)$, with the term

$$W(\mathbf{R}) = \sum_{i<j} v(r_{ij}) + \frac{\varepsilon^2}{24}\frac{\hbar^2}{m}\sum_{i=1}^{N}\sum_{j\neq i}|\nabla_i v(r_{ij})|^2 \ . \tag{2.24}$$

Using this approximation in a simulation of liquid ^{4}He, the number of beads needed to reach the $\varepsilon \to 0$ limit decreases by a factor 4. Balancing this gain with the extra computational effort in calculating $W(\mathbf{R})$ instead of $V(\mathbf{R})$, we arrive at a relative improvement of performance of a factor 1.4 [20].

2.3.2 Symplectic Expansions

Another approach aimed to better the Primitive Approximation can, in principle, be provided by a symplectic factorization of the form

$$e^{\varepsilon(\hat{K}+\hat{V})} = \prod_{i=1}^{n} e^{-t_i\varepsilon\hat{K}}e^{-v_i\varepsilon\hat{V}} \ . \tag{2.25}$$

It makes sense to ask if a proper choice of the coefficients $\{t_i, v_i\}$ in Eq. 2.25 is able to cancel out the leading error term in the expansion at the right side of equation, resulting thus in an improved approximation with respect to the primitive one. It has to be noticed that all the parameters $\{t_i, v_i\}$ must be positive (forward propagation in imaginary time), in order to have, in the multidimensional integral for the expectation value $\langle\hat{O}\rangle$, Eq. 2.18, a normalizable function which can be thought as a probability distribution and therefore can be sampled by Monte Carlo methods.

Unfortunately, the Sheng-Suzuki theorem [34, 35] proves that it is impossible to go beyond the second order in ε using the factorization in Eq. 2.25 with only positive coefficients. The better way to overcome this limitation is to introduce the double commutator $[[\hat{V},\hat{K}],\hat{V}]$ at least in one term of the factorization in Eq. 2.25, as proposed by Chin and Chen in Ref. [19]. In this work, authors worked out a continuous family of *gradient symplectic algorithms* which proved to be very accurate in the resolution of classical and quantum problems. Later on, Chin performed

a complete analytical characterization of these fourth-order propagators, showing that they are fully fourth-order and, thus, they improve the Takahashi-Imada approximation which is accurate to fourth order only for the trace [36].

2.3.3 The Chin approximation

Having seen that the incorporation of modified potentials in the factorization for the imaginary time evolution operator is able to make the approximation scheme of fourth order in ε, it is worth to take a step back and modify the symplectic decomposition of Eq. 2.25 introducing terms presenting the double commutator $[[\hat{V},\hat{K}],\hat{V}]$ in the exponential. We may therefore ask if, in the new factorization

$$e^{\varepsilon(\hat{K}+\hat{V})} = \prod_{i=1}^{n} e^{-t_i\varepsilon\hat{K}} e^{-v_i\varepsilon\hat{V}} e^{-w_i\varepsilon\left[[\hat{V},\hat{K}],\hat{V}\right]} , \tag{2.26}$$

it is possible to find some optimal values for the positive coefficients $\{t_i, v_i, w_i\}$ which make Eq. 2.26 an effective sixth-order approximation for the action.

This is the main aspect at the basis of the so called *Chin Approximation*, whose factorization is given explicitly by

$$e^{-\varepsilon\hat{H}} \simeq e^{-v_1\varepsilon\hat{W}_{a_1}} e^{-t_1\varepsilon\hat{K}} e^{-v_2\varepsilon\hat{W}_{a_2}} e^{-t_1\varepsilon\hat{K}} e^{-v_1\varepsilon\hat{W}_{a_1}} e^{-2t_0\varepsilon\hat{K}} , \tag{2.27}$$

where

$$\hat{W}_{a_i} = \hat{V} + \frac{u_0}{v_i} a_i\varepsilon^2 \left[[\hat{V},\hat{K}],\hat{V}\right] \tag{2.28}$$

According to this scheme, the evolution operator is split into $n = 3$ smaller and not equal imaginary time propagations, at which extremes one should evaluate the Takahashi-Imada action, Eq. 2.24. The parameters in Eqs. 2.27 and 2.28 are not all independent: imposing that the right side of the factorization in Eq. 2.27 is accurate to ε^4, it follows that the coefficients must satisfy the following rules:

$$\begin{aligned} u_0 &= \frac{1}{12}\left[1 - \frac{1}{1-2t_0} + \frac{1}{6\,(1-2t_0)^3}\right] \\ v_1 &= \frac{1}{6\,(1-2t_0)^2} \\ v_2 &= 1 - 2v_1 \\ a_2 &= 1 - 2a_1 \\ t_1 &= \frac{1}{2} - t_0 \,. \end{aligned} \tag{2.29}$$

It follows that the only free parameters in this factorization are t_0 and a_1, which are restricted to fulfill the conditions

$$0 \leq a_1 \leq 1 \tag{2.30}$$

$$0 \leq t_0 \leq \frac{1}{2}\left(1 - \frac{1}{\sqrt{3}}\right) . \tag{2.31}$$

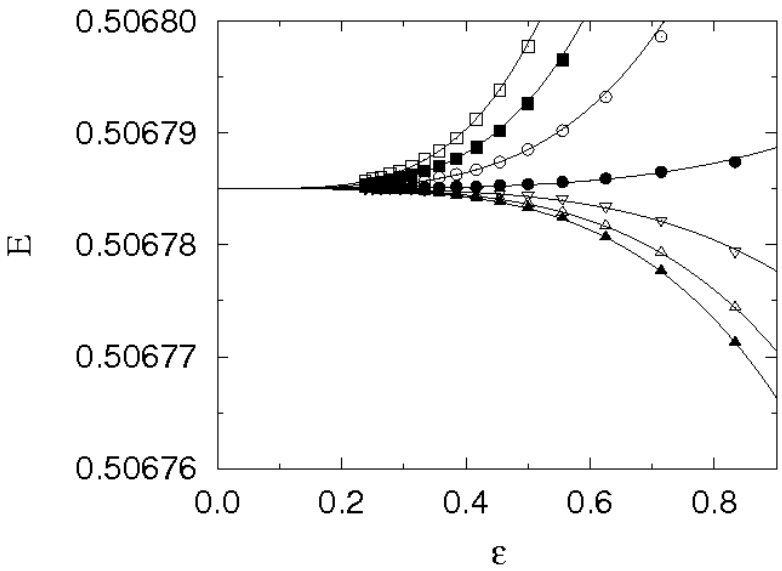

Figure 2.2: Departure from the asymptotic energy E_0 for different values of t_0 in a PIMC calculation of the harmonic oscillator at temperature $T = 0.2$ (from top to bottom, t_0 =0.09, 0.10, 0.11, 0.12, 0.13, 0.14, and 0.15). The figure is taken from Ref. [20]

The accuracy of the Chin Approximation depends on the particular values of a_1 and t_0 that have to be optimized. The optimal values are those achieving an approximate cancelation of the various high-order commutators in the leading fourth-order error. These optimal values are, therefore, independent of the temperature and they can be easily determined numerically carrying out simulations at high temperatures, where the limit $\varepsilon \to 0$ can be reached even with a small number of beads.

A deep analysis of the use of Chin Approximation in PIMC simulations and on its optimization method has been carried out by Sakkos *et al.* in Ref. [20]. An instructive example is the one provided in the study of the one-dimensional harmonic oscillator: in Fig. 2.2, we show their result for the energy E of the system as a function of ε for different values of t_0 at fixed a_1. It is easy to notice that for some values of t_0 the asymptotic exact value E_0 is approached from above, while for other values of t_0, E_0 is approached from below. In particular, since the departure from the asymptotic value E_0 varies monotonically with t_0, there is an optimal value of t_0 for which it is possible to cancel out the leading error term and recover an effective sixth-order approximation. This allows the use of large imaginary time steps, representing huge improvement with respect to the previous approximations for the action, as showed in Fig. 2.3.

Even though a similar sixth order behavior has been found using Chin approximation in the simulation of more complex systems such as a H_2 drop or bulk liquid ^{4}He, Casas in Ref. [37] showed that the fourth-order method obtained from the

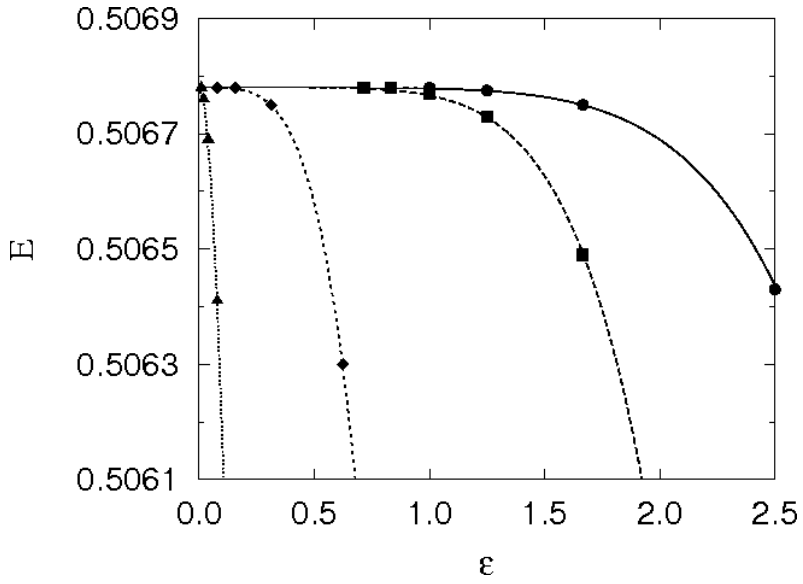

Figure 2.3: PIMC energy of a particle in a one-dimensional harmonic well at temperature $T = 0.2$ as a function of ε: triangles, diamonds, squares, and circles stand for Primitive approximation, Takahashi-Imada approximation, Chin approximation with $a_1 = 0$, and Chin approximation with $a_1 = 1/3$, respectively. The figure is taken from Ref. [20]

factorization in Eq. 2.27 is of effective sixth order only for the harmonic oscillator and not for a more general potential. In this work, Casas deduced the analytical conditions for which the general factorization of Eq. 2.26 can be consider of sixth order, comparing the expansion of the factorization in Eq. 2.26 with the expansion of the evolution operator obtained with the Baker-Campbell-Hausdorff formula (Eq. 2.13). Only in the case of the harmonic oscillator, which has been studied also in a previous work by Scuro and Chin [38], Casas has been able to write down an analytical expression between t_0 and a_1 in the factorization of Eq. 2.27 in order to recover the effective sixth-order approximation. Nevertheless, the linear stability analysis of this method, which is important in order to give an estimation of the maximum time step ε that can be used in the simulation, shows that with a numerical optimization of the parameters, it is possible to achieve a scheme whose linear stability interval is very close to the optimal one, and thus a scheme whose performances are notably high. An estimation of the efficiency of the Chin approximation is given by Sakkos *et al.*: in the simulation of liquid ^{4}He, they have been able to develop an algorithm whose efficiency was eight times larger than the one making use of the primitive approximation [20].

We can concluded that, even if Chin approximation has to be considered as a strictly fourth-order approximation, it presents the performance of a sixth order one, making possible the simulation of highly degenerate quantum systems at low

temperature without exceeding computational efforts.

2.4 The permutation sampling

The discussion performed in the previous sections highlights the most important features of the PIMC method, but it is not complete. What we said up to now, indeed, holds only for systems made up of distinguishable particles. Instead, when we want to deal with quantum many-body systems at low temperature, it is fundamental to take into account the quantum statistic of the particles.

All the states, and thus also the thermal density matrix, are either symmetric or anti-symmetric with respect to a given permutation. A convenient way to recover the right expression for ρ, when dealing with Bose or Fermi statistics, is to sum over all the possible permutations of the particle labels in one of the two arguments

$$\rho_{\substack{B\\F}}(\mathbf{R}_1, \mathbf{R}_2; \beta) = \frac{1}{N!} \sum_{\mathcal{P}} (\pm 1)^P \rho(\mathbf{R}_1, \mathcal{P}\mathbf{R}_2; \beta) \ , \tag{2.32}$$

where $\mathcal{P}$ is one of the $N!$ permutations of the particle labels, P is the number of transpositions of the permutation $\mathcal{P}$ and in the term (± 1) we choose the sing $+$ or $-$ if the system is made up, respectively, of bosons or fermions. With this new definition of the thermal density matrix, the expectation value of any observable $\hat{O}$ (Eq. 2.18) becomes

$$\langle \hat{O} \rangle_{\substack{B\\F}} = \frac{1}{N!} \sum_{\mathcal{P}} \int \prod_{j=1}^{M} d\mathbf{R}_j \, O(\mathbf{R}_j) \, (\pm 1)^P \rho(\mathbf{R}_{j+1}, \mathbf{R}_j; \varepsilon) \tag{2.33}$$

with the condition $\mathbf{R}_{M+1} = \mathcal{P}\mathbf{R}_1$.

An exact evaluation of the $N!$ addends in the sum in Eq. 2.33 becomes soon unfeasible by increasing N. Fortunately, as in the case of distinguishable particles, even in this expression we can recognize a probability distribution and therefore, we can rearrange the Monte Carlo procedure in order to include the sum over the permutations. If we consider Fermi particles, an additional sign would appear in front of each term: the even permutations will contribute positively to $\langle \hat{O} \rangle$, the odd ones will contribute negatively. A Monte Carlo evaluation of Eq. 2.33 for a fermionic system, would lead to a signal-to-noise ratio going to zero for small T and large N. As a consequence of this *sign problem*, the path integral calculation becomes unfeasible unless we introduce some systematic approximations. Similarly to the *Fixed-Node* approximation [39], the *restricted path integral Monte Carlo* [40] allows the estimation of the quantum properties of a fermionic system imposing that the sampled paths are restricted to a region of the configurational space with a positive trial density matrix, thereby avoiding the sign problem.

For systems of bosons, where all the terms in the sum of Eq. 2.33 are positive, the evaluation of $\langle \hat{O} \rangle$ is feasible, but not trivial. In order to understand how to include the sum over permutations in the Monte Carlo procedure, it is important to

notice that the symmetrization of the thermal density matrix changes the boundary condition on the configuration $\mathbf{R}_{M+1}$. The new condition $\mathbf{R}_{M+1} = \mathcal{P}\mathbf{R}_1$ (where $\mathcal{P}\mathbf{R} = \{\mathbf{r}_{p(1)}, \mathbf{r}_{p(2)}, \ldots, \mathbf{r}_{p(N)}\}$, $p(i)$ being the label of the particle in permutation with the i-th atom) indicates that the last bead of the i-th polymer is not necessarily connected to the first bead of the same chain, but it is connected to the first bead of the $p(i)$-th chain. This means that, when simulating bosons with PIMC, the quantum N-body system is not mapped onto a classical system of N closed polymers made up all of the same number of beads M, but it is possible to find out polymers composed by $L \times M$ beads, which represent the permutation cycles between L bosons. Therefore, in order to include the sampling of permutations, we have to include movements which connect beads belonging to different chains and allow the formation of long polymers.

These movements are quite difficult to implement since they involve simultaneous update of the permutation table $p(i)$ and of the configuration $\mathbf{R}_j$. A typical sampling scheme to include permutations in Path Integral Monte Carlo simulations has been developed by Ceperley, see Ref. [18]. According to this classical scheme, we choose at first the L atoms which should take part to the permutation cycle, according to a kinetic criterion. This choice has to pass a first acceptance/rejection test, in order to satisfy the detailed balance principle. In case of acceptance of this new permutation cycle, the movement follows with a reconstruction of the polymers, in order to reconnect beads belonging the chains selected in the first step of the update. This new configuration is subject to a second acceptance/rejection test according to the potential part of the action. If the update passes even this second test, we have created a new configuration presenting a permutation structure $\mathcal{P}$ different from the initial one.

The performance of this scheme is quite low and it is not able to provide a good sampling of bosonic permutations, especially when the number of atoms increases. The main problem found when using this algorithm is highlighted by Boninsegni [41]: he showed that the acceptance rate of the first test, which defines the L bosons which participate in the permutation, decreases notably with the number L. In particular, he showed that permutations involving more than 6 particles are extremely rare events, independently of the physical system considered or of the algorithm parameters. This pathology strongly affects the simulation when we are interested in the study of the Bose-Einstein condensation or the superfluid properties of the system, since these quantum effects are correlated to the appearance of long permutation cycles between the particles (see subsections 2.5.4 and 2.5.5 for better explanations). From the practical point of view, this problem makes unfeasible the estimation of the superfluid density ρ_s for large systems ($N > 100$) due to the large computational cost required to obtain a change in ρ_s.

Furthermore, in the simulation of strongly interacting systems, such as for instance superfluid ^{4}He, this sampling scheme presents some problems even in dealing with pair exchanges. In general, when the interatomic potential is strongly repulsive at short distance, the possibility of sampling configurations presenting superposition of the particles (i.e. beads of the same imaginary-time index at a distance smaller

than the hard-core) strongly reduces the acceptance rate of the update. In the scheme proposed in Ref. [18], the movements require to update the configuration of at least two different polymers at the same time: this increases the possibility of finding configurations presenting superpositions of the atoms, which would be rejected after the Metropolis test on the potential action.

At the end, due to these intrinsic pathologies, the sampling scheme described above is not able to provide a fully ergodic random walk through permutation space. A different approach in the sampling of the bosonic permutations in PIMC simulations is provided by the *worm algorithm*. It was developed for the first time by Prokof'ev *et al.* in the context of interacting bosons on a lattice [42] and, later, it has been extended to continuous-space systems by Boninsegni *et al.* [21, 7, 43]. A deeper discussion on the path sampling method of the worm algorithm, including a precise description of all the updates needed to perform its implementation, is provided in appendix A. The worm algorithm works in an extended configurational space, given by the union of the ensemble Z, formed by the usual ring-polymer configurations, and the ensemble G, where all the polymers are closed except one, which is left open and usually is referred as the *worm*.

This extension of the configurational space creates the additional difficulty of implementing new updates in order to switch from the configurations in Z to ones in G and vice versa. Nonetheless, including G-configurations in the sampling it is much easier to perform permutations in presence of the worm, thanks to the *swap* movement (Fig. 2.4). The basic idea of the swap movement is to rebuild a free particle path between an open extremity of the worm and a bead belonging to a different polymer: in this way, it is possible to modify both the permutation table $p(i)$ and the configuration of the system $\mathbf{R}_j$ by means of following updates which do not suffer of low acceptance probability. The swap movement is indeed able to overcome the difficulties found when using the previous scheme in the sampling of permutations. At first, it does not require the definition of a L-particles exchange cycle, but the definition of just a single partner which should permutate with the worm. The long cyclic permutations needed to give a microscopic description of the superfluid effects can be obtained after following repetitions of the swap updates. Secondly, the swap movement is a single-particle update, in the sense that, when proposing it, we have to redraw a portion of only one polymer: therefore, the eventuality of the superposition of two atoms is highly reduced.

We have to notice that the probability distribution used to sample the configurations in the subset G is different from the one appearing in 2.33 and therefore these configurations cannot be used to compute the diagonal observables, such as the energy or the superfluid density. However, the G-configurations can be used to compute off-diagonal observables, such as the one-body density matrix $\rho_1(\mathbf{r}, \mathbf{r}')$ (see Section 2.5.4).

In conclusion, the worm algorithm, thanks to its capability to sample the exchanges between bosons by means of single particle updates whose acceptance probability is comparable to that of the other updates in the sampling of the polymers, generates an ergodic and detailed balance random walk through the permutation

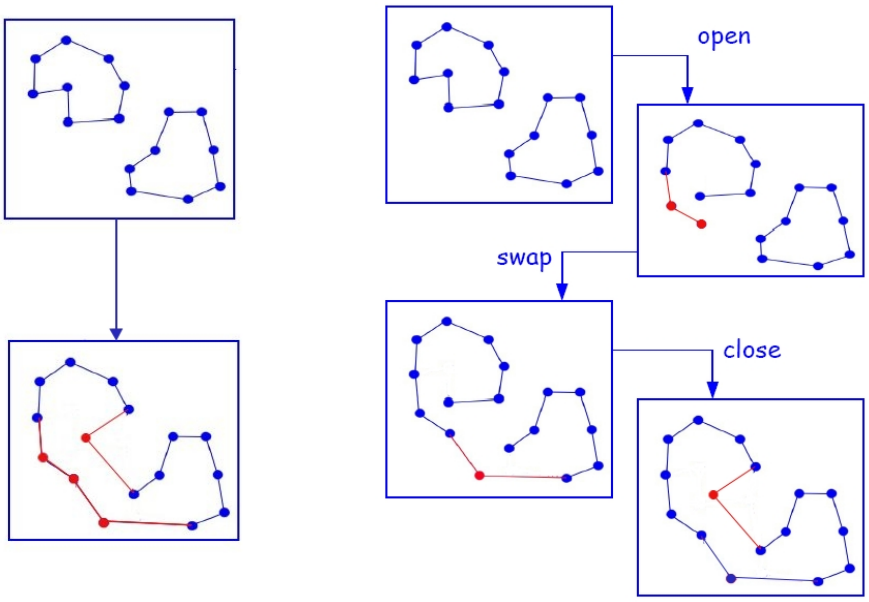

Figure 2.4: Comparison of the permutation movement in the conventional sampling methods (left) and in the worm algorithm (right). If we work in a configurational space where open polymers are not allowed (conventional PIMC), it is necessary to update the configuration of more than one particle to propose a permutation. If we allow the presence of an open polymer in the sampled configurations, as in the worm algorithm, it is possible to propose permutations through subsequent single-particles updates (the link and the beads marked in red are the ones updated after the movement).

space. Thus, it allows for an efficient description of the thermodynamic properties connected to the bosonic statistics of the quantum systems, such as the superfluidity effects or the off-diagonal correlations, and importantly for system much greater than the ones accessible to conventional PIMC simulations.

2.5 Computing the properties

Once the approximation for the action is chosen and the sampling is working, we are ready to calculate expectation values. In this section, we discuss the technical details of constructing estimators for various physical quantities.

2.5.1 Energy per particle

The *energy per particle* E/N is one of the most important quantities we want to get out of a simulation. At finite temperature, E/N can be derived from the partition function Z with the formula

$$\frac{E}{N} = -\frac{1}{NZ}\frac{dZ}{d\beta} \ . \tag{2.34}$$

In the PIMC formalism, the partition function of a three-dimensional bosonic system can be written

$$Z = \frac{1}{N!}\sum_{\mathcal{P}}\int\prod_{j=1}^{M} d\mathbf{R}_j \, (4\pi\lambda\varepsilon)^{-3N/2} \exp\left[-S(\mathbf{R}_{j+1}, \mathbf{R}_j; \varepsilon)\right] \ , \tag{2.35}$$

where we use the condition $\mathbf{R}_{M+1} = \mathcal{P}\mathbf{R}_1$ and, as in Eq. 2.16, the definition $\lambda = \hbar^2/(2m)$. The action

$$S(\mathbf{R}_{j+1}, \mathbf{R}_j; \varepsilon) = \frac{1}{4\lambda\varepsilon}(\mathbf{R}_{j+1} - \mathbf{R}_j)^2 + U(\mathbf{R}_{j+1}, \mathbf{R}_j; \varepsilon) \tag{2.36}$$

is the sum of a kinetic part (first term) and a potential part, which we indicate with U and depends on the approximation used to factorize the thermal density matrix.

If we apply the definition of E/N, Eq. 2.34, directly to Z in Eq. 2.35, we recover the so called *thermodynamic estimator* for the total energy:

$$\frac{E_T}{N} = \left\langle \frac{3}{2\varepsilon} - \frac{1}{MN}\sum_{j=1}^{M}\frac{(\mathbf{R}_{j+1} - \mathbf{R}_j)^2}{4\lambda\varepsilon^2} + \frac{1}{MN}\sum_{j=1}^{M}\frac{\partial U(\mathbf{R}_{j+1}, \mathbf{R}_j; \varepsilon)}{\partial\varepsilon} \right\rangle \ , \tag{2.37}$$

where brackets $\langle \ldots \rangle$ indicate the average over the configurations $\mathbf{R}$ sampled in the Monte Carlo simulation. The first term of the sum is M times the energy of a classical ideal gas $3/(2\beta)$.

In a similar way, we can deduce an estimator for the kinetic energy per particle starting from the definition

$$\frac{K}{N} = -\frac{m}{\beta Z}\frac{dZ}{dm} \ . \tag{2.38}$$

Applying this last definition to Eq. 2.35, we get the thermodynamic estimator for the kinetic energy

$$\frac{K_T}{N} = \left\langle \frac{3}{2\varepsilon} - \frac{1}{MN}\sum_{j=1}^{M}\frac{(\mathbf{R}_{j+1}-\mathbf{R}_j)^2}{4\lambda\varepsilon^2} + \frac{m}{MN\varepsilon}\sum_{j=1}^{M}\frac{\partial U(\mathbf{R}_{j+1},\mathbf{R}_j;\varepsilon)}{\partial m}\right\rangle . \quad (2.39)$$

The estimator for the potential energy can be obtained as the difference $V/N = E/N - K/N$:

$$\frac{V}{N} = \left\langle \frac{1}{MN}\sum_{j=1}^{M}\left(\frac{\partial U(\mathbf{R}_{j+1},\mathbf{R}_j;\varepsilon)}{\partial\varepsilon} - \frac{m}{\varepsilon}\frac{\partial U(\mathbf{R}_{j+1},\mathbf{R}_j;\varepsilon)}{\partial m}\right)\right\rangle . \quad (2.40)$$

We can notice that, for the Primitive Approximation Eq. 2.14, the potential action U does not depend on the mass of the particle. Therefore, in Eq. 2.37, we can easily distinguish the kinetic energy, represented by the first two terms in the sum, and the potential one, which reduces simply to the potential energy of the configuration, averaged over the bead index,

$$\frac{V_{PA}}{N} = \left\langle \frac{1}{MN}\sum_{j=1}^{M} V(\mathbf{R}_j)\right\rangle . \quad (2.41)$$

For high-order approximations, the potential action U depends on the mass of the particle and also the third term $\partial U/\partial\varepsilon$ gives a contribution to the kinetic energy. For instance, in the Takahashi-Imada approximation, the double commutator $\left[[\hat{V},\hat{K}],\hat{V}\right]$ depends on the mass (see Eq. 2.23) and therefore the kinetic energy estimator is written

$$\frac{K_{TIA}}{N} = \left\langle \frac{3}{2\varepsilon} - \frac{1}{MN}\sum_{j=1}^{M}\frac{(\mathbf{R}_{j+1}-\mathbf{R}_j)^2}{4\lambda\varepsilon^2} + \frac{1}{MN}\sum_{j=1}^{M}\frac{\varepsilon^2}{24}\frac{\hbar^2}{m}|\nabla V(\mathbf{R}_j)|^2\right\rangle , \quad (2.42)$$

while the potential energy estimator is

$$\frac{V_{TIA}}{N} = \left\langle \frac{1}{MN}\sum_{j=1}^{M} V(\mathbf{R}_j) + \frac{1}{MN}\sum_{j=1}^{M} 2\,\frac{\varepsilon^2}{24}\frac{\hbar^2}{m}|\nabla V(\mathbf{R}_j)|^2\right\rangle . \quad (2.43)$$

The thermodynamic estimator, Eq. 2.37, is easily implementable in a PIMC simulation, but its statistical error behaves poorly in the limit of small ε. Indeed, as ε becomes small, the first and the second terms in Eq. 2.37 become large and, to find out the energy, we have to estimate a small difference between two large terms. To overcome this pathology, Herman *et al.* have introduced another estimator for the energy per particle whose fluctuation does not increase as ε decreases [44]. This new estimator is obtained integrating by parts over the path variables and is called

virial estimator for the total energy [18]:

$$\begin{aligned}\frac{E_V}{N} &= \left\langle \frac{3}{2\beta} - \frac{1}{N}\sum_{j=1}^{M}\frac{(\mathbf{R}_{M+j}-\mathbf{R}_j)(\mathbf{R}_{M+j-1}-\mathbf{R}_{M+j})}{4\lambda\beta^2} + \right. \\ &+ \frac{1}{2\beta N}\sum_{j=1}^{M}(\mathbf{R}_j-\mathbf{R}_j^C)\frac{\partial}{\partial\mathbf{R}_j}\left[U(\mathbf{R}_{j+1},\mathbf{R}_j;\varepsilon)+U(\mathbf{R}_j,\mathbf{R}_{j-1};\varepsilon)\right] \\ &+ \left.\frac{1}{MN}\sum_{j=1}^{M}\frac{\partial U(\mathbf{R}_{j+1},\mathbf{R}_j;\varepsilon)}{\partial\varepsilon}\right\rangle \end{aligned} \tag{2.44}$$

where we have defined $\mathbf{R}_j^C = \sum_{l=1}^{M-1}(\mathbf{R}_{j+l}+\mathbf{R}_{j-l})/2M$.

The whole derivation of the virial estimator can be found in appendix B. Here, we notice that in the formula 2.44 there are no terms getting large when the number of beads M increases. This feature makes the statistical error quite independent of M and thus the virial estimator is much more efficient than the thermodynamic one in the calculation of the energy.

2.5.2 Pair-correlation function

The *pair correlation function* $g(\mathbf{r}_1,\mathbf{r}_2)$ is proportional to the probability of finding a particle in $\mathbf{r}_2$, when another particle is placed in $\mathbf{r}_1$. Using the Feynman's density matrix formalism, one can define the pair-distribution function at finite temperature as

$$g(\mathbf{r}_1,\mathbf{r}_2) = \frac{V^2}{Z}\int \rho(\mathbf{R},\mathbf{R};\beta)\,d\mathbf{r}_3\ldots d\mathbf{r}_N\ , \tag{2.45}$$

with $\mathbf{R}=\{\mathbf{r}_1,\mathbf{r}_2,\ldots,\mathbf{r}_N\}$. For uniform systems, g does not depend on the choice of $\mathbf{r}_1$, but only on the distance $\mathbf{r}=\mathbf{r}_2-\mathbf{r}_1$. Therefore, it is worth taking into account the symmetry under particle exchange and define the PIMC estimator for the pair distribution function as

$$g(\mathbf{r}) = \frac{V}{N^2}\left\langle \frac{1}{M}\sum_{j=1}^{M}\sum_{i_1\neq i_2}\delta\left(\mathbf{r}-(\mathbf{r}_{i_1,j}-\mathbf{r}_{i_2,j})\right)\right\rangle\ . \tag{2.46}$$

In this equation, we have also considered an average over the bead indexes since, due to the symmetry over imaginary time indexes, all the configuration $\mathbf{R}_j$, with $1\leq j\leq M$, can be considered in the evaluation of $g(\mathbf{r})$ to take advantage of larger statistics.

Practically, the expectation value of the delta function appearing in Eq. 2.46, can be calculated constructing a histogram of the frequencies of the relative distances between all pairs of beads with the same imaginary time index. The column of this histogram corresponding to the segment $[r-\Delta r/2, r+\Delta r/2]$ has to be normalized dividing the number of occurrences by the volume of the associated spherical shell $\frac{4}{3}\pi[(r+\Delta r/2)^3-(r-\Delta r/2)^3]$. In order to avoid systematical error, it is important to take the width Δr of the segments of the histogram small.

However, we have to notice that the estimator of $g(r)$ given in Eq. 2.46 works only in the assumption of knowing exactly the thermal density matrix. A more rigorous estimator for $g(r)$ should be obtained as a functional derivative of the free energy, so that thermodynamic identities will hold between estimators at any imaginary time step ε, not only in the limit of $\varepsilon \to 0$.

In the general case, the average value of an arbitrary observable $\hat{O}$ should be given through the variation of potential

$$\langle \hat{O} \rangle = -\frac{1}{\beta} \frac{1}{Z(V)} \left. \frac{dZ(V + \lambda O)}{d\lambda} \right|_{\lambda=0} , \tag{2.47}$$

$Z(V)$ being the partition function for the system with potential energy operator $\hat{V}$ [31]. When using the primitive approximation, the estimator for $g(r)$ discussed above works properly since the estimation of the distance between the atom i_1 and the atom i_2 is simply the distance, in periodic boundary conditions, of the beads $\mathbf{r}_{i_1,j}$ and $\mathbf{r}_{i_2,j}$ with the same bead index j. On the contrary, this is not true when using more complex approximation schemes, such as the Takahashi-Imada or the Chin approximations. In this case, due to the presence of a corrective term depending on temperature in the expression of the potential action, one should evaluate the distance between the atom i_1 and the atom i_2 according to the formula

$$r_{i_1,i_2} = \sqrt{(\mathbf{r}_{i_1,j} - \mathbf{r}_{i_2,j})^2 + \underbrace{\frac{\varepsilon^2 \hbar^2}{6m} (\nabla_{i_1} V - \nabla_{i_2} V) \cdot (\mathbf{r}_{i_1,j} - \mathbf{r}_{i_2,j})}_{\Delta_{i_1,i_2}}} \tag{2.48}$$

The presence of the term Δ_{i_1,i_2} in Eq. 2.48 may affect the construction of the histogram for the $g(r)$ and, in principle, one should take care of this when performing the PIMC estimation [45]. Nevertheless, it can be shown that the effect of Δ_{i_1,i_2} on the estimation of $g(r)$ is really small: in a simulation of liquid helium in the superfluid regime, we have noticed that the result for $g(r)$ obtained neglecting the term Δ_{i_1,i_2} differs from the correct one on the fifth significative digit, that is an irrelevant quantity if compared to the statistical error.

2.5.3 Static structure factor

Even though the pair distribution function gives a good description of the microscopic structure of the many-body system, in many cases the information given by $g(r)$ is not enough to provide a complete characterization of the system. In these cases, it is necessary to investigate the spatial order of the atoms in the reciprocal space, using the *static structure factor*

$$S(\mathbf{q}) = \frac{1}{NZ} \int d\mathbf{R}\, \rho(\mathbf{R}, \mathbf{R}; \beta) \left(\sum_{i=1}^{N} e^{-i\mathbf{q}\cdot\mathbf{r}_i} \right) \left(\sum_{j=1}^{N} e^{i\mathbf{q}\cdot\mathbf{r}_j} \right) . \tag{2.49}$$

Since the numerical simulation is performed choosing a simulation box with finite size and periodic boundary conditions, the wave vector $\mathbf{q}$ can assume only a

discrete number of values, according to the dimensions of the box. If we consider a rectangular box whose dimension are L_x, L_y and L_z, then

$$\mathbf{q} = \left(2\pi \frac{n_x}{L_x}, 2\pi \frac{n_y}{L_y}, 2\pi \frac{n_z}{L_z} \right) \ , \tag{2.50}$$

where n_x, n_y and n_z are integer numbers.

For practical purposes, the reciprocal space is explored with three cycles on the indexes n_x, n_y and n_z and, once $\mathbf{q}$ is fixed, $S(\mathbf{q})$ is calculated with the formula

$$S(\mathbf{q}) = \frac{1}{NM} \left\langle \sum_{i_1 \neq i_2} \sum_{j=1}^{M} \cos(\mathbf{q} \cdot \mathbf{r}_{i_1,j}) \cos(\mathbf{q} \cdot \mathbf{r}_{i_2,j}) + \sin(\mathbf{q} \cdot \mathbf{r}_{i_1,j}) \sin(\mathbf{q} \cdot \mathbf{r}_{i_2,j}) \right\rangle \ . \tag{2.51}$$

As in the case of $g(r)$, it is possible to take advantage on the symmetry over imaginary time index and use all the configurations $\mathbf{R}_j$, with $1 \leq j \leq M$, in the evaluation of the static structure factor.

2.5.4 One-body density matrix

The *one-body density matrix* (OBDM) $\rho_1(\mathbf{r}, \mathbf{r}')$ is a fundamental quantity when we are interested in the Bose-Einstein condensation (BEC) properties of a quantum system, since it is the inverse Fourier transform of the momentum distribution $n(\mathbf{k})$. Indeed, in a strongly interacting system, a macroscopic occupation of the ground state appears in $n(\mathbf{k})$ as a delta-peak for $\mathbf{k} = 0$ and a divergent behavior $n(k) \sim 1/k$ when $k \to 0$. Nevertheless, such a singular behavior is not easily detectable in numerical simulations because of the finite size effects (the lowest k value is $k = 2\pi/L$, L being the smallest dimension of the simulation box).

When using Quantum Monte Carlo methods, it is preferable to study the BEC properties of a many-body system working in the coordinate space. The OBDM can be written

$$\rho_1(\mathbf{r}_1, \mathbf{r}_1') = \frac{V}{Z} \int d\mathbf{r}_2 \ldots d\mathbf{r}_N \, \rho_B(\mathbf{R}, \mathbf{R}'; \beta) \ , \tag{2.52}$$

where ρ_B is the thermal density matrix for the Bose system (Eq. 2.32) and the configuration $\mathbf{R} = \{\mathbf{r}_1, \mathbf{r}_2, \ldots, \mathbf{r}_N\}$ differs from $\mathbf{R} = \{\mathbf{r}_1', \mathbf{r}_2, \ldots, \mathbf{r}_N\}$ only for the position of one of the N atoms.

When Bose-Einstein condensation is present in a quantum many-body system, $\rho_1(\mathbf{r}_1, \mathbf{r}_1')$ presents a non zero asymptotic value in the limit of large distances $\mathbf{r} = \mathbf{r}_1 - \mathbf{r}_1'$, which indicates, in the space of momenta, the presence of a delta singularity for $\mathbf{k} = 0$ [11]. In particular, the condensate fraction n_0, that is the fraction of atoms inside the zero momentum state, is related to the OBDM by the formula

$$\lim_{|\mathbf{r}_1 - \mathbf{r}_1'| \to \infty} \rho_1(\mathbf{r}_1, \mathbf{r}_1') = n_0 \ . \tag{2.53}$$

We can notice easily that ρ_1 is an off-diagonal observable, since the configurations appearing as arguments of the thermal density matrix in Eq. 2.52 are different,

contrary to the definition of the thermal average of the diagonal observable in Eq. 2.8. This means that the OBDM cannot be calculated in the usual PIMC configurational space made up of ring polymers.

If we expand Eq. 2.52 over a discrete path, we get an expression similar to Eq. 2.33, but with a different condition on the configuration $\mathbf{R}_{M+1}$. In particular, since the configuration $\mathbf{R}$ and $\mathbf{R}'$ in Eq. 2.52 differs only from the position of one atom, the new condition on $\mathbf{R}_{M+1}$ is obtained removing the restriction, on just one polymer, that it returns to the starting position of one of the N polymer. This means that the PIMC calculation of off-diagonal observables, like ρ_1, is performed mapping the quantum system on a classical system in which all polymers but one are closed. We can therefore compute $\rho_1(\mathbf{r})$, being $\mathbf{r} = \mathbf{r}_1 - \mathbf{r}'_1$, with the formula

$$\rho_1(\mathbf{r}) = \frac{V}{NZ} \left\langle \delta \left(\mathbf{r} - (\mathbf{r}_{i_T,1} - \mathbf{r}_{i_H,M+1}) \right) \right\rangle \ , \tag{2.54}$$

where the brackets $\langle \ldots \rangle$ refer to the average over the configurations presenting the open polymer (often referred as off-diagonal configurations) and $\mathbf{r}_{i_T,1}$ and $\mathbf{r}_{i_H,M+1}$ are the positions of the two extremities of the open polymer. In order to compute the average of the delta function we have to build the histogram of the frequencies of the distances between the points $\mathbf{r}_{i_T,1}$ and $\mathbf{r}_{i_H,M+1}$, dividing, at the end, the height of every column by the volume of the corresponding spherical cell, in analogy of the calculation of $g(r)$ described in section 2.5.2.

Nevertheless, the calculation of the OBDM presents the difference, with respect to the computation of $g(r)$, that we cannot take advantage of the symmetry over imaginary time and thus the estimator for $\rho_1(r)$ given in Eq. 2.54 suffers of low efficiency, especially when the number of atoms increases. Indeed, in the off-diagonal configurations, one polymer has to be treated differently from the others and only one distance out of the $3NM$ degrees of freedom contributes to the estimation. The main consequence of this fact is that, for a given configuration, the statistical sample over which the estimator Eq. 2.54 is averaged is much smaller than the one available for the pair correlation function, making thus difficult to reduce the variance of the OBDM computed during the simulation. A way to improve the efficiency of the estimator for ρ_1 is to move, in the Metropolis sampling, the open polymer more frequently than the other atoms. The atoms that are not in the immediate neighborhood of the open chain, indeed, act as a sluggish background and they do not affect strongly estimation of the OBDM.

Another difficulty of the OBDM estimator in Eq. 2.54 is the evaluation of the normalization factor. In this factor, it appears the partition function Z, which is a diagonal observable and therefore cannot be computed sampling off-diagonal configurations. Nonetheless, the right normalization of the OBDM can be achieved adjusting by hand the histogram computed with PIMC, in order to satisfy the condition $\rho_1(0) = 1$. However, this *a posteriori* normalization is not an easy procedure, because of the small occurrences of the distances close to zero, and may introduce systematic errors in the estimation of the condensate fraction n_0. A modification of the algorithm which make this procedure easier is proposed by Ceperley in [18]:

the idea is to add to the action an artificial potential acting between the extremities of the open chain, which operates as an importance sampling, so that these two points will spend roughly the same amount of time at short and large distances. Nevertheless, the choice of the external potential is not trivial and its use does not solve completely the difficulties which are intrinsic to this normalization procedure.

This problem of the normalization can be overcome using the worm algorithm. Its capability to sample both diagonal and off-diagonal configurations allows for the calculation of the properly normalized OBDM (see appendix A) and therefore to avoid the systematic errors that can be induced normalizing the histogram by hand. The possibility of evaluating the normalization factor in Eq. 2.54 is a peculiar feature of the worm algorithm and represents a notable improvement with respect to previous PIMC sampling schemes.

We have also to notice that the main interest of the OBDM is the possibility of estimating the condensate fraction n_0 from its long range behavior, according to Eq. 2.53. When a condensate is present in a quantum system there is a non-zero probability of finding the two extremities at large distances. If we do not consider the permutations between particles, the size of the polymers is of the order of the thermal wavelength and, therefore, the extremities of the open chain cannot move much far away from each other: typically the distribution of the distances between the extremities is a Gaussian and decays fast to zero at large r. On the contrary, when we consider the possibility for the atoms to exchange, long polymers will begin to appear in the sampled configurations and the two extremities can become separated by distances larger than the thermal wavelength. It is therefore important to highlight that to perform a good calculation of ρ_1 and n_0 a good sampling of the permutations is required.

In practice, to compute n_0 by means of PIMC methods, we construct the histogram of $\rho_1(r)$ and focus on its behavior at large r: if $\rho_1(r)$ presents a plateau for a non-zero value at the maximum distances reachable with the microscopic simulation, therefore the system presents BEC, n_0 being the asymptotic limit of $\rho_1(r)$. Thus, a good estimation of n_0 requires also the use of a sufficiently large number of particles, in order to appreciate the asymptotic behavior of the OBDM.

2.5.5 Superfluid density

The superfluid density in a quantum liquid is the fraction of the system which does not respond to movements of the walls of its vessel [46]. To define it, it is worth considering a liquid inside a bucket with cylindrical symmetry and in thermal equilibrium with the walls of its container. The effective moment of inertia of the liquid is defined as the work done for an infinitesimally small rotation rate,

$$I = \left.\frac{d^2F}{d\omega^2}\right|_{\omega=0} = \left.\frac{d\langle \hat{L}_z\rangle}{d\omega}\right|_{\omega=0} \tag{2.55}$$

where F is the free energy, $\hat{L}_z$ is the total angular momentum operator in the direction of the axis of rotation (which we indicate as the z-axis)

$$\hat{L}_z = i\hbar \sum_{i=1}^{N} \frac{\partial}{\partial \theta_i} \tag{2.56}$$

and θ_i is the azimuthal angle of the i-th particle in cylindrical coordinates. The classical momentum of inertia can be written

$$I_c = \left\langle \sum_{i=1}^{N} m_i (r_{\perp_i})^2 \right\rangle \ , \tag{2.57}$$

$r_{\perp_i}$ being the distance of the i-th atom from the rotation axis. The superfluid density ρ_s is the density of the fraction of the system which does not respond classically to the rotation and can be obtained knowing I and I_c as

$$\frac{\rho_s}{\rho} = 1 - \frac{I}{I_c} \ . \tag{2.58}$$

The derivation of an estimator for the superfluid density which can be used in PIMC calculation is not trivial. The main difficulty is that the definition of ρ_s, Eq. 2.58, is obtained considering a rotation, and thus a motion of the system in real time, and it is not straightforward to translate it in the path integral formalism, based on imaginary time. To do that, it is necessary to switch to the reference frame rotating with the bucket and, therefore, to consider the Hamiltonian of the liquid as $\hat{H}_\omega = \hat{H} - \omega \hat{L}_z$, $\hat{H}$ being the Hamiltonian of the liquid at rest. Starting from this consideration, Pollock and Ceperley have deduced a path integral expression for the effective momentum of inertia I [47]. With this result, they get to a PIMC estimator for the superfluid density:

$$\frac{\rho_s}{\rho} = \frac{2m\langle A_z^2 \rangle}{\beta \lambda I_c} \tag{2.59}$$

where we have defined the projected area as

$$\mathbf{A} = \frac{1}{2} \sum_{i=1}^{N} \sum_{j=1}^{M} \mathbf{r}_{i,j} \times \mathbf{r}_{i,j+1} \ . \tag{2.60}$$

and A_z, its component along the z-axis, is the sum of the areas enclosed by all the polymers projected on a plane perpendicular to the rotation axis. Notice that the superfluid density is a diagonal observable and, thus, the average in Eq. 2.59 has to be considered as an average over the closed chain configurations sampled in the PIMC simulation.

For numerical simulations, it is important to generalize the estimator for the superfluid fraction in systems with periodic boundary conditions (PBC), that are more suitable than cylindric geometry. To do that, we consider a quantum liquid enclosed between two cylindric surfaces of mean radius R and spacing d, with $d \ll R$.

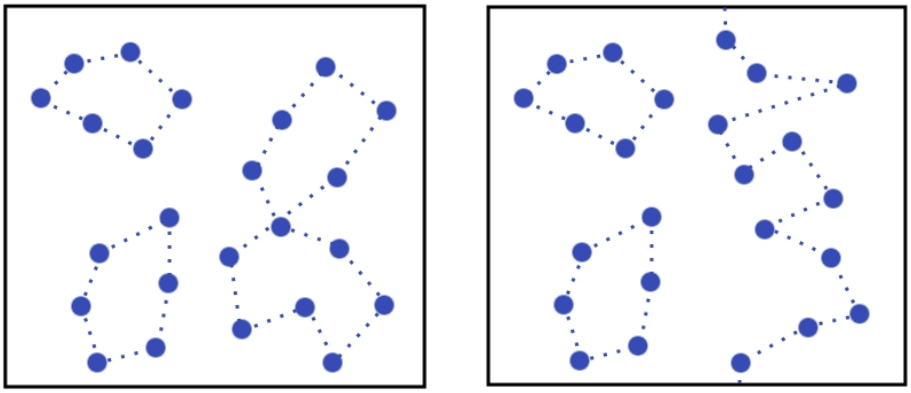

Figure 2.5: Schematic representation of systems presenting zero (left) and non-zero (right) winding number. In the configuration of the left picture, all the polymers close on themselves without crossing the periodic boundaries of the simulation box and none of them winds around any boundary of the box. Thus, summing the relative distances between following beads over all the links, as in the definition of $\mathbf{W}$ (Eq. 2.62), we obtain $\mathbf{W} = 0$. In the configuration of the right picture, there is a polymer which winds around the boundary of the box in one direction. This means that, summing the relative distances between following beads over all the links, we obtain a winding number $\mathbf{W}$ which presents a coordinate different from zero, resulting in a configuration presenting a non-zero superfluid fraction.

Since the superfluid density is proportional to the mean-squared area of the paths sampled for the container at rest and projected on a plane perpendicular to the rotation axis, in this case the only paths contributing to the superfluid density are the ones winding the torus: the other paths, which do not make a complete circuit around the cylinder, give a contribution to A_z which is negligible at large R. If we define the winding number W as the flux of paths winding around the torus times the circumference of the torus, the projected area A_z will be $WR/2$ and the classical momentum of inertia is $I_c = mNR^2$. Using this results in Eq. 2.59, we get

$$\frac{\rho_s}{\rho} = \frac{\langle W^2 \rangle}{2\lambda\beta N} \ . \tag{2.61}$$

We have to remark that a torus, like the one we consider in the previous discussion, is topologically equivalent to the usual periodic boundary conditions. Therefore, the expression in Eq. 2.61 can be used in any system presenting PBC, providing the generalization of the winding number

$$\mathbf{W} = \sum_{i=1}^{N} \sum_{j=1}^{M} \mathbf{r}_{i,j+1} - \mathbf{r}_{i,j} \ . \tag{2.62}$$

Indeed, the whole derivation of Eq. 2.61 could be performed directly in periodic

space by calculating the response of a periodic system to a linear velocity of its walls, replacing the angular momentum operator $\hat{L}$ with the total momentum operator [47].

We have to notice that generally the winding number is a vector, since periodic boundary conditions are usually applied in all three spatial directions, and that it is "quantized" in units of the box length.

The appearance of nonzero winding paths in the sampled configurations is a clear signal of the superfluidity of the simulated systems (Fig. 2.5). It is easy to understand that macroscopic exchange between the atoms are necessary to have paths with nonzero winding number. However, conventional PIMC methods for the sampling of permutations cannot provide good results for the superfluid density in large systems ($N \gtrsim 100$). Indeed, to change the winding number, we need to modify a path spanning the entire system along one direction. Such an update is expected to involve at least a number of particles of the order of $N^{1/3}$ and it is difficult to accept if we sample only diagonal configurations. The worm algorithm, instead, circumvents this pathology working in an extended configurational space presenting also off-diagonal configurations. In this way, the extremities of the open chain can easily propagate crossing the boundary of the simulation box by means of single particle updates. This feature makes the worm algorithm much more efficient in the computation of $\mathbf{W}$ and therefore of the superfluid density.

2.6 Results for model systems

In this section we test the algorithms described so far. We focus on the sampling of the permutations and on the improvement given by the worm algorithm in the study of quantum many-body system. We have performed this test simulating different systems: the quantum harmonic oscillator, the ideal Bose gas and, finally, bulk liquid ^{4}He.

2.6.1 Harmonic oscillator

In the first application, we compute the energy per particle of N particles in a one-dimensional harmonic well, with Hamiltonian

$$\hat{H} = \sum_{i=1}^{N} -\frac{\hbar^2}{2m}\frac{\partial^2}{\partial x_i^2} + \frac{1}{2}m\omega^2 x_i^2 \ . \tag{2.63}$$

This problem is a good test for a computational method, since it can be solved analytically at any temperature and thus we have exact values for the energy with which we can compare our numerical results. The exact solution for the system of N distinguishable particles is [48]

$$\frac{E}{N} = \frac{\hbar\omega}{2}\coth\left(\frac{\hbar\omega}{2k_B T}\right) \ , \tag{2.64}$$

T/T_0	E/N exact	E/N PIMC
	Distinguishable particles	
0.2	0.50678	0.50678(3)
0.4	0.58943	0.58944(4)
0.8	0.90155	0.90162(8)
	Bosons	
0.1	0.50001	0.50005(12)
0.2	0.50115	0.50114(12)
0.4	0.51748	0.51741(8)
0.8	0.61546	0.61545(6)

Table 2.1: Energy per particle in the system on $N = 6$ particles in a harmonic potential as a function of the temperature. Numbers in parentheses are statistical errors.

while for a system of N bosons is [31]

$$\frac{E}{N} = \frac{\hbar\omega}{N}\left[\sum_{l=1}^{N}\frac{l}{2}\coth\left(\frac{l\hbar\omega}{2k_BT}\right) - \frac{N(N-1)}{4}\right] . \tag{2.65}$$

This system can be easily implemented in a PIMC code. Nevertheless, despite its simplicity, this problem is not a trivial test for our computational method. Indeed, the possibility of sampling the variables and evaluating the estimators quickly allows to give very precise results for the energy: it is possible to reduce the statistical error down to fourth or the fifth significative digit in reasonable computing time. If we are able to get results with such a precision and in agreement with the exact values, we have the guarantee that our sampling scheme is working properly. It is important to notice that the choice of the approximation for the thermal density matrix plays an important role in these calculations. The accuracy of the Chin approximation makes possible to simulate the quantum system using few beads and thus to recover precise results for the energy in an easier way with respect to other approximation schemes.

In our PIMC simulation, we have considered a system made up of $N = 6$ particles at different temperature, assuming $\hbar = \omega = m = k_B = 1$. At first, we have performed our calculation considering distinguishable particles. Secondly, we have implemented the worm algorithm in our code, in order to perform the more demanding simulation of a bosonic system. The results for both cases are shown in Table 2.1 and in Fig. 2.6. We note that the results obtained from PIMC are in excellent agreement with the exact ones and we can conclude that worm algorithm is able to perform a good sampling of the permutations, at least in this kind of weakly interacting systems.

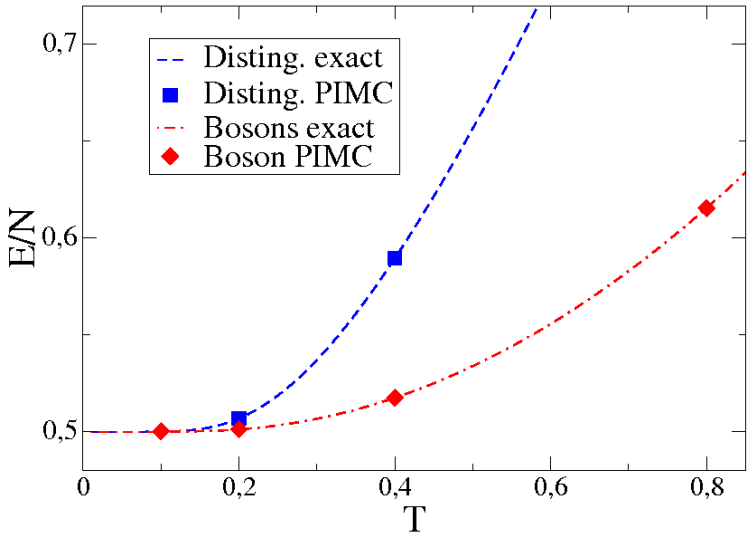

Figure 2.6: Energy per particle in the system on $N = 6$ particles in a harmonic potential as a function of the temperature: the lines are the theoretical expectation (blue dashed for distinguishable particles, red dot-dashed for bosons), the symbols are the PIMC results (blue squares for distinguishable particles, red diamonds for bosons) Statistical error are below symbol size.

2.6.2 Ideal gas

Another important feature of the worm algorithm is its capability to compute the properly normalized one-body density matrix $\rho_1(\mathbf{r})$. To test this feature, we have calculated $\rho_1(r)$ for a three-dimensional ideal Bose gas.

As in the previous case of the harmonic oscillator, also the problem of the ideal Bose gas can be treated analytically and we can derive exact results which we can compare with the ones obtained from the simulation. Quantum statistical mechanics tell us that a three-dimensional ideal system of bosons undergoes Bose-Einstein condensation below the critical temperature

$$T_c = \frac{2\pi\hbar^2}{m k_B}\left(\frac{\rho}{\zeta(3/2)}\right)^{2/3} \tag{2.66}$$

where $\zeta(y)$ is the zeta Riemann function ($\zeta(3/2) = 2.612$) [48]. Below T_c, the condensate fraction is

$$n_0 = 1 - \left(\frac{T}{T_c}\right)^{3/2} \tag{2.67}$$

and the one-body density matrix is given by the sum of the condensate fraction and the inverse Fourier transform of the Bose distribution function:

$$\rho_1(\mathbf{r}) = n_0 + \frac{1}{(2\pi)^3\rho}\int d\mathbf{k}\,\frac{e^{i\mathbf{k}\cdot\mathbf{r}}}{e^{\beta(\hbar^2k^2/(2m))} - 1}\,. \tag{2.68}$$

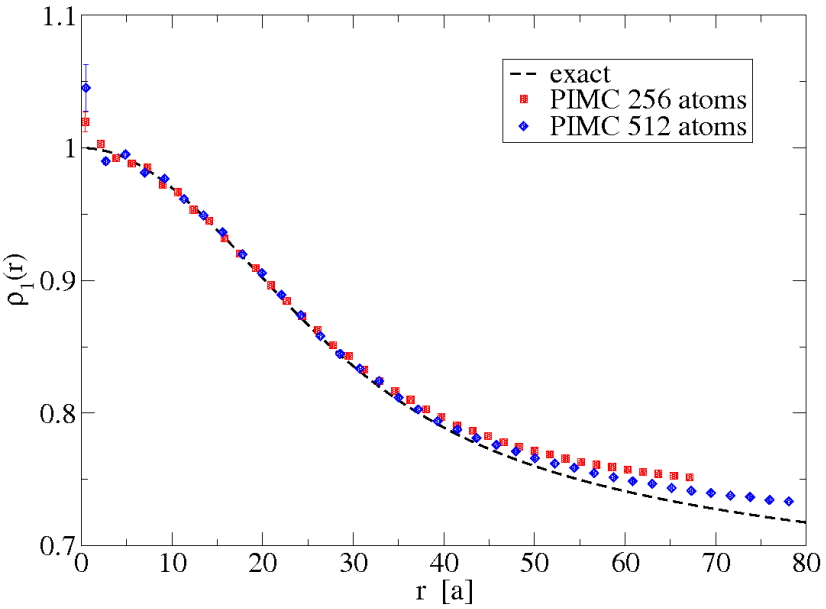

Figure 2.7: One-body density matrix for the ideal Bose gas at temperature $T = 0.5\,T_c$, being T_c the Bose-Einstein condensation transition temperature (Eq. 2.66). The red squares and the blue diamonds represent the PIMC result respectively for the system of $N = 256$ and $N = 512$ particles and the black dashed line represent the exact result (Eq. 2.68). Statistical errors of the PIMC result, if not shown are below symbol size.

To compute the OBDM for the ideal Bose gas, we have simulated N atoms completely free to move inside a cubic box, whose dimensions are fixed according to the density ρ of the gas, with periodic boundary conditions. We have performed simulations for different values of the number of particles N and of the temperature T: in Fig. 2.7 we show the result for $\rho_1(r)$ in the two largest system studied ($N = 256$ and $N = 512$) at temperature $T = 0.5\,T_c$ (T_c is the critical temperature of the gas, Eq. 2.66). Even if the simulated systems are not big enough to see the plateau of the OBDM and therefore to give an estimation of the condensate fraction, we can see that our result is in good agreement with the one expected theoretically. In particular, we notice that, at short distances, $\rho_1(r)$ is close to 1, satisfying the normalization condition on the OBDM. The deviation of the numerical results from the analytical curve of $\rho_1(r)$ at large r, which is large for the smaller system of $N = 256$ atoms, can be attributed to finite size effects.

It is important to remark that in this case of non-interacting system, the action is merely kinetic and, thus, exactly known (Eq. 2.16). Therefore, the only difficulty in the simulation of the ideal gas is given by the sampling of the bosonic permutations. The good agreement between the PIMC result and the exact one given in Eq. 2.68 indicates that the worm algorithm is able to describe properly the exchange between the identical particles.

2.6.3 Liquid ^{4}He

As a last test, we have studied the performance of the method in a fully many-body calculation, as it is liquid ^{4}He. This is a stringent test for a computational technique, since in bulk ^{4}He at low temperature, the correlations between the atoms arise from both the strong interatomic potential and the quantum nature of the system. To perform this simulation, we have considered a system of $N = 64$ atoms interacting with the HFD-B(HE) Aziz potential [49] inside a cubic box, at different temperatures and at the equilibrium density measured experimentally at each temperature [50].

The first quantity we compute is the total energy per particle E/N: in Fig. 2.8, we show our PIMC results for E/N and we compare them with the experimental measurement by Crawford [51]. We can see that the PIMC results for the energy as a function of the temperature present the same behavior as the experimental data, even if our numerical values for E/N are slightly lower than Crawford's measurements, in an amount of ~ 0.20 K. A similar discrepancy has been obtained also in a previous calculation [4] and can be attributable to the particular Aziz potential used in the present simulation. The disagreement between the PIMC and the experimental result increases close to the superfluid transition temperature $T_\lambda = 2.17$ K, since the computer simulation, because of finite size effects, is not able to reproduce accurately the kink in $E(T)$ at T_λ.

To investigate the microscopic structure of the simulated system we have computed the two-body radial distribution function $g(r)$. Our result of $g(r)$ at the temperature $T = 1.2$ K and density $\rho = 0.02184$ Å^{-3} is shown in Fig. 2.9 and is in excellent agreement with experimental data [52].

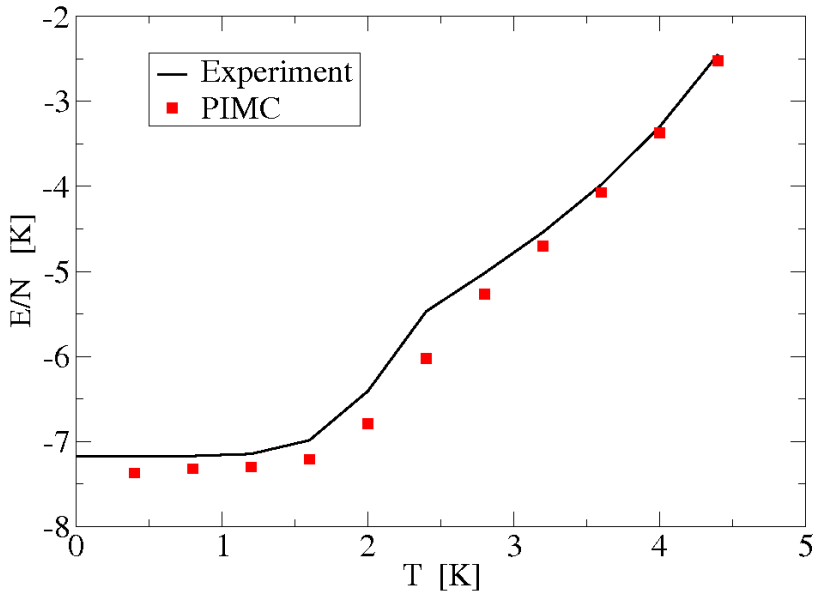

Figure 2.8: Energy per particle in the system of $N = 64$ ^{4}He atoms at the SVP density as a function of the temperature: the red squares are the PIMC results (statistical error are below symbol size) and the straight black line is the experimental measurement taken from Ref. [51].

In order to check if the worm algorithm can provide a good sampling of the permutations even in strongly interacting systems, it is important to calculate the properties strictly connected with the quantum nature of the system, such as the condensate or the superfluid fraction. At first, we have computed the one-body density matrix $\rho_1(r)$: we have performed this calculation in a system larger than the ones used in previous simulations, made up of $N = 128$ atoms, in order to see more clearly the long range behavior of $\rho_1(r)$. The result for a system at the temperature $T = 1.2$ K and density $\rho = 0.02184$ Å^{-3} is shown in Fig. 2.10: we can easily see that, at large r, $\rho_1(r)$ does not vanish, but presents a plateau at a non zero value indicating the presence of Bose-Einstein condensation in the system. The estimated condensate fraction is $n_0 = 0.072 \pm 0.002$.

Finally, we have also studied the dependence of the superfluid fraction ρ_s/ρ as a function of the temperature. Our results, both for the system of 64 and 128 ^{4}He atoms, are shown in Fig. 2.11 and compared to the experimental measurements [53]. At very low temperature ($T < 2$ K), our data are in good agreement with experimental ones, even though they present a quite large statistical error. Indeed, it is hard to estimate accurately the superfluid fraction by means of the mean-squared winding number because changes in $\mathbf{W}$ involve global moves of the paths and do not occur with high frequency during the Metropolis sampling of the coordinates.

Close to T_λ, the discrepancies between PIMC and experimental data increase.

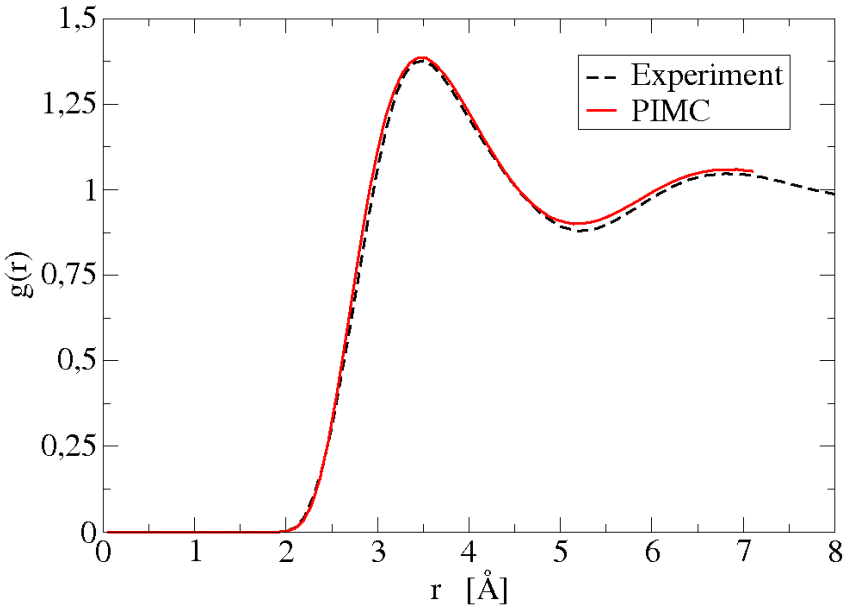

Figure 2.9: Two-body radial distribution function for liquid ^{4}He. The red straight line is the result obtained in PIMC simulation at temperature $T = 1.2$ K and density $\rho = 0.02184$ Å^{-3}; the black dashed line is the experimental measurement at the equilibrium density at $T = 1$ K, taken from Ref. [52]

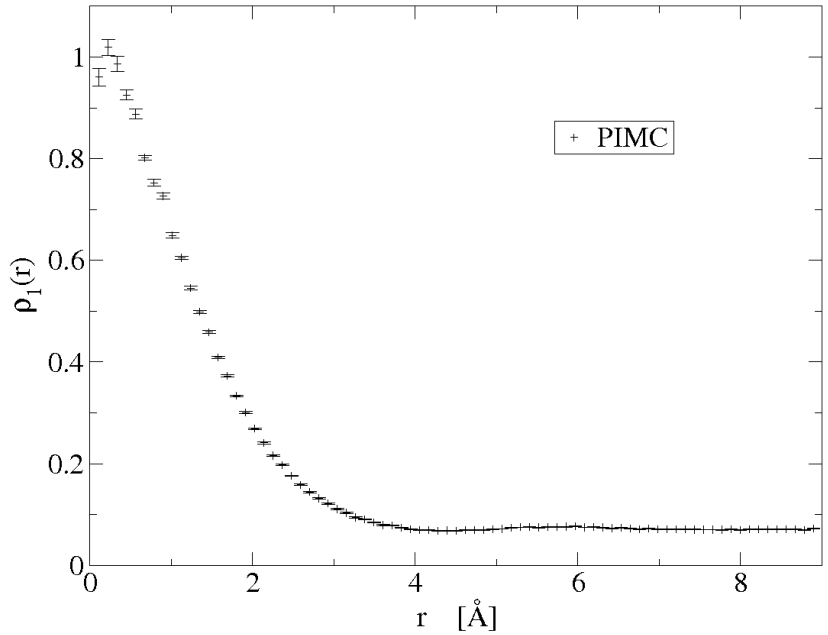

Figure 2.10: One-body density matrix for liquid ^{4}He at temperature $T = 1.2$ K and density $\rho = 0.02184$ Å^{-3}.

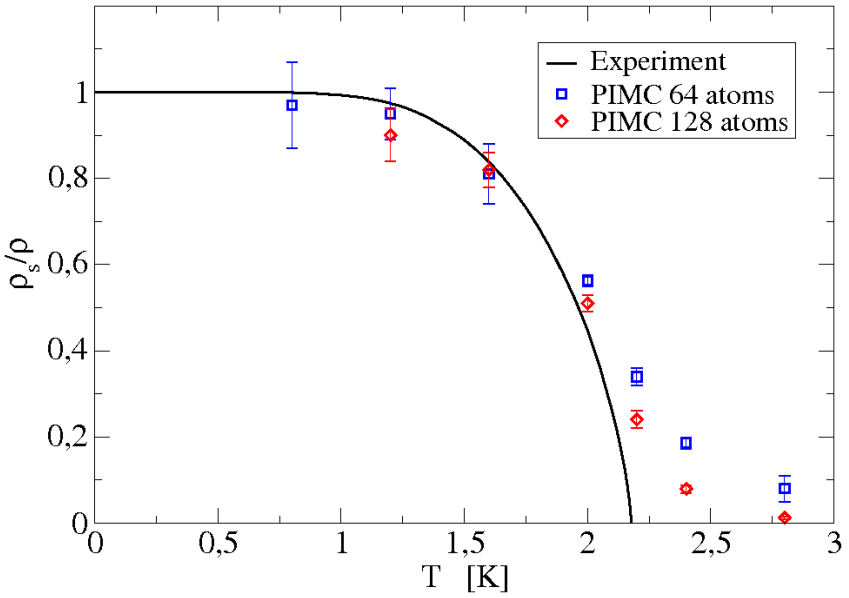

Figure 2.11: Superfluid density for liquid ^{4}He at the equilibrium density as a function of the temperature: the straight black line is the experimental measurement taken from Ref. [53]; symbols are the results obtained from PIMC simulation (blue squares and red diamonds are respectively the result obtained in the simulation of $N = 64$ and $N = 128$ ^{4}He atoms).

For the system of 64 atoms, we see that ρ_s decays to zero at high T in a smoother way in comparison with the experimental behavior. This effect is due to the finite size of the simulation box: it can be partially corrected considering larger systems, as we can see from the PIMC result of the simulation of the system made up of 128 ^{4}He atoms. To extrapolate the value of the superfluid density in the thermodynamic limit from the PIMC data, and thus to estimate the critical temperature for the superfluid transition, it would be necessary to perform simulations of larger systems, which are quite demanding from the computational point of view, and then to carry out a finite-size scaling analysis [54]. Nevertheless, the possibility of reproducing quite well the behavior of the superfluid density in a system of 128 ^{4}He atoms represents a big improvement in the sampling of permutations with respect to conventional techniques. Indeed, as pointed out by Ceperley in Ref. [18], without the worm algorithm it is possible to calculate the superfluid fraction of many-body system only in small systems containing no more than 100 particles.

In conclusion, this last test has shown that, by means of the PIMC method with the worm algorithm, it is possible to reproduce the main static properties of bulk liquid ^{4}He. We can therefore assume that our method is able to give a complete and accurate description of quantum systems, even in case of high degeneracy and strong interaction between the atoms.

Chapter 3

Zero temperature calculations: the Path Integral Ground State method

In this chapter, we present an extension of the Path Integral Monte Carlo method to the simulation of quantum systems at zero temperature, usually called *Path Integral Ground State* (PIGS) method. After a short introduction of the subject recalling the formalism of the method, we examine the possibility of improving the quality of the ground state wave function with the choice of a good approximation for the propagator in imaginary time. The efficiency of the method makes possible to obtain completely model independent results with a very small number of beads. Finally, we discuss also the improvement in the sampling scheme given by the implementation of the worm algorithm in these simulations.

3.1 Variational Monte Carlo and Path Integral Ground State methods

The Monte Carlo methods, that we briefly discussed in Sec. 2.1 showing the example of their application in the study of classical systems at finite temperature, are suitable also to compute the properties of quantum systems at zero temperature. The ground state average of an observable $\hat{O}$

$$\langle \Psi_0 | \hat{O} | \Psi_0 \rangle = \frac{\int d\mathbf{R}\, O(\mathbf{R}) \Psi_0^2(\mathbf{R})}{\int d\mathbf{R}\, \Psi_0^2(\mathbf{R})} \,. \tag{3.1}$$

can be calculated sampling the coordinates of the quantum system according to the probability distribution $\Psi_0^2(\mathbf{R}) / \int d\mathbf{R} \Psi_0^2(\mathbf{R})$. However, with respect to the Monte Carlo simulation of a classical system, the quantum case presents the additional difficulty that the ground state wave function is generally unknown and, to define the probability distribution used for the sampling of the coordinates, it is necessary to approximate $\Psi_0(\mathbf{R})$ with a trial wave function $\Psi_T(\mathbf{R})$.

The trial wave function must respect the postulates of quantum mechanics. In particular, it is necessary that $\Psi_T(\mathbf{R})$ respects the correct symmetry under the exchange of the particle labels: Ψ_T has to be symmetric when studying bosons and antisymmetric when studying fermions. Nonetheless, its choice can be made with a certain arbitrariness. To judge among a set of proposed forms of Ψ_T which is best,

we make use of the variational principle. This states that the ground state is the one which minimizes the energy functional

$$E[\Psi] = \langle \Psi | \hat{H} | \Psi \rangle \geq E_0 \ : \tag{3.2}$$

therefore, the better Ψ_T approximates Ψ_0, the lower is the value

$$E_T = \frac{\int d\mathbf{R}\, E_L(\mathbf{R}) \Psi_T^2(\mathbf{R})}{\int d\mathbf{R}\, \Psi_T^2(\mathbf{R})} \ , \tag{3.3}$$

where the quantity

$$E_L(\mathbf{R}) = \frac{\hat{H}\Psi_T(\mathbf{R})}{\Psi_T(\mathbf{R})} \ , \tag{3.4}$$

$\hat{H}$ being the Hamiltonian of the system, is called the *local energy*. The strategy generally followed in numerical simulation is therefore to construct a physically motivated wave function involving some free parameters and optimize these searching for the minimum of E_T.

The approach based on the use of Monte Carlo methods to perform numerically the calculation of E_T and the optimization of Ψ_T is referred to as *Variational Monte Carlo* (VMC). This method is easily implementable and it can provide approximated results with a little computational effort. However, its efficiency and its reliability depend strongly on the particular ansatz for the trial wave function. Furthermore, the results obtained with this method are affected by a systematic error which is difficult to quantify, especially the result for the total energy since, in accordance to the variational principle, E_T can be considered only an upper bound for the ground state energy [17].

It is therefore desirable to develop methods able to improve the quality of the trial wave function and thus to recover more reliable results for the ground state averages of the quantum system. An effective approach to accomplish this objective can be found in the solution of the Schrödinger equation in imaginary time $\tau = it$:

$$-\frac{\partial}{\partial \tau}\Psi(\mathbf{R};\tau) = \hat{H}\Psi(\mathbf{R};\tau) \tag{3.5}$$

Using the trial wave function to describe the initial condition $\Psi(\mathbf{R};0) = \Psi_T(\mathbf{R})$, the solution for Ψ at any imaginary time τ is

$$\Psi(\mathbf{R};\tau) = e^{-\tau\hat{H}}\Psi_T(\mathbf{R}) = \sum_{n=0}^{\infty} C_n \Psi_n(\mathbf{R}) e^{-\tau E_n} \tag{3.6}$$

where we indicate with Ψ_n the eigenstate of the Hamiltonian with eigenvalue E_n and we define $C_n = \langle \Psi_n | \Psi_T \rangle$.

For sufficiently large τ, only the eigenfunction with the lowest eigenvalue contributes to the sum in Eq. 3.6: this means that, if the trial wave function is not orthogonal to the ground state, $\Psi_0(\mathbf{R})$ can be written, except for a normalization factor, as

$$\Psi_0(\mathbf{R}) = \lim_{\tau\to\infty} \Psi(\mathbf{R};\tau) = \lim_{\tau\to\infty} \int d\mathbf{R}'\, G(\mathbf{R},\mathbf{R}';\tau)\Psi_T(\mathbf{R}') \ , \tag{3.7}$$

where $G(\mathbf{R}, \mathbf{R}'; \tau) = \langle \mathbf{R}|e^{-\tau \hat{H}}|\mathbf{R}'\rangle$. Eq. 3.7 tells us that the propagator $G(\mathbf{R}, \mathbf{R}'; \tau)$ for a sufficiently large imaginary time can be used to project a trial initial state onto the ground state. This result is at the basis of the formulation of many numerical methods known as *projection techniques*: among them, it is worth to mention the Green's Function Monte Carlo [17], Diffusion Monte Carlo [17] and Reptation Monte Carlo [55].

It is easy to notice that the imaginary time propagator G in Eq. 3.7 is equivalent to a thermal density matrix for a quantum system at temperature $T = 1/(k_B\tau)$. This means that we can write a very accurate approximation for the ground state wave function by means of the Path Integral formalism we have previously used to describe the properties of the quantum system at finite temperature. This approach is commonly known as the *Path Integral Ground State* (PIGS) method [56, 57, 58] and provides a technique to systematically improve a trial wave function which eventually drives the system into the ground state.

More precisely, the PIGS approach works constructing the propagator for the total imaginary time τ as a convolution of M propagators on a smaller time $\varepsilon = \tau/M$, for which it is possible to give a reliable approximation for G:

$$G(\mathbf{R}_M, \mathbf{R}_0; \tau) = \int \prod_{j=0}^{M-1} dR_j \, G(\mathbf{R}_{j+1}, \mathbf{R}_j; \varepsilon) \; . \tag{3.8}$$

Making use of the convolution property, we can rewrite Eq. 3.7 as

$$\Psi_0(\mathbf{R}) = \lim_{M\to\infty} \int \prod_{j=0}^{M-1} dR_j \, G(\mathbf{R}_{j+1}, \mathbf{R}_j; \varepsilon)\Psi_T(\mathbf{R}_0) \; . \tag{3.9}$$

Thus, if we fix a finite value for the integer M, we obtain an analytical form for the ground state wave function that can be used to perform numerical simulations,

$$\Psi_{PIGS}(\mathbf{R}_M) = \int \prod_{j=0}^{M-1} dR_j \, G(\mathbf{R}_{j+1}, \mathbf{R}_j; \varepsilon)\Psi_T(\mathbf{R}_0) \; . \tag{3.10}$$

At first sight, it seems that PIGS method is not so different from other variational methods: at the end, we have defined an ansatz $\Psi_{PIGS}(\mathbf{R})$ to approximate the ground state wave function and we use it to sample the coordinates and to compute the expectation values of the observables (indeed, in its first formulation PIGS was called *Variational Path Integral* method [18]). Nevertheless, the important novelty of the PIGS method with respect to VMC is the possibility to control the systematic error by means of the parameter M, which represents the number of convolution terms used in the approximation. Increasing M, we provide a better and better approximation for $\Psi_0(\mathbf{R})$ and the expectation value for the energy becomes smaller than the value E_T obtained with Eq. 3.3. At sufficiently large M, the value for the estimated energy will be independent on M, indicating that the systematic error due to the choice of $\Psi_T(\mathbf{R})$ has lowered below the statistical uncertainties and the

result can be considered an exact estimation of the ground state energy E_0; for this reason PIGS is referred to as an *exact* method.

Once we have determined the value of M for which $\Psi_{PIGS}(\mathbf{R})$ can provide a good description of the ground state, all the relevant properties of the quantum averages of the observables can be calculated with the formula

$$\begin{aligned}\langle\Psi_0|\hat{O}|\Psi_0\rangle &= \frac{\int d\mathbf{R}_M\, O(\mathbf{R}_M)\Psi^2_{PIGS}(\mathbf{R}_M)}{\int d\mathbf{R}_M\, \Psi^2_{PIGS}(\mathbf{R}_M)} \\ &= \frac{\int \prod_{j=1}^{2M} d\mathbf{R}_j\, O(\mathbf{R}_M)\Psi_T(\mathbf{R}_{2M})G(\mathbf{R}_j,\mathbf{R}_{j-1};\varepsilon)\Psi_T(\mathbf{R}_0)}{\int \prod_{j=1}^{2M} d\mathbf{R}_j\, \Psi_T(\mathbf{R}_{2M})G(\mathbf{R}_j,\mathbf{R}_{j-1};\varepsilon)\Psi_T(\mathbf{R}_0)} \end{aligned} \quad (3.11)$$

This integral can be computed via a Monte Carlo procedure, sampling the probability distribution

$$p(\mathbf{R}_0,\ldots,\mathbf{R}_{2M}) = \frac{\prod_{j=1}^{2M} \Psi_T(\mathbf{R}_{2M})G(\mathbf{R}_j,\mathbf{R}_{j-1};\varepsilon)\Psi_T(\mathbf{R}_0)}{\int \prod_{j=1}^{2M} d\mathbf{R}_j\, \Psi_T(\mathbf{R}_{2M})G(\mathbf{R}_j,\mathbf{R}_{j-1};\varepsilon))\Psi_T(\mathbf{R}_0)}\,, \quad (3.12)$$

This probability distribution can be seen as the Boltzmann distribution of a classical system of polymers, each one composed by $2 \times M + 1$ beads. Therefore, in close analogy with PIMC simulations at finite temperature, we can map the quantum N-particle system onto a classical system of N polymers, whose interaction is specified in the form used to approximate the propagator $G(\mathbf{R}_j,\mathbf{R}_{j-1};\varepsilon)$. Being G formally equivalent to a thermal density matrix, the probability distribution used in PIGS simulation, Eq. 3.12, is very similar to the one used in PIMC: thus the sampling scheme used for calculations at finite temperature can be easily extended to the zero temperature formalism.

The main discrepancy with respect to the calculation at finite temperature is that, in this case, we do not have to impose the periodic boundary conditions in imaginary time required by taking the trace of the propagator. For this reason, the quantum system is not isomorphous to a classical system of ring polymers but to a classical system of open polymers. On the configurations of the extreme points of these polymers, namely $\mathbf{R}_0$ and $\mathbf{R}_{2M}$, in addition to the interaction specified by the propagator G, we must also evaluate a special weight which depends on the choice of the trial wave function Ψ_T.

Another difference between PIMC and PIGS concerns the parameter ε. If in PIMC it is related to the temperature of the system, in PIGS it has no physical meaning and has to be considered as a variational parameter which has to be optimized, following the typical variational scheme of the minimization of the energy.

Notice that the conditions of indistinguishability of the quantum particles are accomplished in the PIGS method with a proper choice of the trial wave function and of the approximated form for the propagator. Thus, if $\Psi_T(\mathbf{R})$ is symmetric and the propagator is the one in Eq. 2.14 which is symmetric, there is no need of sampling the permutations between identical particles and single-polymers movements are sufficient to provide an ergodic sampling and a reliable calculation of the ground state averages.

Finally, it is important to make a remark in the choice of the trial wave function Ψ_T in the PIGS method. It has been found that the PIGS results are independent of Ψ_T and that they converge to the exact results even when the trial state contains no correlation at all ($\Psi_T = 1$) [59, 60]. The only influence of Ψ_T is on the convergence rate, since a judicious choice of Ψ_T would require a lower number M of beads to describe the ground state of the system. This result represents an improvement with respect to other projector Quantum Monte Carlo methods, such as Green Function or Diffusion Monte Carlo, where the trial wave function plays an important role in the importance sampling of the coordinates.

3.2 Estimators for the local energy

A remarkable feature of the PIGS method is the possibility it offers to evaluate the exact properties of the quantum system computing directly the pure estimator $\langle\Psi_0|\hat{O}|\Psi_0\rangle$. In many Quantum Monte Carlo techniques, only the mixed estimator $\langle\Psi_T|\hat{O}|\Psi_0\rangle$ are easily accessible, while the pure estimators are obtained through a forward walking algorithm [61].

In the PIGS method we can calculate, according to Eq. 3.11, the pure estimator of any observable $\hat{O}$ evaluating directly $O(\mathbf{R}_M)$, that is evaluating the observable on the configuration of the beads exactly at the center of the open polymers. The definition of the estimators $O(\mathbf{R}_M)$ is straightforward for the observables which are diagonal in the space of coordinates, such as the potential energy or the pair distribution function. Instead, it is more involved in the case of observables which depend on the coordinates of the system in two different imaginary time: among them, it is important to mention the local energy $E_L(\mathbf{R}_M)$, Eq. 3.4, whose average provides the ground state energy of the system and has to be used in the study of the convergence of $\Psi_{PIGS}(\mathbf{R}_M)$, Eq. 3.10, to $\Psi_0(\mathbf{R}_M)$ as the number of beads M increases. The definition of $E_L(\mathbf{R}_M)$ directly from the evaluation of $\hat{H}\Psi_{PIGS}$ can be hard because the definition of $\hat{H}\Psi_{PIGS}$ would require the computation of the first and of the second derivatives of $G(\mathbf{R}_M, \mathbf{R}_{M-1}; \varepsilon)$, resulting in a formula for $E_L(\mathbf{R}_M)$ which in many cases is difficult to implement.

In order to overcome this problem, there are many ways which can be followed. The most common strategy is to evaluate the ground state energy using the mixed estimator $\langle\Psi_0|\hat{H}\,|\Psi_T\rangle$. Indeed, we can easily demonstrate that, within the PIGS approach, the mixed estimator for any observable $\hat{O}$ commuting with the Hamiltonian is exact:

$$\langle\Psi_0|\hat{O}|\Psi_0\rangle = \lim_{\tau\to\infty}\langle\Psi_T|e^{-\tau\hat{H}}\hat{O}e^{-\tau\hat{H}}|\Psi_T\rangle = \lim_{\tau\to\infty}\langle\Psi_T|e^{-2\tau\hat{H}}\hat{O}|\Psi_T\rangle = \langle\Psi_0|\hat{O}|\Psi_T\rangle\ , \tag{3.13}$$

where in the second equality we have made use of the commutativity of the observable $\hat{O}$ with $\hat{H}$, and thus with $e^{-\tau\hat{H}}$, to move $\hat{O}$ and to apply it directly to $|\Psi_T\rangle$. This result tells us that the estimator for the local energy can be obtained

computing $\hat{H}\Psi_T(\mathbf{R})$ instead of $\hat{H}\Psi_{PIGS}(\mathbf{R})$, in order to recover the simpler form

$$E_L(\mathbf{R}) = -\frac{\hbar^2}{2m}\frac{\nabla^2\Psi_T(\mathbf{R})}{\Psi_T(\mathbf{R})} + V(\mathbf{R}) \ . \tag{3.14}$$

This estimator is able to provide reliable and precise results for the expectation values of the ground state energy, but requires the knowledge of a reasonable approximation of the ground state wave function. Indeed, if Ψ_T is not sufficiently accurate to describe the ground state, the local energy estimator given in Eq. 3.14 suffers the drawback of a large variance.

Therefore, it is very important to develop other estimators for the local energy which can be used in the general case of systems whose ground state wave function is poorly known. An alternative estimator can be obtained from the identity

$$\lim_{\tau\to\infty}\frac{\partial}{\partial\tau}\ln\langle\Psi_T|e^{-\tau\hat{H}}|\Psi_T\rangle = \lim_{\tau\to\infty}\frac{\langle\Psi_T|e^{-\tau\hat{H}}\hat{H}|\Psi_T\rangle}{\langle\Psi_T|e^{-\tau\hat{H}}|\Psi_T\rangle} = \langle\Psi_0|\hat{H}|\Psi_0\rangle \ . \tag{3.15}$$

According to this equation, we can deduce the local energy estimator evaluating the derivative of the propagator $G(\mathbf{R}_{2M}, \mathbf{R}_0; \tau)$ with respect to the imaginary time τ, in the same way as we have deduced the energy estimator in PIMC simulations at finite temperature (Sec. 2.5.1). Following this approach, we will get an estimator which does not depend only on the configuration $\mathbf{R}_M$ of the mid points of the PIGS polymers, but also on all the configurations $\{\mathbf{R}_0, \ldots, \mathbf{R}_{2M}\}$ representing the whole propagation in the imaginary time τ. More precisely, we get

$$\begin{aligned} E_L(\mathbf{R}_0, \ldots, \mathbf{R}_{2M}) \ = \ & \frac{3N}{2\tau} + \frac{(\mathbf{R}_{2M} - \mathbf{R}_0)(\mathbf{R}_{2M-1} - \mathbf{R}_{2M})}{4\lambda\varepsilon\tau} + \\ & + \frac{1}{\tau}\sum_{l=1}^{2M-1}(\mathbf{R}_l - \mathbf{R}_0)\frac{\partial}{\partial\mathbf{R}_l}(U(\mathbf{R}_{l+1}, \mathbf{R}_l; \varepsilon) + U(\mathbf{R}_l, \mathbf{R}_{l-1}; \varepsilon)) \\ & + \frac{1}{2M}\sum_{l=1}^{2M}\frac{\partial U(\mathbf{R}_l, \mathbf{R}_{l-1}; \varepsilon)}{\partial\varepsilon} \ . \end{aligned} \tag{3.16}$$

Notice that this equation for E_L is equivalent to the virial estimator for the energy at finite temperature, obtained after the redefinition of the harmonic terms proportional to $(\mathbf{R}_j - \mathbf{R}_{j-1})^2$ coming from the derivation of the gaussians in the kinetic contribution to the imaginary time propagator, as shown in appendix B.

The estimator in Eq. 3.16 can be more robust than the one in Eq. 3.14 since it is totally independent of the choice of the trial wave function and can be used in a large number of cases. However, it presents a higher variance in comparison with E_L of Eq. 3.14. Furthermore, Eq. 3.16 is exact only in the limit of $\tau \to \infty$ and cannot be used for variational calculations.

In the general case of a not accurate trial wave function and of a number of beads M out of convergence, the only approach to get an estimator for the local energy is to compute it directly from the definition of Ψ_{PIGS}. It is possible to write the imaginary time propagator in forms which are easily derivable and allow

for an easy definition of the local energy estimator. In particular, if we define the imaginary time propagator $G(\mathbf{R}_j, \mathbf{R}_{j-1}; \varepsilon)$ in a symmetrized form where we put the kinetic contribution at the extremities and we evaluate the potential action in an inner configuration $\mathbf{R}'_j$, as in

$$G(\mathbf{R}_j, \mathbf{R}'_j, \mathbf{R}_{j-1}; \varepsilon) = \frac{1}{(4\pi\lambda\varepsilon)^{3N/2}} e^{-\frac{(\mathbf{R}_j - \mathbf{R}'_j)^2}{4\lambda\varepsilon}} e^{-\varepsilon W(\mathbf{R}'_j)} e^{-\frac{(\mathbf{R}'_j - \mathbf{R}_{j-1})^2}{4\lambda\varepsilon}} , \qquad (3.17)$$

the calculation of $\nabla^2 \Psi_{PIGS}(\mathbf{R}_M)$ is simpler since, if we substitute Eq. 3.17 in Eq. 3.10, the configuration $\mathbf{R}_M$ appears in the expression of $\Psi_{PIGS}(\mathbf{R}_M)$ only as argument of a gaussian term, making thus Ψ_{PIGS} easily derivable. With this assumption, we get the following estimator for the local energy:

$$E_L(\mathbf{R}_M, \mathbf{R}'_M, \mathbf{R}_{M-1}) = \frac{3}{2\varepsilon} - \frac{1}{4\lambda\varepsilon^2}(\mathbf{R}_M - \mathbf{R}_{M-1})^2 + V(\mathbf{R}'_M) . \qquad (3.18)$$

In practice, to use this estimator we have to focus on a central link of the PIGS polymer: the kinetic energy is computed from the square distances of the extremities of the link considered, while the potential energy is computed on a configuration $\mathbf{R}'_M$ sampled according the distribution $p_L(\mathbf{R}'_M) = \rho_F(\mathbf{R}_M, \mathbf{R}'_M; \varepsilon/2)\rho_F(\mathbf{R}'_M, \mathbf{R}_{M-1}; \varepsilon/2)$, where ρ_F is the kinetic energy propagator, Eq. 2.16. The term $p_L(\mathrm{R}'_M)$ can be easily rewritten as a gaussian centered in $(\mathbf{R}_M + \mathbf{R}_{M-1})/2$ and with standard deviation $\sigma = \sqrt{\hbar^2\varepsilon/m}$, so that the configuration $\mathbf{R}'_M$ is not difficult to sample.

The main advantage of the estimator for the local energy written in Eq. 3.18 is its easy implementation and its complete generality. However, it suffers from a large variance and needs long simulation runs in order to lower the statistical error in the estimation of the ground state average of the Hamiltonian. For this reason, we use this estimator especially in variational calculations performed with a limited number M of beads (typically $M = 1$) for which the sampling is not exceedingly demanding from the computational point of view.

In our simulations, we have implemented all the three estimators for the local energy we have discussed in the present section. According to the characteristics of every simulation, we have chosen which of is the optimal option. However, when more than one estimator is usable, we compute all of them and verify that they provide compatible results, in order to make ourselves sure of the reliability of the simulation.

3.3 Variational calculations

In previous sections, we have defined the PIGS method as exact in the sense that the systematic error can be controlled and lowered below the statistical one studying the convergence of the mean value of the energy as the number M of beads increases. However, the nature of this method is variational and, in principle, we can use the path integral formalism also to create a variational ansatz for the many-body wave function using a small number of beads out of convergence, typically using $M = 1$.

A well known example in this class of variational wave functions is the so called *Shadow Wave Function* (SWF)[62, 63]:

$$\Psi_{SWF}(\mathbf{R}) = \Psi_r(\mathbf{R}) \int d\mathbf{S}\, \Theta(\mathbf{R},\mathbf{S})\Psi_s(\mathbf{S}) \tag{3.19}$$

The term $\Theta(\mathbf{R},\mathbf{S}) = \exp(-C\sum_{i=1}^{N}|\mathbf{r}_i - \mathbf{s}_i|^2)$ is a gaussian kernel which provides a coupling between the real coordinates of the system $\mathbf{R} = \{\mathbf{r}_1,\ldots,\mathbf{r}_N\}$ and the auxiliary coordinates $\mathbf{S} = \{\mathbf{s}_1,\ldots,\mathbf{s}_N\}$ which, being integrated out, do not appear as explicit variables of the Ψ_{SWF} and are referred as shadow variables (C is a variational parameter). The function $\Psi_r(\mathbf{R})$ and $\Psi_s(\mathbf{S})$ are Jastrow type wave functions

$$\Psi_r(\mathbf{R}) = \prod_{i<j} e^{-\frac{1}{2}u(r_{ij})} \qquad \text{and} \qquad \Psi_s(\mathbf{S}) = \prod_{i<j} e^{-\frac{1}{2}u(s_{ij})}\ , \tag{3.20}$$

where the two-body correlations are described with a McMillan pseudopotential $u(r) = (b/r)^5$ (with b a variational parameter). The functional form in Eq. 3.20 is often used in the simulation of condensed matter systems since it is able to account for the two-body correlations at short range coming from the hardcore interatomic potential in a simple way. The SWF is able to improve the variational results obtained with a normal Jastrow wave function since, with the shadow variables, it introduces implicit correlations between more than two bodies, which play an important role in strongly interacting quantum systems.

It is easy to realize that the shadow wave function in Eq. 3.19 can be interpreted as a PIGS wave function, Eq. 3.10, with $M = 1$. Indeed, the function Ψ_s depends only on variables which are finally integrated and plays the same role as the trial wave function Ψ_T in Eq. 3.10. Furthermore, the gaussian kernel $\Theta(\mathbf{R},\mathbf{S})$ is similar to the kinetic contribution to the imaginary time propagator $G(\mathbf{R},\mathbf{S};\varepsilon)$ and thus the product $\Psi_r(\mathbf{R})\Theta(\mathbf{R},\mathbf{S})$ can be regarded as an approximation for $G(\mathbf{R},\mathbf{S};\varepsilon)$.

Nevertheless, this approximation is too simple and therefore it makes sense to ask if the results given by VMC with the SWF can be improved considering a better ansatz when the initial state is projected making use of a more accurate approximation for G. To accomplish this purpose, we have constructed a new shadowlike wave function making use of the Chin approximation for the imaginary time propagator [20]

$$e^{-\varepsilon\hat{H}} \simeq e^{-v_1\varepsilon\,\hat{W}_1}e^{-t_1\varepsilon\,\hat{K}}e^{-v_2\varepsilon\,\hat{W}_2}e^{-2t_0\varepsilon\,\hat{K}}e^{-v_2\varepsilon\,\hat{W}_2}e^{-t_1\varepsilon\,\hat{K}}e^{-v_1\varepsilon\,\hat{W}_1}\ , \tag{3.21}$$

with $\hat{W}_i = \hat{V} + u_0/(3v_i)\varepsilon^2\,[\hat{V},[\hat{T},\hat{V}]]$, and where the various factorization coefficients are all dependent on the single free parameter t_0 (Eqs. 2.29), obtaining thus the following ansatz for the variational wave function:

$$\begin{aligned}\Psi_{SC}(\mathbf{R}) \;=\; & \int d\mathbf{S_1}d\mathbf{S_2}d\mathbf{S_3}\, e^{-v_1\varepsilon W_1(\mathbf{R})}e^{-\frac{(\mathbf{R}-\mathbf{S}_1)^2}{4\lambda t_1\varepsilon}}e^{-v_2\varepsilon W_2(\mathbf{S}_1)}e^{-\frac{(\mathbf{S}_1-\mathbf{S}_2)^2}{8\lambda t_0\varepsilon}}\times \\ & \times e^{-v_2\varepsilon W_2(S_2)}e^{-\frac{(\mathbf{S}_2-\mathbf{S}_3)^2}{4\lambda t_1\varepsilon}}e^{-v_1\varepsilon W(\mathbf{S}_3)}\,\Psi_T(\mathbf{S}_3)\ .\end{aligned} \tag{3.22}$$

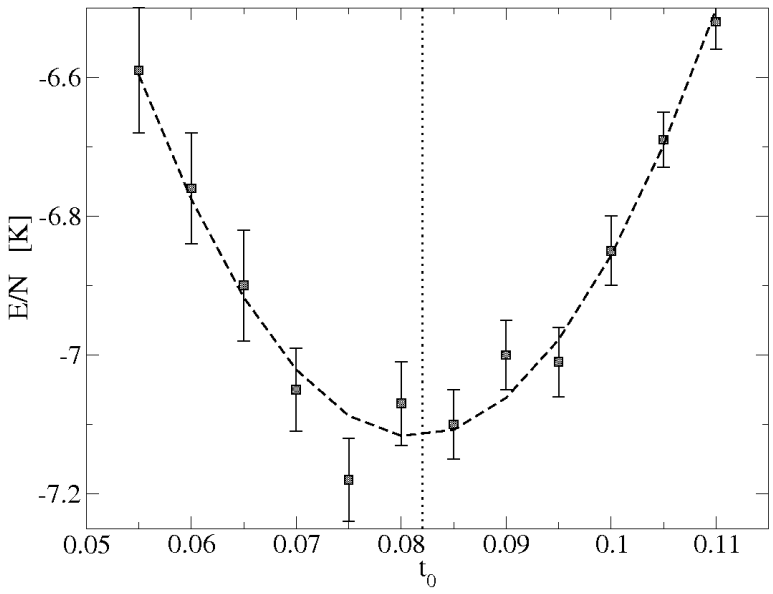

Figure 3.1: Variational energy obtained using the wave function Ψ_{SC} (Eq. 3.22) as a function of the free parameter t_0, with $\varepsilon = 0.06\,\mathrm{K}^{-1}$. The dashed line is obtained fitting our results with a quadratic function. The dotted line corresponds to the value $t_0 = 0.082$ obtained from the optimization at finite temperature.

In order to test the accuracy of the variational ansatz in Eq. 3.22, we have used it in the calculation of the energy of liquid ^{4}He at the equilibrium density. We have performed thus a simulation of $N = 64$ ^{4}He atoms interacting via the Aziz potential [49] at the density $\rho = 0.02186\,\text{Å}^{-3}$. As initial trial wave function, we make use of a Jastrow form based on the McMillan model, $\Psi_T(\mathbf{S}) = \prod_{i<j} \exp(-0.5(b/s_{ij})^5)$, that is the same trial wave function used in the first definition of the SWF, Eq. 3.19.

The first task for making our approximation for the ground state as accurate as possible is to optimize the variational parameters. We start from the optimization of the parameter t_0 used for the factorization of the evolution operator. Fig. 3.1 shows the results for the total energy of the system as a function of t_0 with a fixed $\varepsilon = 0.06\,\mathrm{K}^{-1}$. This value for ε is quite large if we consider that, in the PIMC simulations, the convergence of the Chin approximation to the exact imaginary time propagator is typically reached for $\varepsilon \leq 0.0125\,\mathrm{K}^{-1}$. However, at higher ε, the dependence of E/N on t_0 is stronger and this makes the optimization procedure easier. This effect has been shown also in the optimization procedure at a fixed finite temperature: in this case, the energy as a function of t_0 has an oscillating behavior which is more marked for a smaller number of beads, that is a higher value of the imaginary time step ε [20]. From Fig. 3.1, we can notice that the optimal parameter for t_0 is close to the value $t_0 = 0.082$ obtained at finite temperature: this supports the hypothesis for which the optimal values for the Chin approximation

ε [K^{-1}]	E/N [K]	
	Jastrow-McMillan	Constant
0.03	-7.14(9)	-6.49(12)
0.045	-7.15(8)	-6.88(8)
0.06	-7.10(5)	-6.91(6)
0.075		-6.77(5)
0.09		-6.44(4)

Table 3.1: Variational energy obtained using the wave function Ψ_{SC} (Eq. 3.22) as a function of the total imaginary time ε of the projection for different choice of the trial wave function Ψ_T. Figures in parentheses are the statistical errors.

depends uniquely on the Hamiltonian [37].

Having optimized the Chin parameter t_0, in Eq. 3.22 it remains another free parameter, ε, which is the total imaginary time of the propagation from the trial state $\Psi_T(\mathbf{S})$ to the final wave function $\Psi_{SC}(\mathbf{R})$. The optimization of this parameter represents the search for a compromise between a large ε value suitable for a large suppression of the excited components present in $\Psi_T(\mathbf{S})$, and a small one suitable for a proper behavior of the short-time approximation for the action. The dependence of the variational energy on the parameter ε is shown in Table 3.1. We can see that, in the case of a trial wave function of the Jastrow type, the result on the variational energy does not depend strongly on ε. Furthermore, we notice that the minimum energy obtained is $E/N = (-7.15 \pm 0.08)$ K: this result is only 0.17 K (two standard deviations) higher than the value $E_0 = -7.32$ K obtained with the PIGS method for a sufficiently large number of beads (see next section). It is very accurate if we consider that it has been obtained following a variational approach.

Equally impressive is the result obtained choosing a constant trial wave function $\Psi_T = 1$ in Eq. 3.22. The choice of this trial wave function, which is the ground state of an ideal Bose gas, represents an interesting variational calculation since, in this way, we get a completely general wave function where no more information than the Hamiltonian and the quantum statistics are used as input of the simulation. The results of the variational energy for different ε with this new choice of Ψ_T are also shown in Table 3.1: in particular, we have obtained a minimum energy $E/N = (-6.91 \pm 0.06)$ K. This result indicates that the use of a good approximation for the propagator provides by itself an impressive enhancement of the quality of the ground state wave function and makes possible to define a completely model independent ansatz which is able, in principle, to give accurate variational results even for systems whose ground state properties are poorly known or even unknown.

3.4 Exact simulations of liquid ^{4}He

The natural continuation of our study of liquid ^{4}He at zero temperature is to increase the number M of convolution terms in Ψ_{PIGS} in order to reach the asymp-

totic regime and finally obtain the ground state energy. In Fig. 3.2, we show the convergence of E/N at large imaginary time, both for the Jastrow $\Psi_T(\mathbf{R}_0) = \prod_{i<j} \exp(-0.5(b/r_{0_{ij}})^5)$ and for the constant trial wave function $\Psi_T(\mathbf{R}_0) = 1$. As the total imaginary time of the projection τ increases, the total energy per particle E/N decreases indicating an improvement in the calculated variational energy. At large τ, the result for E/N converges to the value $E/N = -7.32$ K, that can be considered our estimation of the ground state energy E_0 of liquid ^{4}He at its equilibrium density. We can also notice that the result for E/N is independent of the choice of the trial wave function Ψ_T: this choice affects only the rate of convergence of the variational results to the exact one, since a trial wave function which is able to describe accurately the ground state does not need a large time τ to reach the asymptotic regime. In particular, to project a Jastrow wave function onto the ground state we need an imaginary time $\tau = 0.1\,\mathrm{K}^{-1}$, while the constant wave function reaches the convergence at $\tau = 0.1875\,\mathrm{K}^{-1}$. Having chosen an imaginary time step $\varepsilon = 0.0125\,\mathrm{K}^{-1}$ for which we can be sure of the accuracy of the propagator $G(\mathbf{R}_j, \mathbf{R}_{j-1}; \varepsilon)$, this means that we get the exact value of the energy with $M = 8$ and $M = 15$ beads respectively for the Jastrow and for the constant wave function. The number of beads can be reduced considering a larger ε: in this case the approximation for the propagator is worst and the total imaginary time τ to achieve convergence may be larger. For instance, in a PIGS simulation with the choice of the McMillan form for Ψ_T and $\varepsilon = 0.045\,\mathrm{K}^{-1}$, we get the convergence at $\tau = 0.18\,\mathrm{K}^{-1}$, which means $M = 4$ beads. Anyway, we have to remark that in both cases we are able to recover the exact result for the energy with a very small number of beads.

Once we have found the number of beads M needed to provide a good description of the ground state with Ψ_{PIGS}, Eq. 3.10, we can calculate unbiased estimations of other operators $\hat{O}$ by evaluating them in the configuration $\mathbf{R}_M$ at the center of the chain. As an example, we plot in Fig. 3.3 the radial distribution function $g(r)$. We can notice that our results are independent of the choice of the trial wave function Ψ_T and are in excellent agreement with experimental data.

Another relevant quantity that can be computed exactly with the PIGS method is the one-body density matrix $\rho_1(r)$, whose asymptotic limit is the condensate fraction. Knowing the ground state wave function of a quantum many-body system $\Psi_0(\mathbf{R})$, the one-body density matrix (OBDM) can be written as

$$\rho_1(\mathbf{r}_1, \mathbf{r'}_1) = \frac{\int d\mathbf{r}_2 ... d\mathbf{r}_N \Psi_0^*(R)\Psi_0(R')}{\int d\mathbf{r}_1 ... d\mathbf{r}_N |\Psi_0(R)|^2} \ , \tag{3.23}$$

where the configuration $R = \{\mathbf{r}_1, \mathbf{r}_2, ..., \mathbf{r}_N\}$ differs from $R' = \{\mathbf{r'}_1, \mathbf{r}_2, ..., \mathbf{r}_N\}$ only by the position of one of the N atoms. In the PIGS approach, the expectation value of non-diagonal observables, like ρ_1, is computed mapping the quantum system in the same classical system of polymers discussed in Sec. 3.1, but cutting one of these polymers in the mid point. Building the histogram of the frequencies of the distances between the cut extremities of the two half polymers, one can compute the numerator in Eq. (3.23). The calculation of the normalization factor at the denominator is not strictly necessary since the histogram can be normalized

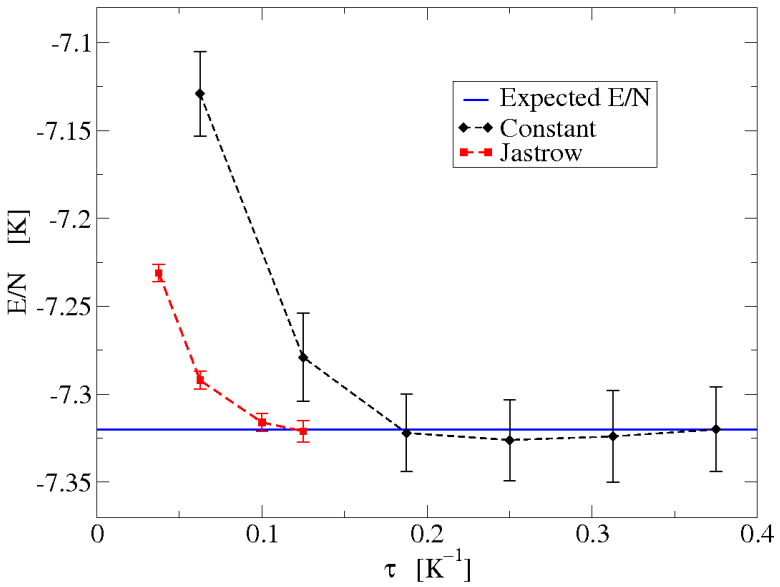

Figure 3.2: Total energy per particle E/N of liquid ^{4}He at the equilibrium density as a function of the total projection time τ obtained from PIGS simulation by projecting a trial Jastrow (red squares) and constant wave function (black diamonds). The straight blue line represents the asymptotic value for the ground state energy $E/N = -7.32$ K.

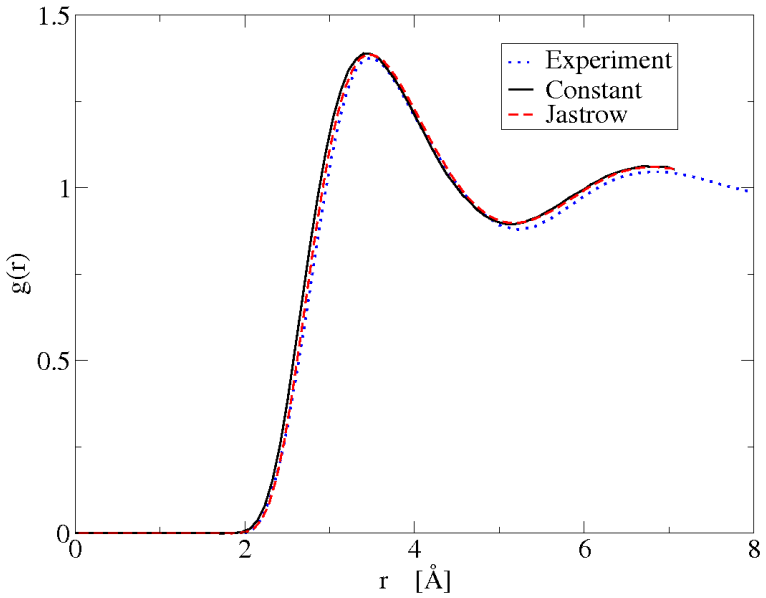

Figure 3.3: Two-body radial distribution $g(r)$ of liquid ^{4}He at zero temperature and density $\rho = 0.02186\,\text{Å}^{-3}$. The black solid and the red dashed lines correspond to the PIGS results at density $\rho = 0.02186\,\text{Å}^{-3}$ with different choice of Ψ_T, respectively $\Psi_T = 1$ and Ψ_T of the Jastrow form. The dashed line represents the experimental data from Ref. [52]

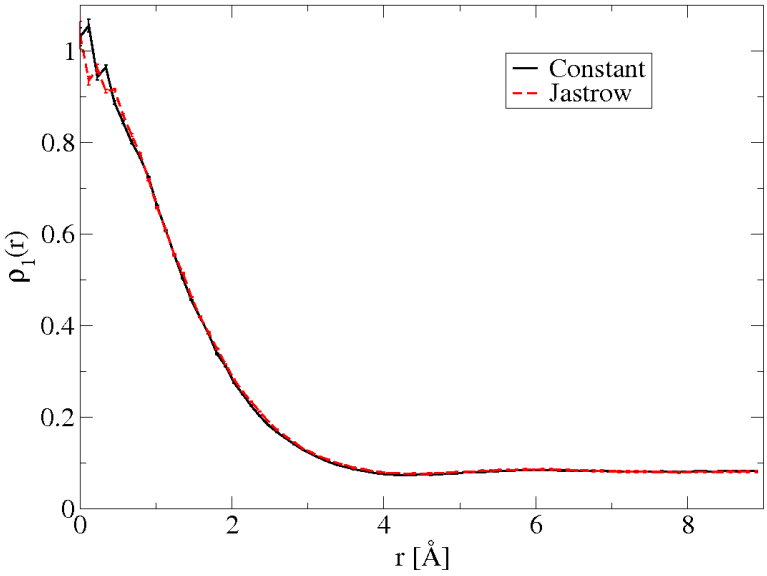

Figure 3.4: One-body density matrix $\rho_1(r)$ of liquid ^{4}He at zero temperature and density $\rho = 0.02186\,\text{Å}^{-3}$. The black solid and the red dashed lines correspond to the PIGS results at density $\rho = 0.02186\,\text{Å}^{-3}$ with different choice of Ψ_T, $\Psi_T = 1$ and Ψ_T of Jastrow form respectively.

imposing the condition $\rho_1(0) = 1$. However, as in the case at finite temperature, this *a posteriori* normalization procedure is not easy, because of few occurrences of the distances close to zero, and may introduce systematic errors in the estimation of the condensate fraction n_0. To avoid this problem and to recover automatically the normalization condition of the OBDM, we have extended the worm algorithm also in the zero temperature PIGS method, implementing updates which allow to switch from diagonal (all polymers with the same length) to off-diagonal (one polymer cut in two separate halves) configurations and vice versa. The results for $\rho_1(r)$ obtained with the choice of two different Ψ_T are shown in Fig 3.4: these results are statistically indistinguishable and predict a condensate fraction $n_0 = 0.080 \pm 0.002$, in nice agreement with a recent PIMC estimation at $T = 1$ K ($n_0 = 0.081 \pm 0.002$) [7].

The capability of the PIGS wave function Ψ_{PIGS} (Eq. 3.10) to describe the ground state with a completely general ansatz, where all the relevant correlations between the particles arise directly from the Hamiltonian, suggests us the possibility to use the same wave function to describe both the liquid and the solid phase of ^{4}He. From the experimental observation at temperatures close to absolute zero, we know that ^{4}He at saturated vapor pressure is in the liquid phase, but it solidifies when an external pressure above 25 bar is applied to the sample. It would be interesting to understand if the function Ψ_{PIGS} could discriminate, according to the density of

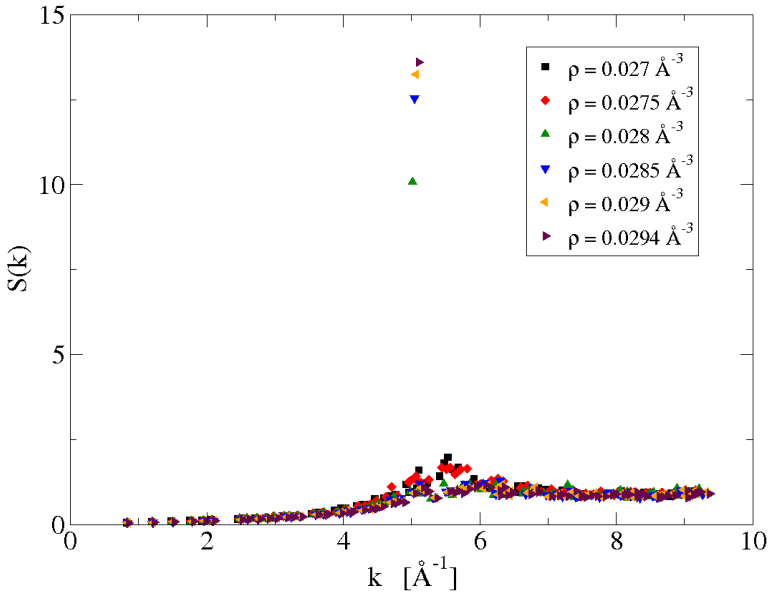

Figure 3.5: The static structure factor $S(k)$ resulting from PIGS simulations of 180 ^{4}He atoms at different densities with an ideal-gas trial wave function $\Psi_T = 1$.

the system, which is the equilibrium configuration between the crystalline and the liquid phase. A similar behavior has been found for the shadow wave function (Eq. 3.19) and represents a relevant property since it allows us to describe the crystalline phase without the definition of a set of *a priori* equilibrium positions for the atoms [62, 63].

In order to perform this study, we have carried out PIGS simulations with the choice $\Psi_T = 1$ of $N = 180$ ^{4}He atoms at different densities starting from the initial configuration of a commensurate hcp lattice. Our purpose is to investigate, for each density, if the crystalline phase remains stable during the whole simulation or if the system relaxes to a liquid configuration. To do that, we have computed the static structure factor $S(k)$, since the presence of Bragg peaks in $S(k)$ is a clear evidence of the solid order of the system. The results of this study are shown in Fig. 3.5: we notice that a peak in $S(k)$ is present at the highest densities, but disappears below the density $\rho = 0.028\,\text{Å}^{-3}$. This value is reasonably close to the experimental value for the melting density $\rho_m = 0.02862\,\text{Å}^{-3}$.

In conclusion, we have calculated with the PIGS method all the relevant properties of liquid ^{4}He at zero temperature, showing a good agreement between numerical and experimental results. Thanks to its capability to give accurate information about the physical system without any *a priori* knowledge of the ground state, the method is completely general and the same wave function can be used for simulating both the liquid and solid phases. These features make PIGS a really powerful method in the study of quantum fluids and solids at zero temperature.

3.5 Worm algorithm and Swap update in Path Integral Ground State

As we commented in Sec. 3.1, in the PIGS method the correct symmetry of the quantum many-body system can be obtained with a proper choice of the trial wave function and of the approximation for the imaginary time propagator, so that there is no need to perform a direct sampling of the permutations as in the case of PIMC at finite temperature.

The implementation of the worm algorithm, nevertheless, can be very useful in PIGS simulation because it provides an easy way to normalize automatically the OBDM $\rho_1(r)$ and thus to recover an unbiased estimation for the condensate fraction. The normalization factor of $\rho_1(r)$, indeed, can be estimated from the ratio between the number of diagonal and off-diagonal configurations sampled in the simulation (see appendix A.3). To calculate this ratio it is obviously necessary to extend the configurational space in order to include both diagonal and off-diagonal configurations, but there is no need to implement updates sampling the exchanges between bosons, like the Swap update.

However, the Swap update, if implemented in the sampling of the off-diagonal configurations, would be able to perform a large displacement of the extremities of the two half polymers in a single movement and could in principle influence the calculation of the OBDM. There is thus a certain interest in understanding how the implementation of updates proposing permutations between different PIGS polymers could affect the estimation of $\rho_1(r)$.

To perform this study we have simulated, with the PIGS method using a constant trial wave function $\Psi_T = 1$, the same system of $N = 64$ ^{4}He atoms inside a cubic box at the equilibrium density of the liquid phase ($\rho = 0.02186\,\text{Å}^{-3}$) following two different sampling schemes: we have implemented the Swap update in the first simulation but not in the second. The results for the OBDM are shown in Fig. 3.6. We can notice that the results for the different sampling scheme are statistically indistinguishable over the all range of r and lead to compatible results for the condensate fraction: $n_0 = 0.079 \pm 0.002$ for the case with Swap and $n_0 = 0.082 \pm 0.002$ for the case without Swap. This indicates that, at least in the simulation of the liquid phase, it is possible to provide an accurate sampling of the coordinates even without the Swap update. However, its implementation does not affect the simulation and there is no reason to remove it from the sampling scheme.

Nevertheless, we have to remark that the simulation of liquid ^{4}He may be not significant for the study of the influence of Swap in the computation of $\rho_1(r)$. Indeed, when the density of the system is not high, the PIGS open polymers can move with a certain facility, even if the sampling scheme include only updates which displace them on distances lower than the interatomic separation. It follows that it is not difficult for the half polymers to separate on distances comparable to the length of the simulation box and to recover in this way the correct behavior of $\rho_1(r)$ at large r.

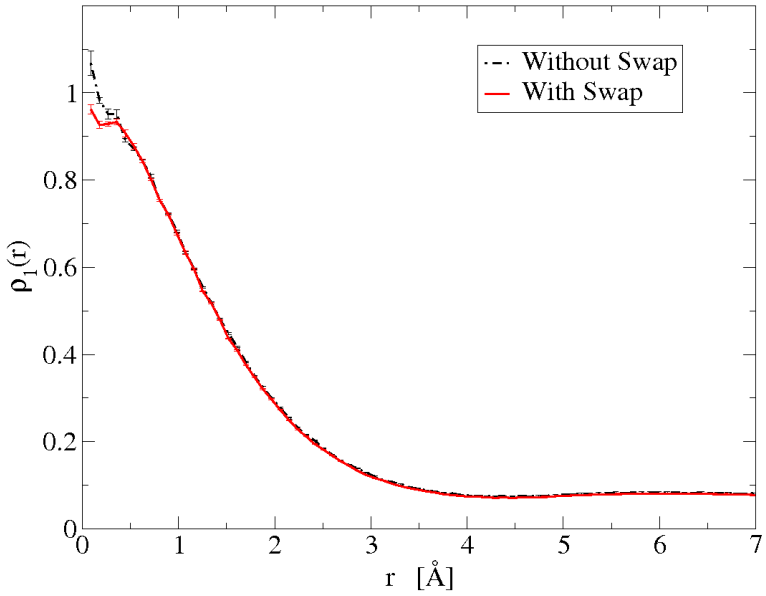

Figure 3.6: The one-body density matrix $\rho_1(r)$ for liquid ^{4}He at its equilibrium density $\rho = 0.02188\,\text{Å}^{-3}$ and at zero temperature, computed with PIGS method following two different sampling schemes, one including Swap updates and the other not.

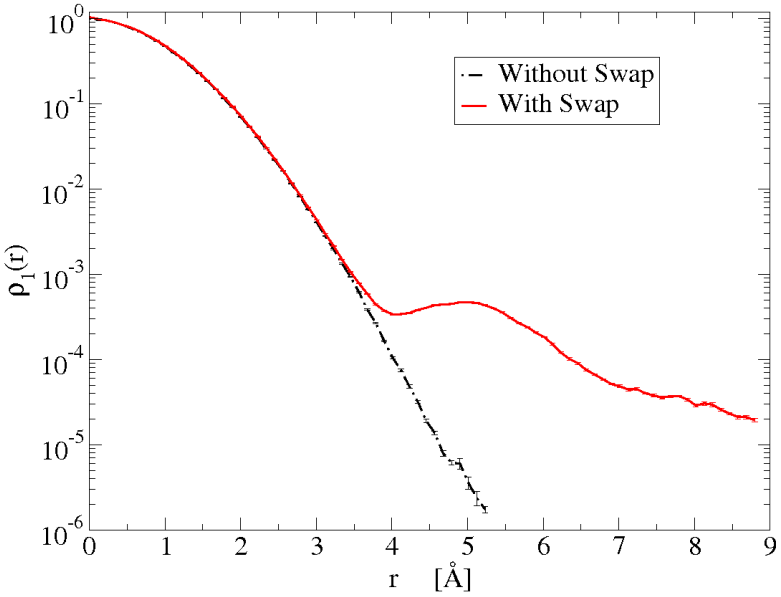

Figure 3.7: The one-body density matrix $\rho_1(r)$ for solid ^{4}He at density $\rho = 0.02186\,\text{Å}^{-3}$ and at zero temperature, computed with PIGS method following two different sampling schemes, one including Swap updates and the other not.

For this reason, it is worth performing the same study of the influence of the Swap update even for denser and more ordered systems, like solid ^{4}He, where the sampling of the coordinates is more difficult. We have carried out the calculation of the OBDM for a system made of $N = 180$ ^{4}He atoms disposed according to a commensurate hcp lattice in a quasi-cubic box following the same sampling schemes used previously, one performing Swap updates and the other not. The results of these simulations are showed in Fig. 3.7. We can notice that, in the range of small r, the two sampling schemes provide comparable results for $\rho_1(r)$ but they present a clear discrepancy at large r: the curve obtained without Swap presents a gaussian behavior, while the OBDM obtained with Swap shows an oscillating exponential decay at large r. The gaussian behavior is typical of classical crystals but it is not a feature of solid ^{4}He, as showed by some anharmonicity effects observed in the experimental measurement of the momentum distribution [64]; instead, the exponential behavior of $\rho_1(r)$ at large r found in the simulation presenting the Swap updates is in agreement with previous PIGS simulations [65] and with PIMC simulations at finite temperature [66]. To recover a similar behavior without implementing Swap, it is necessary to introduce an artificial potential between the cut extremities of the half polymers which should help them to move apart form each other. However, this potential is totally arbitrary and a bad choice may cause a loss of the ergodicity of the sampling, especially with respect to the balance with diagonal and off-diagonal configuration necessary to estimate the normalization factor of $\rho_1(r)$.

We can therefore conclude that, even if the worm algorithm is not strictly necessary in a PIGS simulation, unlike the case of PIMC at finite temperature where it is indispensable for the sampling of permutations, its implementation allows for sizeable improvements in the calculation of off-diagonal observables such as the one-body density matrix $\rho_1(r)$. In fact, it is able to provide not only a way to automatically normalize ρ_1, but it allows also a better sampling of the coordinates, especially in the simulation of solid systems where the atoms scarcely diffuse.

Chapter 4

One-body density matrix, momentum distribution and condensate fraction of liquid ^{4}He

In this chapter, we present results of the one-body density matrix $\rho_1(r)$ and the condensate fraction n_0 of liquid ^{4}He calculated at zero temperature by means of the Path Integral Ground State Monte Carlo method. This technique provides unbiased estimations of $\rho_1(r)$, from which we can obtain precise results for the condensate fraction n_0 and the kinetic energy K of the system. The dependence of n_0 with the pressure shows an excellent agreement of our results with recent experimental measurements. Above the melting pressure, overpressurized liquid ^{4}He shows a small condensate fraction that has dropped to 0.8% at the highest pressure of $p = 87\,\mathrm{bar}$.

4.1 Introduction

Several microscopic theories point out that the phenomenon of superfluidity in liquid ^{4}He has to be seen as a consequence of Bose-Einstein condensation (BEC)[67]. Having total spin $S = 0$, ^{4}He atoms behave like bosons and, below the critical temperature $T_\lambda = 2.17\,\mathrm{K}$, they can occupy macroscopically the same single-particle state. Nevertheless, the strong interaction between ^{4}He atoms does not allow all of them to occupy the lowest energy state and, even at zero temperature, only a small fraction $n_0 = N_0/N$ of the N particles is in the condensate.

Experimental estimates of n_0 can be obtained from the dynamic structure factor, $S(q,\omega)$, measured by inelastic neutron scattering at high energy and momentum transfer. These measurements have a long history [3, 68, 69]: in the 80s, the first experiments gave estimates for n_0 slightly above 10%, but they were affected by a poor instrumental resolution and by some difficulties in describing the final states effects of the scattering experiment. Recently, with the advances in the experimental technology and in the method of analysis of the scattering data, Glyde *et al.* [70] have been able to give improved estimations of n_0 at very low temperature. At saturated vapor pressure (SVP), they found $n_0 = (7.25 \pm 0.75)\%$ [70], and more recently they have measured the dependence of n_0 with pressure p [71].

Because of the strong correlations between ^{4}He atoms, the calculation of the one-body density matrix in superfluid ^{4}He cannot be obtained analytically via a perturbative approach. It is necessary the use of microscopic simulations to provide

accurate estimations of the condensate fraction. In particular, the Path Integral Monte Carlo (PIMC) method has been widely used in the study of ^{4}He at finite temperature, thanks to its capability of furnishing in principle exact numerical estimates of physical observables relying only on the Hamiltonian of the system [18]. The first calculations of n_0 with this method date back to 1987 [72], but most recent simulations based on an improved sampling algorithm provide very accurate results for $\rho_1(r)$, showing a condensate fraction $n_0 = 0.081 \pm 0.002$ at temperature $T = 1\,\mathrm{K}$ [7]. At zero temperature, ground-state projection techniques are widely used in the study of BEC properties of ^{4}He. Diffusion Monte Carlo technique, for instance, has provided estimations of n_0 in liquid ^{4}He on a wide range of pressures [4, 5, 73]. This method, however, suffers from the choice of a variational ansatz necessary for the importance sampling whose influence on $\rho_1(r)$ cannot be completely removed. Reptation Quantum Monte Carlo (RQMC) has also been used for this purpose [6], but the calculated value of n_0 at SVP lies somewhat below the recent PIMC value [7] at $T = 1\,\mathrm{K}$ noted above.

Motivated by recent accurate experimental data on $n_0(p)$, our aim is to perform new calculations of $\rho_1(r)$ and of n_0 in liquid ^{4}He using completely model-independent techniques based on path integral formalism. Using a good sampling scheme in our Monte Carlo simulations, we are able to provide very precise calculations of the one-body density matrix at different densities. We fit our numerical data for $\rho_1(r)$ with the model used in previous experimental works [70], highlighting the merits and the faults of this model, and finally we give our estimations for the condensate fraction at zero temperature when changing the pressure of the liquid, showing an excellent agreement with experimental data [71].

The chapter is organized as follows: section 4.2 is devoted to the analysis of the fit currently used in experimental measurements of $\rho_1(r)$; in section 4.3 we present the calculation of the momentum distribution at different finite temperatures; in section 4.4 we show how the condensate fraction n_0 changes as a function of the pressure p of the liquid.

4.2 Analysis of the fit for the one-body density matrix

To compute $\rho_1(r)$ in liquid ^{4}He at zero temperature, we have carried out different simulations using a cubic box with periodic boundary conditions containing $N = 128$ atoms interacting through the Aziz pair potential [49]. At first, we study the system at the equilibrium density $\rho = 0.02186$ Å^{-3}: our result for $\rho_1(r)$ is shown in Fig. 4.1. We have checked that our results starting with $\Psi_T = 1$ or with a Jastrow-McMillan wave function are statistically indistinguishable. In order to check how the finite size of the box affects our results, we have performed a simulation of the same system in a larger box containing $N = 256$ ^{4}He atoms. In Fig. 4.1, we have compared $\rho_1(r)$ obtained in this last simulation with the one estimated using a smaller number of particles: we can see that, up to the distances reachable with the smaller system, these two results agree within the statistical error. Furthermore, the

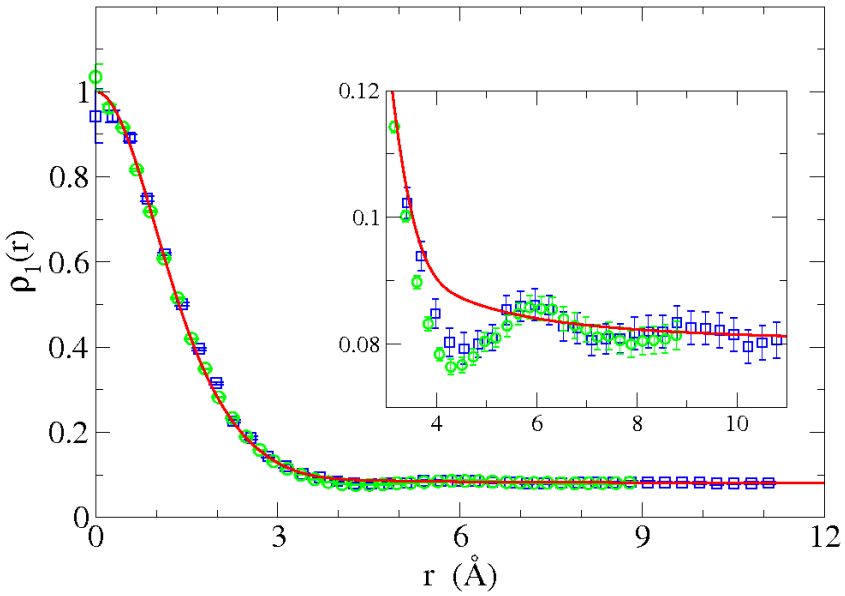

Figure 4.1: One-body density matrix $\rho_1(r)$ at the equilibrium density $\rho = 0.02186$ Å^{-3}. The symbols represents the result of the PIGS simulations for the system containing $N = 128$ (green circles) and $N = 256$ (blue squares) ^{4}He atoms. The red line is the curve obtained fitting these data with Eq. 4.1 with optimal values: $k_c = 1.369 \pm 0.020$ Å^{-1}, $\alpha_2 = 0.794 \pm 0.005$ Å^{-2}, $\alpha_4 = 0.355 \pm 0.050$ Å^{-4}, $\alpha_6 = 0.680 \pm 0.080$ Å^{-6}, and $n_0 = 0.0801 \pm 0.0022$. The inset shows the same data for r between 3 Å and 11 Å on an expanded scale.

two functions reach the same plateau at the largest available distances, indicating that the asymptotic regime for $\rho_1(r)$ is already achieved using $N = 128$ ^{4}He atoms.

To fit our data we use the model proposed by Glyde in Ref. [3] that has been used in the analysis of experimental data [70],

$$\rho_1(r) = n_0[1 + f(r)] + A\rho_1^*(r) \ . \tag{4.1}$$

The function $f(r)$ represents the coupling between the condensate and the non-zero momentum states. In momentum space, one can express $f(k)$ in terms of the phonon response function [3],

$$f(k) = \left[\frac{mc}{2\hbar(2\pi)^3\rho}\frac{1}{k}\coth\left(\frac{c\hbar k}{2k_BT}\right)\right] e^{-k^2/(2k_c^2)} \ , \tag{4.2}$$

with c the speed of sound. Since we work in the coordinate space, we are interested in its 3D Fourier transform $f(r)$, which at zero temperature can be written as

$$f(r) = \frac{mc}{\hbar(2\pi)^2\rho}\frac{\sqrt{2}k_c}{r}D\left(\frac{k_cr}{\sqrt{2}}\right) \ , \tag{4.3}$$

where $D(x) = e^{-x^2}\int_0^x dte^{t^2}$ is the Dawson function. To describe the contribution to ρ_1 from the states above the condensate, which we denote by ρ_1^*, we use the cumulant

expansion of the intermediate scattering function, that is the Fourier Transform of the longitudinal momentum distribution [3],

$$\rho_1^*(r) = \exp\left[-\frac{\alpha_2 r^2}{2!} + \frac{\alpha_4 r^4}{4!} - \frac{\alpha_6 r^6}{6!}\right] . \tag{4.4}$$

The constant A appearing in Eq. 4.1 is fixed by the normalization condition $\rho_1(0) = 1$. Therefore, the model we used has five parameters: n_0, k_c, α_2, α_4 and α_6. It has to be noticed that, unlike what is done in the treatment of the experimental data, where k_c is chosen as a cut-off parameter to make the term $f(k)$ vanish out of the phonon region, we have considered k_c as a free parameter of the fit.

The best fit we get using the model of Eq. 4.1 is shown in Fig. 4.1. This model is able to reproduce the behavior of $\rho_1(r)$ for short distances and in the asymptotic regime, but cannot describe well the numerical data in the range of intermediate r. Indeed, for distances above 3 Å, $\rho_1(r)$ obtained with PIGS presents oscillations which are damped at larger r, as observed also in previous theoretical calculations [6, 7]. This non monotonic behavior, which can be attributed to coordination shell oscillations [7], is difficult to describe within the model of Eq. 4.1.

Nevertheless, despite of these difficulties in describing the oscillations of the $\rho_1(r)$ obtained with PIGS, the fit we gave using the model of Eq. 4.1 contains important information about the ground state of liquid ^{4}He. First of all, from the long range behavior, we can obtain the value of the condensate fraction n_0. From our analysis, we get $n_0 = 0.0801 \pm 0.0022$, in complete agreement with the value $n_0 = 0.081 \pm 0.002$ obtained by Boninsegni *et al.* [7] in a path integral Monte Carlo simulation at temperature $T = 1\,\mathrm{K}$, and in good agreement with the experimental result $n_0 = 0.0725 \pm 0.0075$ [70]. Furthermore, from the behavior of $\rho_1(r)$ at short distances, we can obtain an estimation of the kinetic energy per particle K/N. In particular, the term α_2 appearing in Eq. 4.4 is the second moment of the struck atom wave vector projected along the direction of the incoming neutron [3] and is related to the kinetic energy per particle by the formula $K/N = 3(\hbar^2/2m)\alpha_2$. Using the value $\alpha_2 = (0.794 \pm 0.005)$ Å^{-2} obtained in our fit, we get $K/N = (14.43 \pm 0.09)\,\mathrm{K}$ which has to be compared with the value obtained in the PIGS simulation, $K/N = (14.37 \pm 0.03)\,\mathrm{K}$.

In Fig. 4.2, we show results of $n(k)$ obtained performing a numerical Fourier transform of $\rho_1(r)$ and we compare it with the Fourier transform of Eq. 4.1,

$$n(k) = n_0\delta(k) + n_0 f(k) + An^*(k) . \tag{4.5}$$

The PIGS data are plotted from $k_{min} = 2\pi/L \simeq 0.4$ Å^{-1} , L being the length of the simulation box, and are not able to reproduce the $1/k$ behavior of $n(k)$ at low k because of finite size effects; for $k > k_{min}$ the effect of $f(k)$ vanishes and $n(k) = n^*(k)$. We notice that the disagreement between the two curves is larger in the region between $k \simeq 1$ Å^{-1} and $k \simeq 2.5$ Å^{-1}. In this range, indeed, $n(k)$ obtained with the PIGS method presents a change of curvature, not seen in $n(k)$ obtained from the fit.

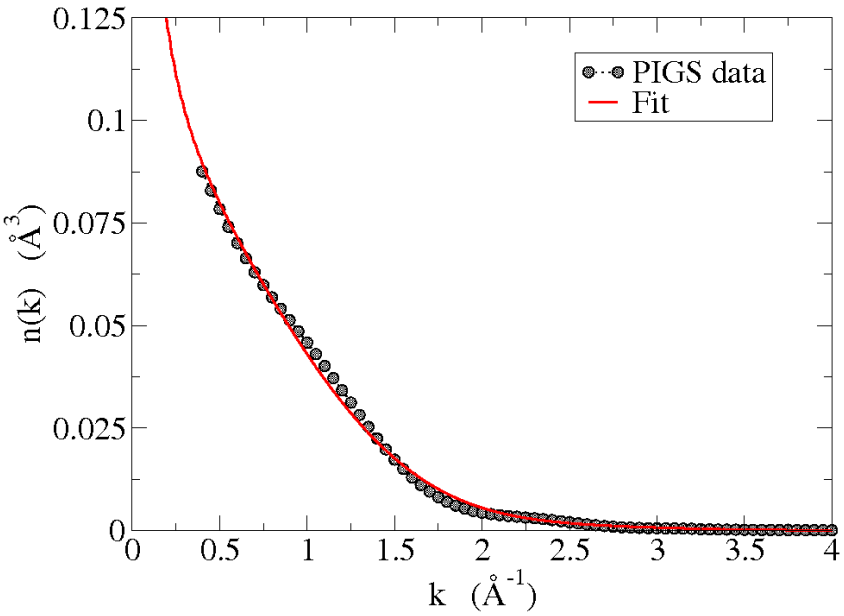

Figure 4.2: The momentum distribution $n(k)$ at equilibrium density $\rho = 0.02186$ Å^{-3}: the black circles represents the numerical result obtained from the PIGS simulation, the red line represents the FT of the fit for $\rho_1(r)$ obtained according to Eq. (4.1).

This discrepancy can be explained considering the coupling between the condensate and the states out of it. The term $f(k)$, defined in Eq. 4.2, is obtained considering only pure density excitations in the system and, therefore, is valid only in the limit of small momenta [3]. At higher k, one should consider even the contributions due to the coupling of the condensate to the excited states out of the phonon region. However, little is known about these contributions and it is difficult to include them in a more complete form for $f(k)$ in order to give a more reliable model for the momentum distribution.

Our results for $n(k)$ are compared with recent experimental measurements at $T = 0.06\,\mathrm{K}$ of the momentum distribution $n^*(k)$ for states above the condensate in Fig. 4.3. Even in this case, we can notice a good agreement between the two curves, except for the intermediate range of k, where our results include contributions arising from the coupling between the condensate and excited states. From the comparison between the two curves, we can deduce that this coupling contributes in depleting the states at higher k. In the same figure, in addition to $n(k)$ at the saturated vapor pressure, we also show $n(k)$ for a higher pressure, close to the freezing transition. We can see that the effect of the pressure in the momentum distribution is to decrease the occupancy of the low-momenta states and to make smoother the shoulder at $k \simeq 2$ Å^{-1}.

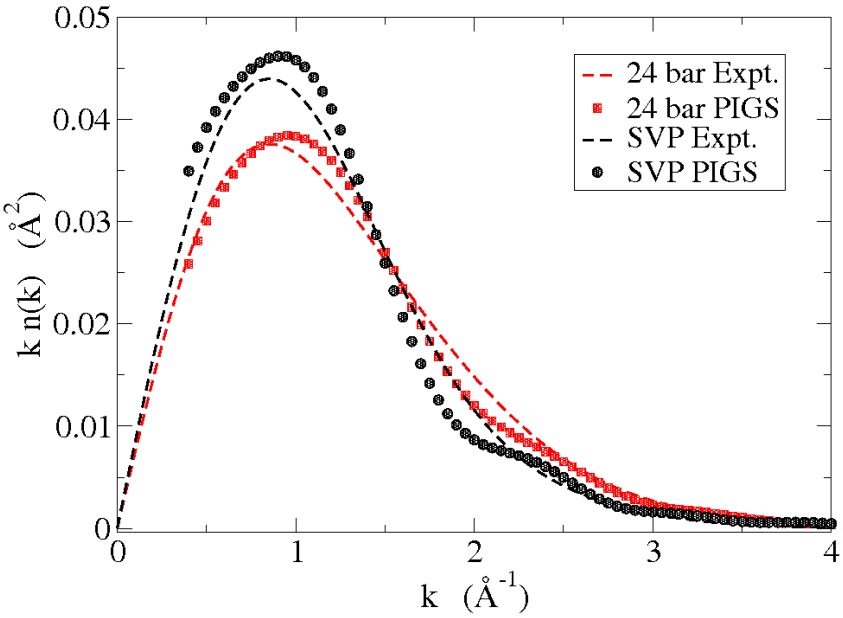

Figure 4.3: The momentum distribution, plotted as $kn(k)$, in liquid ^{4}He at two different pressures: black circles and red squares are the PIGS results for $n(k)$, respectively, at saturated vapor pressure ($\rho = 0.02186$ Å^{-3}) and at a pressure close to the freezing, $p \simeq 24$ bar ($\rho = 0.02539$ Å^{-3}). The black and the red dashed lines represent the experimental results for the momentum distribution above the condensate $n^*(k)$ at the same pressures [71].

4.3 Momentum distribution at finite temperature

In Figs. 4.2 and 4.3, we have seen that the momentum distribution at zero temperature computed with the PIGS method presents a change of curvature for k close to 2 Å^{-1}. A similar behavior in $n(k)$ has been obtained also from calculations performed within the scheme of hypernetted-chain equations using a variational wave function containing two-body (Jastrow) and three-body correlations [74].

To understand this behavior, we suggest the possibility of a coupling between the condensate and the excited states. In superfluid helium, there are two characteristic elementary excitations: the phonon in the region of low k and the roton at a higher momentum $k \simeq 2\,\text{Å}^{-1}$ [3]. In the momentum distribution $n(k)$ in Eq. 4.5, the coupling between the condensate and the phonons is taken into account by the term $f(k)$, but there is not a term describing the coupling between the condensate and the roton. We are led to think that the lack of this term can be at the origin of the difference between our result and the experimental one for the distribution $n^*(k)$ since the discrepancy appears clearly in the range of k corresponding to the excitation of the roton.

An easy way to check this hypothesis is to study the behavior of the momentum distribution at finite temperature, both in the superfluid and in the normal phase. If we see that the kink in $n(k)$ is present only in the superfluid region and disappears for temperature $T > T_\lambda$ for which there is not a Bose-Einstein condensate inside the liquid, the conjecture that the particular behavior of $n(k)$ is associated to a coupling between the condensate and the roton is plausible. With this objective, we have calculated the momentum distribution of liquid ^{4}He simulating $N = 128$ ^{4}He atoms inside a cubic box at different temperatures and at constant density $\rho = 0.02186\,\text{Å}^{-3}$, that is the equilibrium density for liquid ^{4}He at zero temperature. The results of these simulations are shown in Fig. 4.4. We can clearly see that the kink is pronounced for the lowest temperatures $T = 0$ K and $T = 1.2$ K, it becomes smoother at $T = 2.0$ K and disappears at the temperature $T = 3.2$ K, for which the liquid ^{4}He is normal. A similar behavior is shown also in the same study at the higher density $\rho = 0.02359\,\text{Å}^{-3}$: the only difference from the previous case at lower density is that the kink has already disappeared at the temperature $T = 2.0$ K, since the temperature of the superfluid transition decreases with the density and for $\rho = 0.02359\,\text{Å}^{-3}$ and $T = 2.0$ K the liquid ^{4}He is in the normal phase.

Therefore, this study seems to confirm our prediction that the appearance of a change of curvature in the momentum distribution close to $k \simeq 2\,\text{Å}^{-1}$ is related to the presence of the condensate in the system. Thus, we think that a model for $n(k)$ better than the one of Eq. 4.5 should be provided including in the theory the possibility for the condensate to couple with the roton excitation.

4.4 Pressure dependence of the condensate fraction

Finally, we report our results for the condensate fraction n_0 over a wide range of densities, including also densities in the negative pressure region and in the regime of

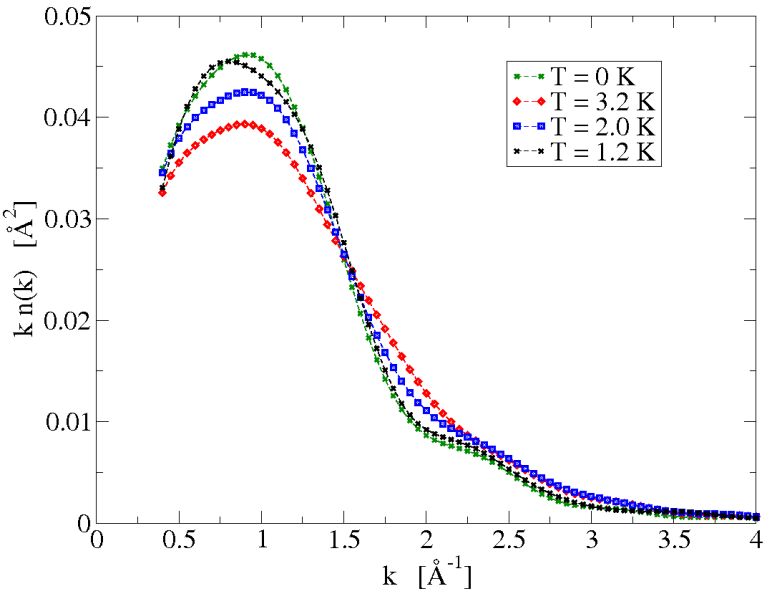

Figure 4.4: The momentum distribution, plotted as $kn(k)$, in liquid ^{4}He at the density $\rho = 0.02186\,\text{Å}^{-3}$ at different temperatures.

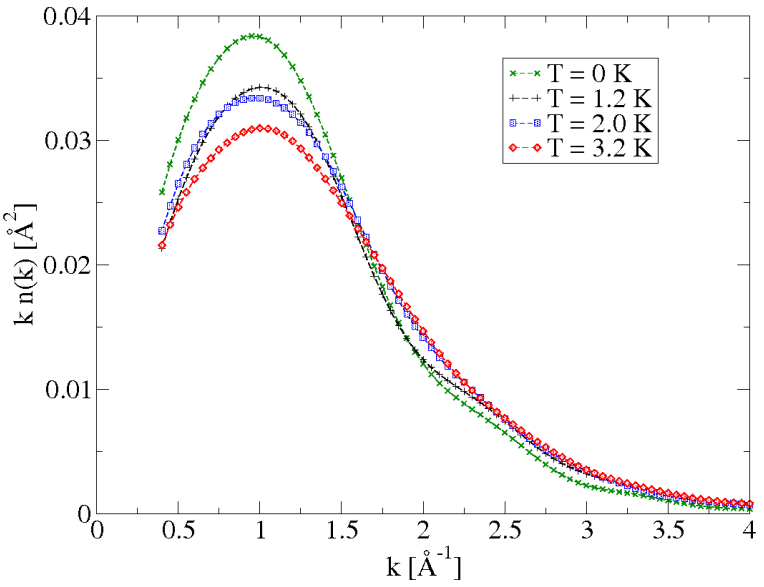

Figure 4.5: The momentum distribution, plotted as $kn(k)$, in liquid ^{4}He at the density $\rho = 0.02359\,\text{Å}^{-3}$ at different temperatures.

ρ [Å^{-3}]	p [bar]	n_0	K/N [K]
0.01964	-6.23	0.1157(19)	12.01(3)
0.02186	-0.04	0.0801(22)	14.37(3)
0.02264	3.29	0.0635(16)	15.35(3)
0.02341	7.36	0.0514(16)	16.28(3)
0.02401	11.07	0.0436(11)	17.02(4)
0.02479	16.71	0.0350(7)	18.08(4)
0.02539	21.76	0.0333(8)	18.82(5)
0.02623	29.98	0.0278(8)	19.99(4)
0.02701	38.95	0.0208(6)	21.08(5)
0.02785	50.23	0.0155(6)	22.24(4)
0.02869	63.37	0.0115(4)	23.65(4)
0.02940	76.28	0.0093(4)	24.83(5)
0.02994	87.06	0.0083(4)	25.61(6)

Table 4.1: Condensate fraction n_0 and kinetic energy per particle K/N as a function of the liquid density ρ. Numbers in parenthesis are statistical errors. The estimation of the pressure is obtained from the equation of state of liquid ^{4}He given in Ref. [73].

the overpressurized metastable fluid. In this range of high densities, we have been able to frustrate the formation of the crystal by starting the simulation from an equilibrated disordered configuration. The metastability of this phase is checked by monitoring how the total energy per particle E/N changes along the simulation. As the calculation goes on, we notice that E/N reaches a plateau for a value above the corresponding value of E/N computed in a perfect crystal at the same density. For instance, at density $\rho = 0.02940$ Å^{-3} we get in our simulation $E/N = (-5.48 \pm 0.03)$ K. If we perform a PIGS simulation at the same density and with the same choice for the initial trial wave function (in both cases, we choose in Eq. 3.10 $\Psi_T = 1$) but starting the computation from a hcp crystalline configuration, we get $E/N = (-5.95 \pm 0.02)$ K. The disagreement of the two results for E/N indicates that, in PIGS simulations, initial conditions for the atomic configuration influence the evolution of the system: in particular, a sensible choice of the initial conditions speed up the convergence of the system to the real equilibrium state. In the simulation of ^{4}He at high densities, if we use a disordered configuration as the initial one, the system evolves towards the equilibrium crystalline phase, but, since crystallization is slow compared with the usual time of PIGS simulations, we see that the overpressurized liquid phase is metastable for a number of Monte Carlo steps sufficiently large to give good statistics for the ground state averages of the physical observables. If the density is increased even more ($p > 90$ bars), one starts to observe the formation of crystallites and the stabilization of the liquid becomes more difficult.

Another evidence of the metastability of the liquid configuration in our simula-

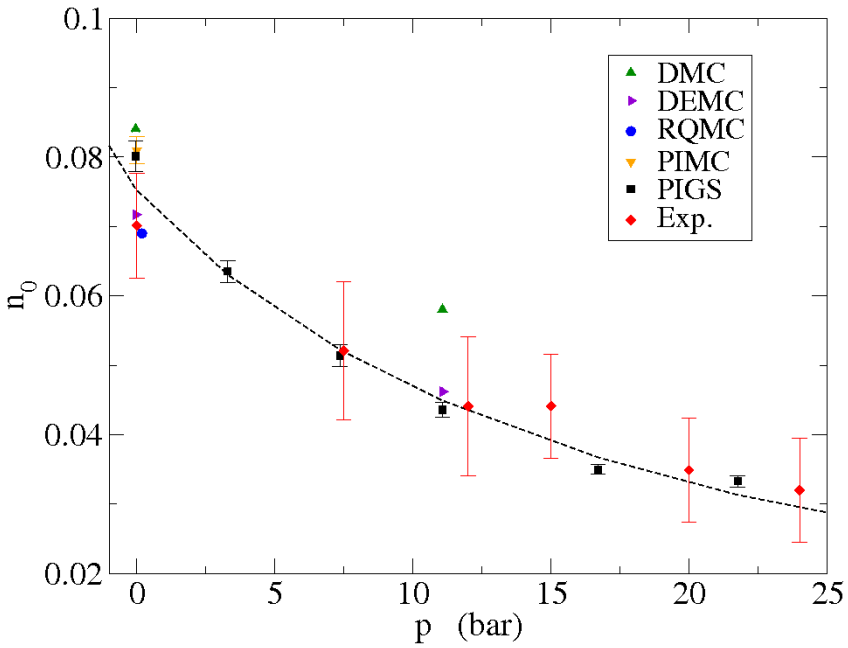

Figure 4.6: The condensate fraction n_0 in liquid ^{4}He at zero temperature as a function of pressure p in the region of stability of liquid phase. Our PIGS results (black squares) are compared with the experimental ones (red diamonds) [71] and previous theoretical calculations, obtained with Diffusion Monte Carlo (green up triangles) [4], Diffusion Euler Monte Carlo (violet left triangles) [5], Reptation Quantum Monte Carlo (blue circle) [6] and PIMC at $T = 1\,\mathrm{K}$ [7]. The dashed line represents the curve obtained fitting our results with the equation $n_0 = A + B/(p - p_0)$.

tions can be given computing the static structure factor $S(k)$. In all the calculations performed, we notice the absence of Bragg peaks in $S(k)$, which indicates clearly that the system does not present crystalline order.

Our results for n_0 at different p are contained in Table 4.1, together with our estimates for the kinetic energy K/N. It is interesting to notice that the condensate fraction of the overpressurized liquid is finite also for densities above the melting ($\rho \geq 0.02862$ Å^{-3}). This evidence supports our hypothesis that the system has reached a metastable non-crystalline phase, since recent PIGS simulations show that, in commensurate hcp ^{4}He crystals, the one-body density matrix decays exponentially to zero at large distances and therefore BEC is not present [65, 75]. In particular, we obtain that in the overpressurized fluid at the melting density the condensate fraction is $n_0 \simeq 1.2\%$. This result, even though cannot provide any deeper understanding concerning the quest of supersolidity in ^{4}He [65], can be thought as an upper limit for the condensate fraction in solid ^{4}He at melting. It is also interesting to notice that, even at the freezing pressure, the condensate fraction is already quite small, $n_0 = 2.9\%$.

In Fig. 4.6, we plot our results for n_0 as a function of p on the range of pressures

where the liquid phase is stable. Our results follow well an inverse proportionality law $n_0(p) = A + B/(p - p_0)$, with p and p_0 measured in bar: the best fit we got has parameters $A = -0.0068 \pm 0.0012$, $B = 1.56 \pm 0.10$, $p_0 = -19.0 \pm 0.9$ bar. In Fig. 4.6, we also compare our estimates for n_0 with the experimental ones [71] and with the ones obtained in previous numerical simulations [4, 5, 6, 7]. It is easy to notice that our results provide an excellent description of the experimental dependence of the condensate fraction as a function of pressure in all the range of stability of the liquid phase of ^{4}He, improving previous calculations which focus especially on the equilibrium density and do not explore in detail the physically interesting pressure range where the experimental data can be measured. Notice that the experimental value of n_0 at zero pressure reported in the more recent experiment [71] is slightly smaller ($7.01 \pm 0.75\%$), but still statistically compatible within the error bars, than the previous one by the same team [70].

Chapter 5

The supersolid phase of ^{4}He

This chapter is devoted to the study of solid ^{4}He and to its eventual supersolid phase. The supersolid state of matter, that is a phase where crystalline order coexists with superfluidity, was predicted many decades ago, but only in the last years it has been possible to find experimental evidences suggesting the existence of this phase in solid ^{4}He. In this work, we perform PIMC simulations of condensed ^{4}He at densities at which the solid phase is stable in real samples, according to different microscopic configurations of the atoms: perfect hcp crystal, crystals with vacancies, amorphous solid and perfect bcc crystal. The main objective is to investigate which of these models provides results in better agreement with experimental ones. We notice a phase transition to a superfluid phase only if the crystal is not commensurate and that the estimated onset temperature of BEC is comparable, in crystal with a low vacancy concentration, with the temperature at which supersolidity effects appears in the experiments.

5.1 Introduction

The debate about the supersolid state of matter has gained a great interest among the scientific community after the first observation, made by Kim and Chan in 2004, of non classical rotational inertia (NCRI) in torsional oscillators containing solid helium [14, 15]. Measuring the resonant period of the oscillator, Kim and Chan showed an anomalous drop of the rotational inertia of the sample when the temperature is lowered below a certain critical value and explained this behavior as the appearance of a superfluidity effect in the solid sample. Although several experiments have confirmed the appearance of a phase transition in solid ^{4}He at temperatures $T_c \sim 60 - 100\,\mathrm{mK}$ [76, 77], we are still far from a complete description of this phenomenon, because of controversial experimental results. For instance, the values of the superfluid density ρ_s/ρ reported so far can vary more than one order of magnitude, according to experimental conditions such as the way in which the crystal is prepared, its subsequent annealing or the ^{3}He concentration [78, 79, 80]. These discrepancies suggest that the quality of the solid sample plays a very important role in these experiments and make fundamental a study of crystalline defects in quantum crystals.

The first theoretical speculations about the supersolid phase date back almost forty years. Penrose and Onsager, in 1956 stated that BEC cannot appear in crystals where the atoms are strongly localized around lattice positions [11]. However, this statement was never considered as a definitive answer to the question of supersolid-

ity, since the model discussed does not take into account the delocalization of the atoms which may in principle be large in quantum crystals. Andreev and Lifshitz, some years later, suggested that a possible supersolid behavior can be explained assuming the presence, in the ground state of quantum crystals, of delocalized vacancies which may undergo Bose-Einstein condensation (BEC) at low temperature [12]. Another relevant speculation was made by Chester in 1970. He conjectured that, since the crystalline phase comes from a spontaneous breaking of the translational symmetry, it is possible to describe the solid phase with the same wave function used to describe the liquid, which is known to support BEC [13].

Nevertheless, all these early works were based on simplified models, so that it was not possible to draw specific predictions for solid ^{4}He. More recently, microscopic methods have been extensively used to provide a reliable description of the supersolid state, but, so far, they have not been able to reproduce all the experimental findings. Path integral Monte Carlo (PIMC) simulations have shown that a commensurate perfect crystal does not exhibit superfluidity [81, 66, 65], but a non-zero condensate fraction has been observed in crystals presenting defects, such as vacancies [82] or grain boundaries [83], and in simulations of an amorphous state of the solid [84]. Nevertheless, these simulations are not able to provide results in complete agreement with the experimental ones and therefore does not bring to a definitive answer of the supersolidity problem.

The possibility for solid ^{4}He to present vacancies in its ground state seems to be hindered by the energetic cost of these defects. According to several Quantum Monte Carlo results, the vacancy formation energy is estimated to be of the order of 10 K [85, 86, 87, 88, 89], in agreement with experimental measurements [90]. Nevertheless, the high delocalization of the vacancies in solid ^{4}He at temperatures close to zero prevents an interpretation of these defects in terms of a classical theory involving an activation energy and a configurational entropy for their creation [91, 92, 93]. Furthermore, experimental data cannot rule out the possibility of a zero-point vacancy concentration below 0.4% [94].

It has also to be noticed that formation energy considerations do not exclude the possibility of vacancies introduced through the experimental conditions, for example during the crystal growth. The spatial correlation between vacancies has been calculated in order to understand if a gas of defects can be metastable in solid ^{4}He. The results show an attractive correlation between vacancies at short distance, but they cannot conclude if they form bound states and aggregate in large clusters, which eventually would phase separate [86, 95, 96, 97].

The observation by Beamish and collaborators [98] of an increase of the shear modulus of hcp ^{4}He at nearly the same onset temperature for NCRI has lead to think that, at least in a partial way, the NCRI signal can be attributed to the change in the elastic properties. This evidence has led Beamish *et al.* to suppose that the anomalous behaviors, both the one in the rotational inertia and the on in the elastic properties, are due to a dislocation network which below T_c becomes pinned by ^{3}He impurities and thus immobile. This hypothesis, however, cannot explain the reason why the mass decoupling seen in torsional oscillator experiment is

independent of the geometry of the confinement. Indeed, an interconnected network of dislocations is not likely to appear in porous media like vycor, where, on the contrary, the period drop of the torsional oscillator is as evident as in the bulk systems. Furthermore, recent experiments have shown that the period of torsional oscillator is not susceptible to the elastic module change, supporting the theory that not all the NCRI effects in solid ^{4}He can be interpreted uniquely on plasticity terms [99, 100].

On the other hand, there are still some evidences indicating that the excitations controlling the torsional oscillator motions are generated by thermal and mechanical stimulation, showing thus an interplay not only between the rotational and shear dynamics of solid ^{4}He, but also a connection with the relaxational dynamics of the sample [101]. Relying on these results, Balatsky and collaborators claim that NCRI effects are to be attributed to the presence of non-equilibrium states inside of the solid sample at very low temperature. In a previous work, the same group have shown that the dynamics of the sample is much slower at temperatures below the temperature T_c at which appears the period drop in torsional oscillator experiments [102]. According to them, T_c does not have to be interpreted as the temperature of transition to a superfluid state, but as the temperature at which amorphous states become metastable in the solid. Glassy configurations for ^{4}He has been studied theoretically with PIMC method by Boninsegni *et al.* [84]: they show that these amorphous states support BEC at low temperature but they do not provide any information about the temperature dependence neither of the condensate fraction nor of the superfluid one.

Although the main focus of the recent research activity has been hcp ^{4}He, which is the stable phase at very low temperatures, Eyal *et al.* [103] have reported recently torsional oscillator experiments on bcc ^{4}He at temperatures between 1.3 and 1.9 K that show similar phenomena to those measured in the hcp phase below 100 mK. This is a surprising result since, even if the disorder of the sample is eventually large, the temperatures of this experiment are one order of magnitude larger than in hcp. This is not the only relevant result related to the bcc phase that emerged in the last years. Some time ago, Markovich *et al.* [104] reported neutron-scattering measurements of phonons in bcc ^{4}He and found an unexpected “opticlike" mode along the [110] direction. This new mode has been theoretically interpreted by Gov [105] in terms of correlated dipolar interactions.

The boundaries of the bcc phase of ^{4}He were first determined by Vignos and Fairbank [106] in 1961 after analyzing their measurements of the velocity of longitudinal sound. The existence of this phase was confirmed after x-ray scattering by Schuch and Mills [107]. Later on, Grilly and Mills [108] measured the volume change along the hcp-bcc coexistence line and Edwards and Pandorf [109] performed accurate measurements of the heat capacity. Updated accounts of the thermodynamic properties of bcc ^{4}He can be found in Refs. [110, 111]. In Fig. 5.1, the P-T phase diagram in the region of interest is plotted. As one can see, the stability of the bcc solid is only ~ 0.04 K wide at fixed pressure and it represents an intermediate phase between the hcp solid and the superfluid in the range of temperatures $T \simeq 1.5$-1.75

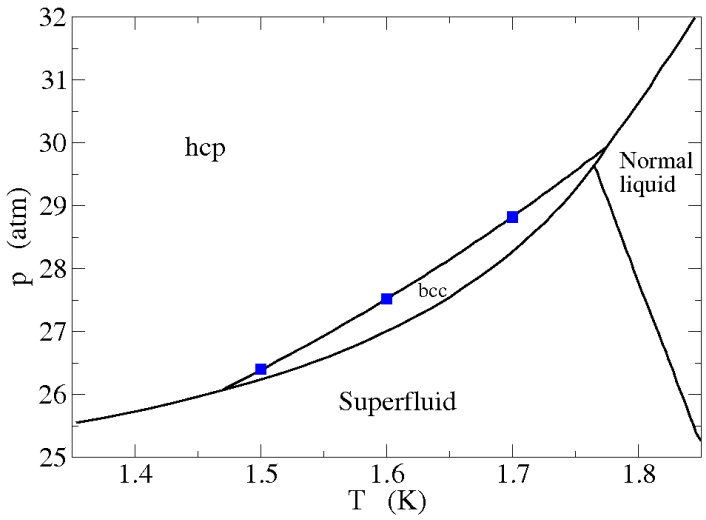

Figure 5.1: Pressure-temperature phase diagram in the stable region of the bcc phase of solid ^{4}He. The squares correspond to the thermodynamic points studied in the present work.

K.

From the theoretical point of view, even if quantum Monte Carlo (QMC) methods have been widely applied in the past to the study of solid ^{4}He, most of the work is devoted to the hcp phase and the results on the bcc phase are scarce and concentrated to the limit of zero temperature. [85, 112, 113]. To our knowledge, the only existing work in the bcc stable P-T region shown in Fig. 5.1 was done by Ceperley [114] with the main goal of estimating the momentum distribution and kinetic energies after some neutron scattering experiments [115].

In this chapter we want to provide a deeper insight in the study of solid ^{4}He, both in the hcp and bcc phases, and of its eventual supersolidity, performing PIMC calculations of condensed ^{4}He at densities for which the solid phase is stable in real samples. We study different models for the solid, making use of different microscopic configurations, and we provide results for their main physical properties, focusing especially in the temperature dependence of the one-body density matrix $\rho_1(r)$. We compare the obtained results with the experimental data, in order to understand if any of models proposed is suitable to describe the anomalies shown by real samples in the experiments. In Sec. 5.2, we provide results for a perfect hcp ^{4}He crystal, comparing the results for the momentum distribution $n(k)$ with the data obtained experimentally with deep inelastic neutron scattering. In Sec. 5.3, we study the model of a crystal presenting vacancies, showing qualitatively the delocalization of the point defects when the temperature decreases and studying the dependence of the onset temperature of BEC with the vacancy concentration X_v. In Sec. 5.4, we present preliminary results obtained in the study of amorphous configurations at high densities, showing the appearance of BEC at temperature higher than the one

at which NCRI effects appears in the experiments. In Sec. 5.5, we present a PIMC study of the bcc phase at three temperatures and densities corresponding to the experimental points shown in Fig. 5.1 and compare them with the corresponding hcp ones along the coexistence line.

5.2 Perfect hcp crystal

We have carried out PIMC simulations of hcp ^{4}He using a perfect lattice in a simulation box containing $N = 180$ atoms interacting with an Aziz pair potential [49]. At first, we perform calculations for a solid at a density $\rho = 0.0294\,\text{Å}^{-3}$, at three different temperatures. The results for $\rho_1(r)$ and $n(k)$ are shown in Figure 5.2. We can see that, at large r, $\rho_1(r)$ decays exponentially, indicating that this system does not present ODLRO. We can also see that there is not a dependence of the momentum distribution with the temperature, in agreement with previous results by Clark and Ceperley [66].

In order to compare our results to the ones obtained by neutron scattering experiments, we compute the Compton profile of the longitudinal momentum distribution $J(y)$, which is $n(\mathbf{k})$ projected along the direction of the momentum $\mathbf{Q}$ of the incoming neutron and it is of easier experimental access than $n(\mathbf{k})$. In the Impulse Approximation, which describes well the inelastic neutron scattering at high momentum transfer, $J(y)$ and $n(k)$ are related by the formula [3]

$$J(y) = \int d\mathbf{k}\, n(\mathbf{k})\, \delta(y - k_Q) = 2\pi \int_{|y|}^{\infty} dk\, k\, n(k)\ , \tag{5.1}$$

with $k_Q = \mathbf{k} \cdot \frac{\mathbf{Q}}{|Q|}$.

In Figure 5.3, we compare the results for the longitudinal momentum distribution obtained from our $n(k)$ at zero temperature with the fit obtained from experimental measurement by Diallo *et al.* for the same quantity in solid ^{4}He at molar volume $V_m = 20.01\,\text{cm}^3/\text{mol}$ ($\rho = 0.0301\,\text{Å}^{-3}$) and a temperature $T = 80\,\text{nK}$ [116]. We can see that our result are in a good agreement with the experimental ones.

In Figure 5.3, we have also plotted the $J(y)$ obtained by Ceperley in a PIMC simulation for a bcc crystal at a density close to the melting $\rho = 0.0288\,\text{Å}^{-3}$ and at a temperature $T = 1.67\,\text{K}$ [114]. The difference between our momentum distribution and the one computed by Ceperley has to be attributed to the larger density of the crystal we are simulating, and indicates that a larger coordination between the atoms in the solid cause a depletion of the low momentum states.

This behavior is confirmed when simulating a crystal at higher densities. Figure 5.4 shows $\rho_1(r)$ and $n(k)$ in a crystal at the density $\rho = 0.0335\,\text{Å}^{-3}$. For this density, the solid phase is stable over a larger range of temperature, making us able to simulate the system at temperatures up to $T = 3\,\text{K}$. Comparing the results for the two different densities, we see that, when ρ increases, the one-body density matrix decays faster to zero and that the occupation of the low momentum states is appreciably decreased. It is also interesting to notice that $\rho_1(r)$ and $n(k)$ are

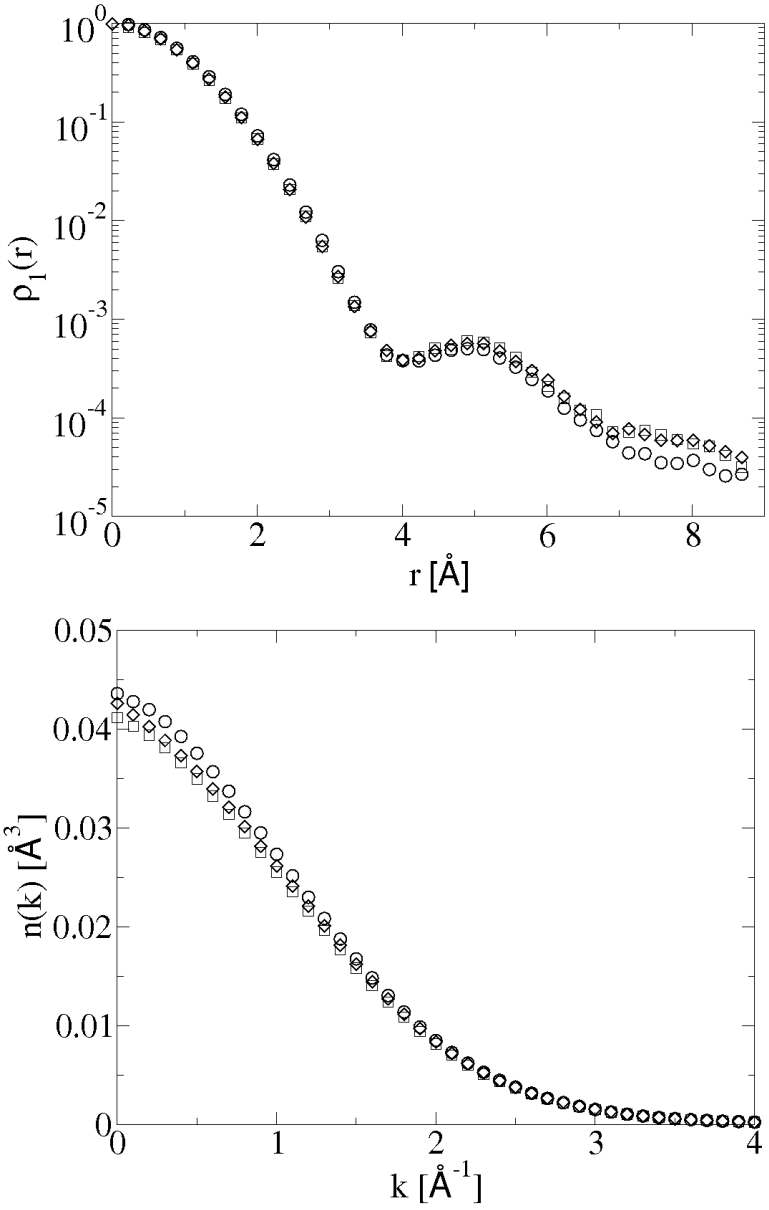

Figure 5.2: The one-body density matrix $\rho_1(r)$ (up) and the momentum distribution $n(k)$ (down) for a commensurate hcp crystal at density $\rho = 0.0294\,\text{Å}^{-3}$ and at different temperatures: $T = 0\,\text{K}$ (circles), $T = 1\,\text{K}$ (squares) and $T = 2\,\text{K}$ (diamonds). Statistical errors are below symbol size.

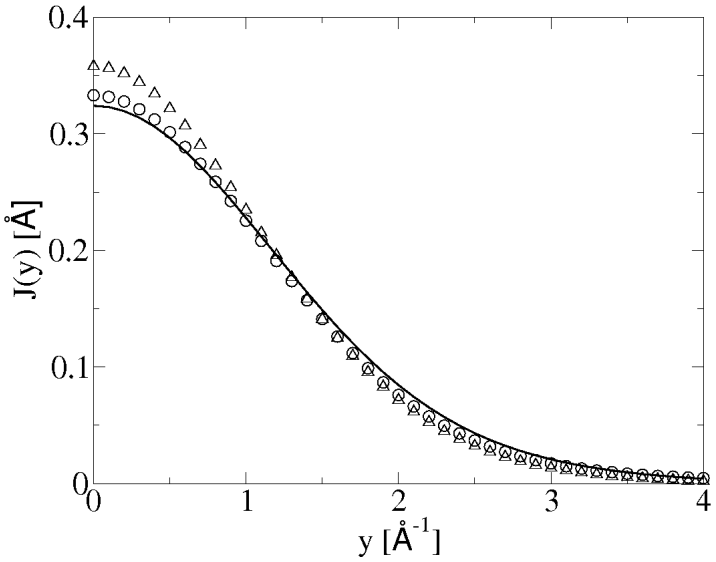

Figure 5.3: The longitudinal momentum distribution $J(y)$: our results at $T = 0\,\mathrm{K}$ and $\rho = 0.0294\,\mathrm{\AA}^{-3}$ (circles) are compared with the fit obtained by Diallo *et al.* [116] from neutron scattering experiment at $T = 80\,\mathrm{nK}$ and $\rho = 0.0301\,\mathrm{\AA}^{-3}$ (solid line) and with the PIMC results of Ceperley [114] for a bcc solid at $T = 1.67\,\mathrm{K}$ and $\rho = 0.0288\,\mathrm{\AA}^{-3}$ (triangles).

nearly independent of T even for temperatures larger than T_λ, that is the superfluid transition temperature in the liquid phase.

It is important to notice that at both densities, the shape of $n(k)$ differs significantly from the classical Gaussian Maxwell-Boltzmann distribution. This feature is clearly shown in Figure 5.5, where we plot, on a logarithmic scale, $n(k)$ as a function of k^2. From this graph, it is easy to see the differences between the momentum distributions we obtained from PIMC and the straight line which represent a Gaussian distribution. We also notice that these differences are smaller in the system at $\rho = 0.0335\mathrm{\AA}^{-3}$, indicating that solid helium becomes more classic when the density increases.

In Fig. 5.6, we plot a two-dimensional projection of the quantum particles (represented by the polymers in PIMC) lying in a basal plane of the hcp lattice at two different temperatures, in order to give a more qualitative description of the results obtained in this study of the perfect hcp ^{4}He crystal. Looking at the two pictures, we can understand that the atoms are delocalized, because of their zero-point motion, on distances comparable with the lattice constant and that this delocalization is larger at low temperature. However, even at low temperature the superpositions and the exchanges between different polymers, i.e. between different quantum atoms, are rare events. This statement can be supported by the fact that the acceptance rate of the Swap update, that is the update performing the

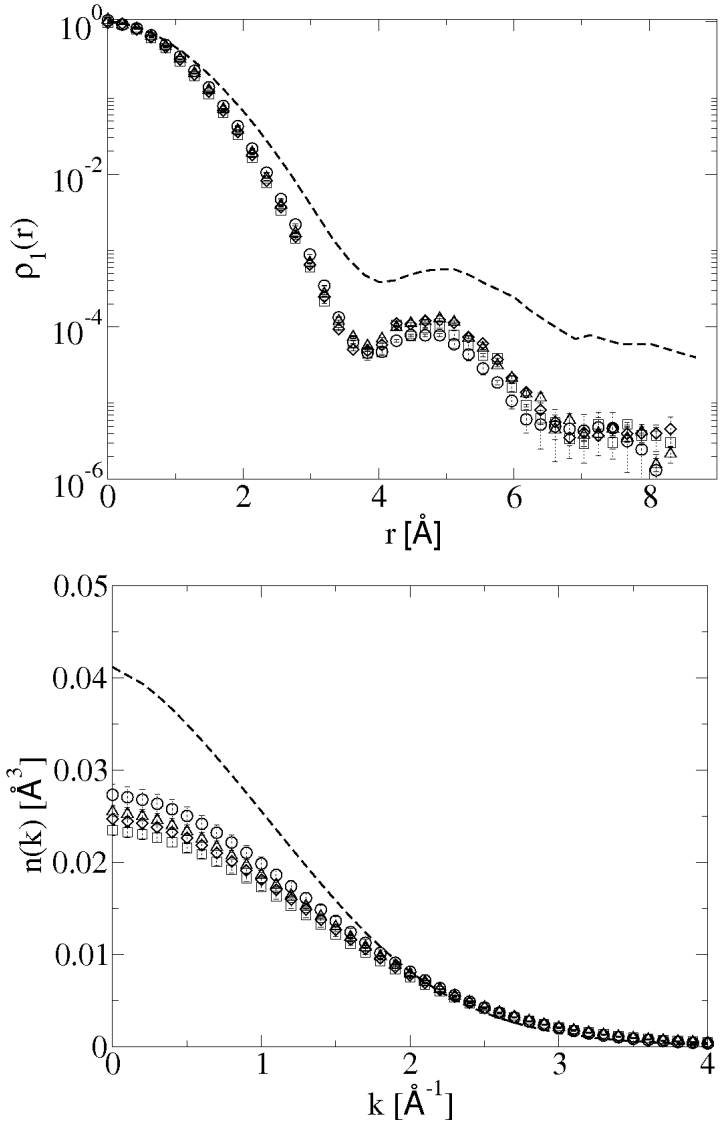

Figure 5.4: The one-body density matrix $\rho_1(r)$ (up) and the momentum distribution $n(k)$ (down) for a commensurate hcp crystal at density $\rho = 0.0335\,\text{Å}^{-3}$ and at different temperatures: $T = 0\,\text{K}$ (circles), $T = 1\,\text{K}$ (squares), $T = 2\,\text{K}$ (diamonds) and $T = 3\,\text{K}$ (triangles). The dashed lines represent the same quantities computed for hcp crystal at $T = 1\,\text{K}$ and $\rho = 0.0294\,\text{Å}^{-3}$

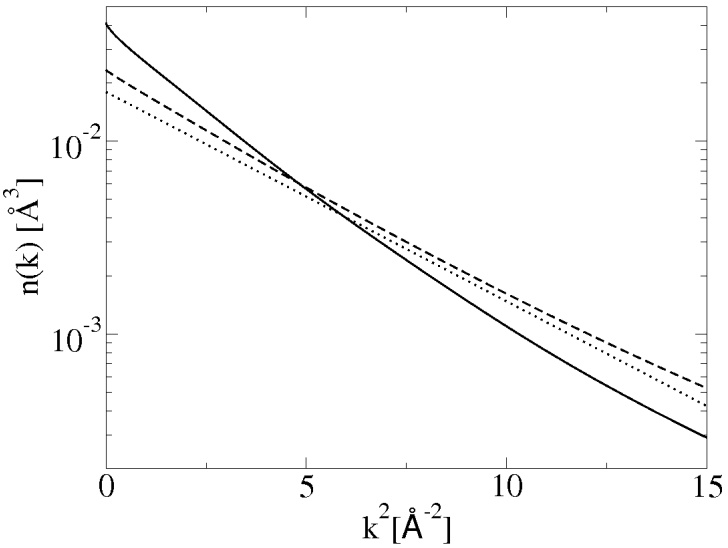

Figure 5.5: The momentum distribution $n(k)$ as a function of k^2 at $T = 1\,\mathrm{K}$ and densities $\rho = 0.0294\,\mathrm{\AA}^{-3}$ (solid line) and $\rho = 0.0335\,\mathrm{\AA}^{-3}$ (dashed line). The dotted line represent a Gaussian $n(k)$ and it is used to guide the eye.

bosonic permutations, is rather low (less than 1% at every temperature). This means that the probability for atoms to permutate is not zero, allowing the appearance of anharmonicity effects in the crystal, but it is not high enough to permit the creation of long permutation cycles which are necessary to the emergence of macroscopic effects such as BEC or superfluidity.

5.3 Crystal with vacancies

In order to calculate $\rho_1(r)$ in a crystal with vacancy concentration $X_v = 1/180$, we have carried out simulations of $N = 179$ ^{4}He atoms, interacting through an accurate Aziz pair potential [49], in an almost cubic simulation box matching the periodicity of an hcp lattice made up of $N_s = 180$ sites at a density $\rho = 0.0294$ Å^{-3}. We apply periodic boundary conditions to the simulation box in order to simulate the infinite dimensions of the bulk system. In Fig. 5.7, we show the results for $\rho_1(r)$ at different temperatures and we compare them with the zero temperature estimations of ρ_1 for the same system and for a perfect hcp crystal, obtained with the Path Integral Ground State method. We notice that, at temperatures $T \geq 0.75$ K, $\rho_1(r)$ computed in an incommensurate crystal, even though is not compatible with ρ_1 for the perfect crystal, presents a similar exponential decay at large r. At lower temperatures, the decay of $\rho_1(r)$ is smoother and, for temperatures $T \leq T_0 = 0.2$ K, ρ_1 presents a non-zero asymptote at large r, which indicates the presence of BEC in the system. This T_0 can be considered a first estimate of the onset temperature of supersolidity

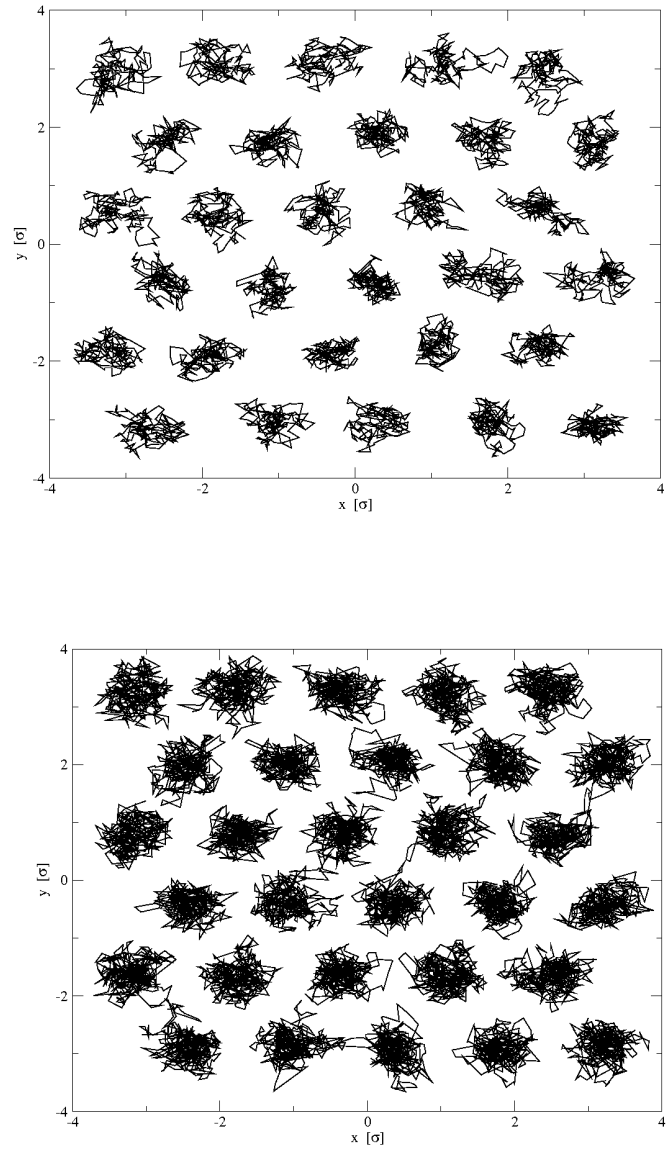

Figure 5.6: Two dimensional projection of basal planes of a perfect hcp crystal at $T = 1\,\mathrm{K}$ (up) and at $T = 0.25\,\mathrm{K}$ (down), represented according the PIMC isomorphism of classical polymers. The coordinates of the polymers are expressed in σ units, with $1\,\sigma = 2.556\,\mathrm{\AA}$.

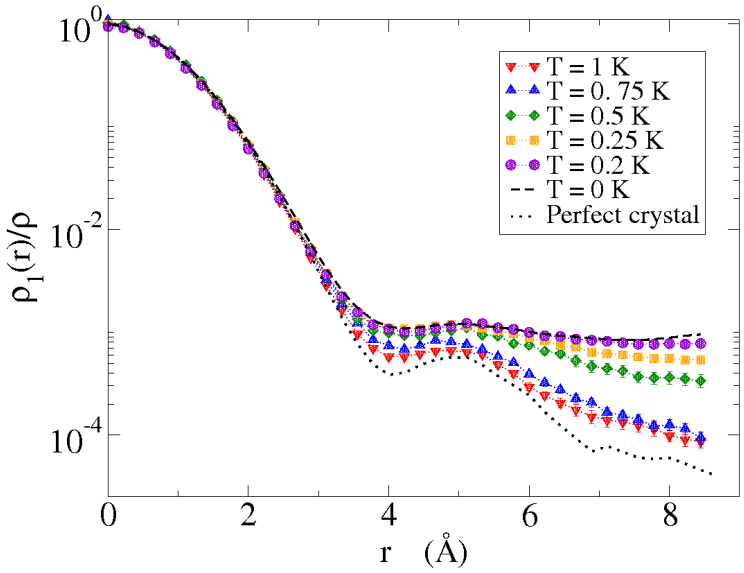

Figure 5.7: The one-body density matrix $\rho_1(r)$ for an hcp crystal with vacancy concentration $X_v = 1/180$ at density $\rho = 0.0294$ Å^{-3} at different temperatures: $T = 1$ K (red triangles down), $T = 0.75$ K (blue triangles up), $T = 0.5$ K (green diamonds), $T = 0.25$ K (yellow squares) and $T = 0.2$ K (purple circles). The dotted and dashed lines represent $\rho_1(r)$ at zero temperature respectively for the commensurate ($X_v = 0$) and incommensurate crystal ($X_v = 1/180$) at the same density.

in the simulated system. An analysis of the finite size effects would be needed to get a more precise estimation of the critical temperature of the supersolidity transition. Nevertheless, the simulation of bigger systems with exactly the same vacancy concentration requires a huge computational effort that would make the calculations impracticable.

In order to give a more qualitative description of the appearance of BEC in incommensurate ^{4}He solids, we visualize typical configurations of the system during the simulation. In Fig. 5.8, we plot two-dimensional projections of the positions of the quantum particles (represented by polymers in PIMC) lying in a basal plane of the incommensurate hcp crystal at different temperature. At $T = 1$ K, ^{4}He atoms tend to stay localized around their equilibrium positions. Also the vacancies are localized and can be easily detected inside the lattice. This explains the fact that, at that temperature, the presence of vacancies does not affect noticeably the overall behavior of ρ_1 which, for the incommensurate crystal, is similar to the one of the perfect crystal. Also the acceptance rate of the Swap update (slightly lower than 1%) is very close to the value obtained in the simulation of the perfect crystal. At $T = 0.5$ K, the effects of the delocalization of the ^{4}He atoms can be seen with the appearance of some polymers which are spread on two different lattice points. In the space configurations at this temperature, the acceptance rate of the exchange between the polymers is higher than in the configurations at larger temperature

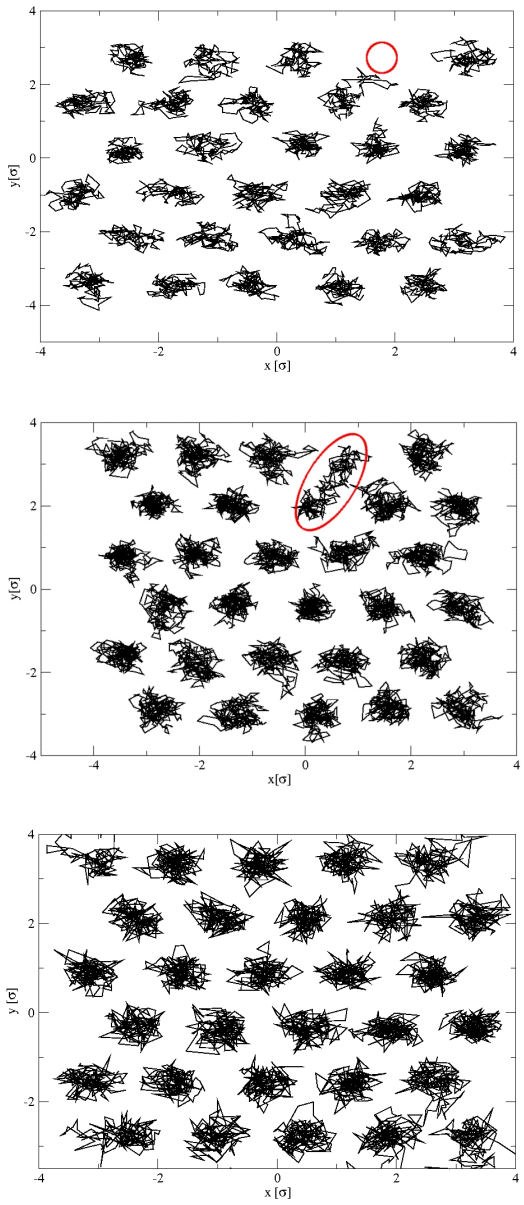

Figure 5.8: Two-dimensional projection of a typical basal plane of the incommensurate hcp crystal at different temperatures, represented according to the PIMC isomorphism of the classical polymers. At $T = 1$ K (higher panel), the vacancy is localized and indicated by the red circle. At $T = 0.5$ K (middle panel), the vacancy begins to delocalize: the red ellipse indicate a quantum particle delocalized over two different lattice sites. At $T = 0.2$ K (lower panel), the vacancy is completely delocalized and cannot be easily detected. The coordinates of the polymers are expressed in σ units, with $1\,\sigma = 2.556\,\text{Å}$

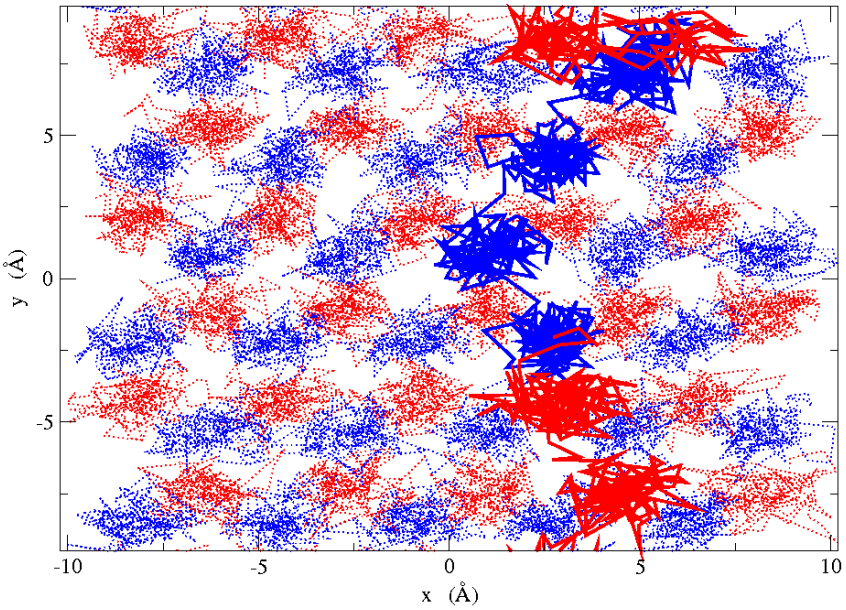

Figure 5.9: Two-dimensional projection of two consecutive basal planes of the incommensurate hcp crystal at $T = 0.15$ K. The different colors distinguish the two different planes. The thick solid line represent a long permutation cycle between the ^{4}He atoms presenting a non-zero winding number.

(the acceptance rate of the Swap update has an average value of about 1.5 %), but it is still too low to allow the appearance of long permutation cycles, which are necessary to see BEC. At $T = 0.2$ K, the large zero-point motion of the ^{4}He atoms makes the vacancy delocalized and undetectable inside the crystal, which looks like a commensurate system. Since the number of lattice sites is different from the number of particles, this means that different polymers may superpose over the same lattice site: this occurrence strongly enhances the possibility for the atoms to permutate (we see, in most of the simulations, an acceptance rate for the Swap update higher than 2.5%) and allows the creation of long permutation cycles which close on periodic boundary conditions. The appearance of configurations presenting a non zero winding number, as the one shown in Fig. 5.9, indicates that the simulated crystals below $T_0 = 0.2$ K support superfluidity. However, it is not possible to give a reliable estimation for the superfluid density ρ_s/ρ in these systems, since the smallest value for ρ_s/ρ computable with the winding number estimator is of the order of 1%, that is of the same order of the value expected from the experimental measurements.

In order to study how the vacancy concentration in quantum solids affect the onset temperature of BEC, we have computed the one-body density matrix also for fcc ^{4}He crystals with $X_v = 1/108$ and $X_v = 1/256$: the results are shown, respectively in Fig. 5.10 and in Fig. 5.11. In Table 5.1, we show the onset temperature

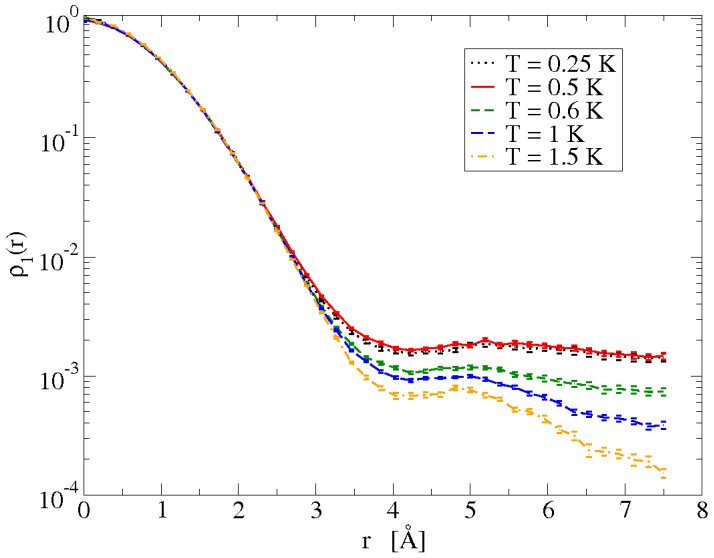

Figure 5.10: The one-body density matrix $\rho_1(r)$ for a fcc crystal with vacancy concentration $X_v = 1/108$ at density $\rho = 0.0294$ Å^{-3} at different temperatures: $T = 1.5$ K (yellow dot-dashed line), $T = 1$ K (blue long dashed line), $T = 0.6$ K (green dashed line), $T = 0.5$ K (red solid line) and $T = 0.25$ K (black dotted line).

X_v	T_0 (K)	n_0
1/108	0.5 ± 0.1	$(1.81 \pm 0.14)10^{-3}$
1/180	0.20 ± 0.05	$(9.0 \pm 0.8)10^{-4}$
1/256	0.15 ± 0.05	$(7.2 \pm 0.8)10^{-4}$

Table 5.1: The onset temperature of BEC T_0 and the condensate fraction n_0 at low temperature as a function of the vacancy concentration X_v

of BEC T_0 and the condensate fraction n_0 at low temperature obtained with PIMC in the three crystals we have studied. We notice that, for the lowest X_v, we get $T_0 = 0.15 \pm 0.05$ K, which is close to the temperatures at which supersolidity has been experimentally observed.

In Fig. 5.12, we plot our results for T_0 as a function of X_v. Our results for T_0 do not follow the law $T_0 \sim X_v^{2/3}$, obtained from a description of solid ^{4}He in terms of a rarefied Gross-Pitaevskii superfluid gas of vacancies, as proposed by Anderson in Ref. [93]. This seems to suggest that, at least in the range of X_v we have been able to study, the correlations between vacancies have an important effect on T_0 and the system cannot be described within a mean-field approach. Nonetheless, our qualitative description of ^{4}He crystals supports the hypothesis [93] according to which it is not reasonable to regard vacancies in quantum solids as strictly local entities.

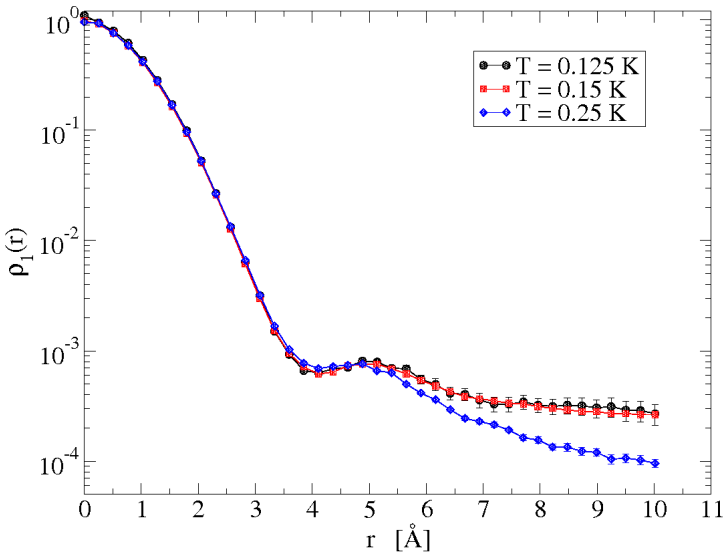

Figure 5.11: The one-body density matrix $\rho_1(r)$ for a fcc crystal with vacancy concentration $X_v = 1/256$ at density $\rho = 0.0294$ Å^{-3} at different temperatures: $T = 0.25$ K (blue diamonds), $T = 0.15$ K (red squares), $T = 0.125$ K (black circles). Error bars, if not showed, are below symbol size.

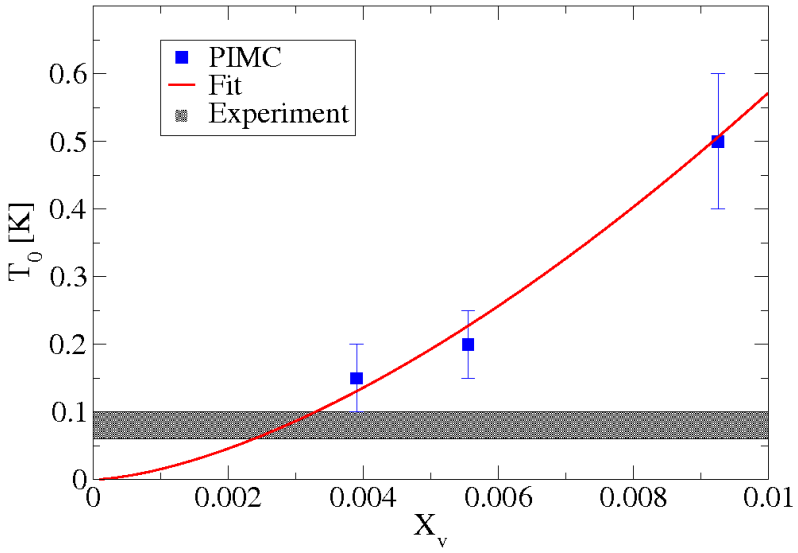

Figure 5.12: The onset temperature T_0 of BEC in incommensurate solid ^{4}He as a function of the vacancy concentration X_v: the blue squares represent the results obtained with the PIMC method; the red line is a fit to the data with a power law $T_0 = AX_v^B$; the grey band indicates the temperature at which the NCRI appears experimentally.

In an attempt to estimate which should be the vacancy concentration in ^{4}He crystals needed to have BEC appearing at the temperature T_c measured experimentally for the supersolid transition, we have plotted in Fig. 5.12 a power function trying to fit the PIMC results. According to this empirical law, ^{4}He crystals with a vacancy concentration $X_v \sim 2 - 3 \times 10^{-3}$ would have an onset temperature T_0 in agreement with the experimental values T_c. This result for X_v is in good agreement with the equilibrium vacancy concentration in solid ^{4}He at zero temperature obtained variationally with the shadow wave function [96].

5.4 Amorphous solid

To simulate amorphous solid ^{4}He, we have carried out simulations of disordered configurations at densities higher than the melting one $\rho_m = 0.02862\,\text{Å}^{-3}$. Such a simulation requires a particular equilibration of the system. At first, having fixed the number of particles N and the temperature T of the microscopic system that we want to study, we perform a simulation of N ^{4}He atoms at the temperature T and at the equilibrium density of the liquid phase $\rho_{eq} = 0.02186\,\text{Å}^{-3}$. When this system at the density ρ_{eq} has equilibrated, we rescale the dimensions of the simulation box and all the coordinates of the final configuration, in order to recover a configuration at the correct density ρ: this rescaled configuration, which has the features of the overpressurized liquid, can be used as a starting point of the simulation of the amorphous solid.

At this point, we can start the simulation of the disordered phase at density $\rho > \rho_m$. If we study the trend of the properties of the microscopic system as the simulation goes on, we see that this configuration remains stable for several Monte Carlo steps, but at a certain point, the system finds out a configuration which is more energetically favorable than the initial one. This event is particularly clear if we focus on the trend of the potential energy per particle V/N. In Fig. 5.13, we show how V/N changes as a function of the number of Monte Carlo steps in a simulation of $N = 140$ ^{4}He atoms at the density $\rho = 0.0294\,\text{Å}^{-3}$ and at the temperature $T = 0.8\,\text{K}$. We can see that in the first part of the simulation the value of the potential energy per particle oscillates around a certain value close to -29 K, but this trend changes clearly after about 16000 Monte Carlo steps. In the second part of the simulation, the mean value of the V/N is approximately 1 K smaller than the mean value in the first part of the simulation: this drop indicates that, as the simulation goes on, the system is driven to a configuration which has a lower energy than the overpressurized liquid and which, therefore, is more stable.

To better understand the microscopic features of this metastable phase, we calculate the static structure factor $S(q)$ in the second part of the simulation and we compare it with $S(q)$ obtained in the first part: the results are shown in Fig. 5.14. We can notice that, in the first part of the simulation, $S(q)$ is very similar to the one of a liquid, presenting only a broad peak at $q \simeq 2\,\text{Å}^{-1}$. In the second part of the simulation, we notice the appearance in $S(q)$ of two sharper peaks at the same q in

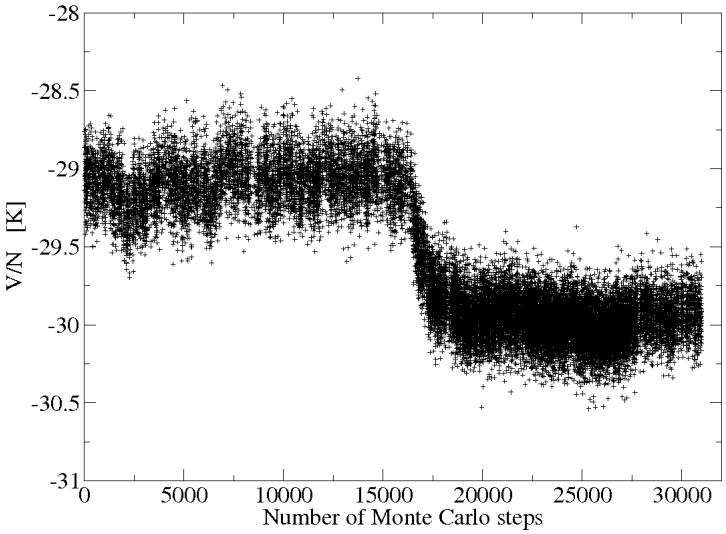

Figure 5.13: Mean values of the potential energy per particle V/N computed for consecutive steps during a typical PIMC simulation of an amorphous solid made up of $N = 140$ ^{4}He at temperature $T = 0.8$ K.

which the liquid structure factor presents the maxima. This indicates the formation, inside the microscopic system, of crystallites with different orientation. However, we have no evidence of high peaks at large q and therefore the system lacks of the long range coordination typical of crystalline solids. We can conclude that we obtained in our simulation a metastable glassy configuration.

In order to investigate the BEC properties of amorphous ^{4}He solid, we have computed the one-body density matrix $\rho_1(r)$ for the configuration obtained equilibrating the microscopic system as described above at the density $\rho = 0.0294\,\text{Å}^{-3}$ for several temperatures. The results of this calculation are showed in Fig. 5.15. We can see the system presents a finite condensate fraction at the temperature $T = 0.8\,\text{K}$: our estimation of n_0 for the glass at this temperature is $n_0 = (1.4 \pm 0.3) \times 10^{-3}$, that is of the same order of magnitude of the condensate fraction obtained in crystal with a non-zero vacancy concentration at zero temperature (see section 5.3). However, we can notice that in amorphous solid at $T = 0.8\,\text{K}$, the appearance of configurations with a non zero winding number is more frequent than in the simulation of crystal presenting vacancies and we can give more easily an estimation of the superfluid fraction: from our PIMC simulation, we get at $T = 0.8\,\text{K}$, $\rho_s = 0.044 \pm 0.012$.

Our results for the glassy phase cannot be easily compared with experimental results, since it has been shown that amorphous states are particularly unstable in real samples at temperatures higher than 100 mK [102]. However, to have a better insight about the features of the glassy phase, it would be interesting to estimate the superfluid fraction of amorphous solid ^{4}He at temperatures lower than

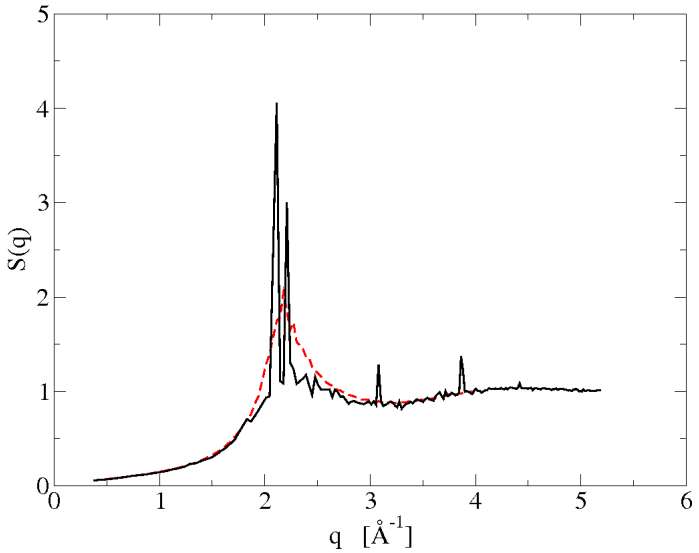

Figure 5.14: The static structure factor $S(q)$ computed in the PIMC equilibration of an amorphous solid made up of $N = 140$ ^{4}He atoms at temperature $T = 0.8$ K. The red dashed line corresponds to the calculation of $S(q)$ in the first part of the equilibration, in which the system presents the configuration of an overpressurized liquid. The black solid line corresponds to the calculation of $S(q)$ in the second part of the equilibration, in which the system presents the configuration of an amorphous solid.

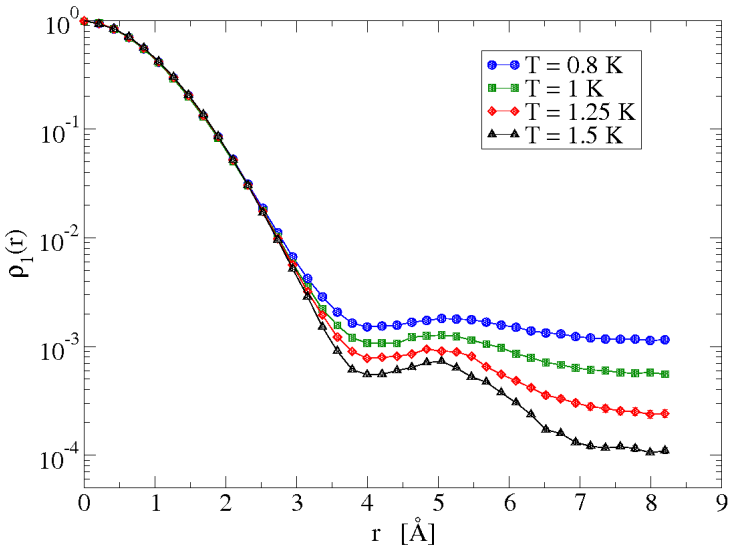

Figure 5.15: The one-body density matrix $\rho_1(r)$ for amorphous solid ^{4}He at density $\rho = 0.0294$ Å^{-3} at different temperatures: $T = 1.5\,\mathrm{K}$ (black triangles), $T = 1.25\,\mathrm{K}$ (red diamonds), $T = 1\,\mathrm{K}$ (green squares) and $T = 0.8\,\mathrm{K}$ (blue circles). Error bars are below symbol size.

the one we have managed to study here, in order to see if, as the temperature of the system decreases, ρ_s remains of the order of some percent, as measured in most of experiments, or if it increases, up to the point that the glass presents a larger superfluid fraction close to the absolute zero.

5.5 Crystal at the hcp-bcc coexistence line

To study the hcp-bcc coexistence line, we have carried out simulations in the three experimental thermodynamic points shown in Fig. 5.1. Explicitly, in the P-T phase diagram the coordinates of these points are A= $(1.5, 26.419)$, B= $(1.6, 27.572)$, and C= $(1.7, 29.029)$ in units of bar and Kelvin for the pressure and temperature, respectively. The corresponding densities are taken from the experimental data contained in Refs. [110, 111]: $(\rho_A^{\mathrm{hcp}} = 0.028834, \rho_A^{\mathrm{bcc}} = 0.028571)$, $(\rho_B^{\mathrm{hcp}} = 0.028954, \rho_B^{\mathrm{bcc}} = 0.028679)$, and $(\rho_C^{\mathrm{hcp}} = 0.029080, \rho_C^{\mathrm{bcc}} = 0.028805)$, all in units of Å^{-3}.

In the Hamiltonian of the system the potential part is built as a sum of pair-wise interatomic potentials, $\hat{V} = \sum_{i<j}^{N} V(r_{ij})$, with $V(r)$ of Aziz type [49]. Simulations are performed using periodic boundary conditions with a number of atoms per simulation cell of $N = 180$ (hcp) and $N = 128$ (bcc); tail corrections to the energy due to the use of a finite number of particles are estimated by running simulations with different N values and extrapolating its linear behavior in $1/N$ to the thermodynamic limit $1/N \to 0$ [117].

	A (T = 1.5 K)		B (T = 1.6 K)		C (T = 1.7 K)	
	bcc	hcp	bcc	hcp	bcc	hcp
$\frac{E}{N}$ expt.(K)	-5.95		-5.93		-5.91	
$\frac{E}{N}$ PIMC(K)	-6.166(7)	-6.058(7)	-6.137(8)	-6.025(7)	-6.091(9)	-5.984(6)
$\frac{V}{N}$ (K)	-30.103(3)	-30.448(3)	-30.230(3)	-30.605(3)	-30.372(3)	-30.752(2)
$\frac{K}{N}$ (K)	23.936(5)	24.391(7)	24.093(5)	24.580(5)	24.281(7)	24.768(5)

Table 5.2: PIMC results of the total (E/N) and partial energies (V/N, K/N) for the three thermodynamic points in the hcp-bcc coexistence line here analyzed. Experimental values of the bcc energies, reported in the first row, are taken from Ref. [110]. Figures in parenthesis stand for the statistical errors.

PIMC results for the total energy per particle in the three mentioned thermodynamic points are reported in Table 5.2. The difference between the energies of the two lattices in the coexistence line is small but, in the three cases, the bcc energies are larger than the hcp ones (in absolute values). This difference is mainly due to the slightly smaller density in the bcc side with respect to the hcp one, with a smaller effect of the lattice type (at the same density). On the other hand, PIMC energies lie below the available experimental energies of the bcc solid in an amount ~ 0.20 K, a feature already observed in liquid ^{4}He and attributable to the particular Aziz potential used in the present simulations [4].

In Table 5.2, we also have included the partial energies per particle. The results for the kinetic energy per particle K/N are the most relevant because it is possible to measure them using deep inelastic neutron scattering. As it is well known, if the momentum of the incoming neutron is high enough the impulse approximation holds and the atomic momentum distribution $n(k)$ is attainable, and from it the kinetic energy. Blasdell *et al.* [115] reported experimental results of K/N for both solid lattices: at $T = 1.07$ K and hcp $K/N = 23.6$ K, and at $T = 1.72$ K and bcc $K/N = 23.7$ K (the densities of both phases were the same). If just the classical estimation $3/2k_BT$ is considered for an isothermical comparison, one can see that the kinetic energy of the bcc crystal is significantly smaller. PIMC results by Ceperley [114] also agree with this trend (in this case the comparison is made between fcc and bcc lattices). Our present results allow for a best comparison since they are obtained following the coexistence line. As one can see in Table 1, there is a nearly constant decrease of ~ 0.5 K when going from the hcp point to the bcc one and our results are in overall agreement with the experimental determinations of Blasdell *et al.* [115]. The thermal effects in the kinetic energy for any of the two lattices are dominated by the classical term $3/2k_BT$ that gives a difference of 0.15 K from one point to the next one.

We have also calculated some structural properties of the bcc phase to better characterize it and to identify specific signatures of this lattice symmetry. One of

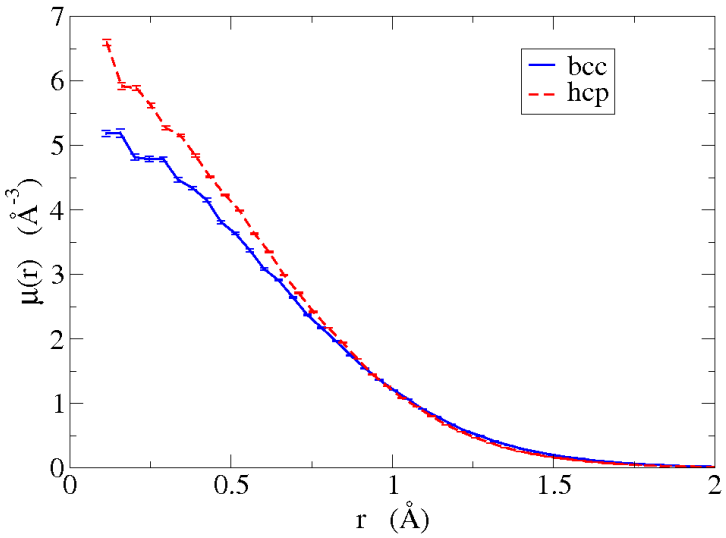

Figure 5.16: Density profile $\mu(r)$ of ^{4}He atoms around the lattice sites for the two lattices at $T = 1.5$ K.

the most relevant in the microscopic study of any solid phase is the density profile $\mu(r)$, defined as the probability of finding a particle in the interval $(r, r+dr)$ around any of the lattice points of the crystal. Results of $\mu(r)$ at the thermodynamic point A and for the two coexistence lattices are shown in Fig. 5.16. As expected, the density profile of the bcc crystal is a bit wider than the hcp one, with a decrease of localization as it corresponds to its slightly more open structure. From the density profile it is possible to calculate the mean squared displacement around a site,

$$\langle \mathbf{u}^2 \rangle = 4\pi \int_0^\infty dr\, r^4 \mu(r) \ , \tag{5.2}$$

and from it to estimate the Lindemann ratio,

$$\gamma = \frac{\sqrt{\langle \mathbf{u}^2 \rangle}}{a} \ , \tag{5.3}$$

a being the nearest-neighbor distance in the perfect crystalline lattice. We have obtained $\gamma_{\rm hcp} = 0.26$ and $\gamma_{\rm bcc} = 0.28$, in agreement with experimental data [3]. The Lindemann ratio is a good measure of the zero-point motion and thus the larger value of γ for the bcc lattice points to an enhancement of its quantum nature.

In Fig. 5.17, we show results of the two-body radial distribution function for both lattices in the coexistence at $T = 1.5$ K. One can see the usual oscillations due to the periodic spatial order and only a tiny difference between both lattices. The height of the main peak of the bcc $g(r)$ is slightly smaller than the hcp one but this is more an effect of its smaller density than a consequence of the lattice symmetry. The difference in the spatial order induced by the lattice is more clear in reciprocal space. Results for the static structure factor $S(q)$ at both sides of the

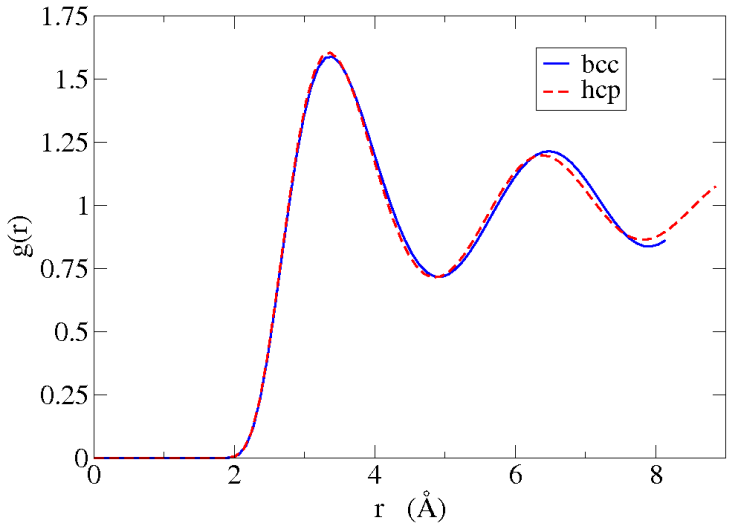

Figure 5.17: Two-body radial distribution function for the hcp and bcc phases of solid ^{4}He at $T = 1.5$ K.

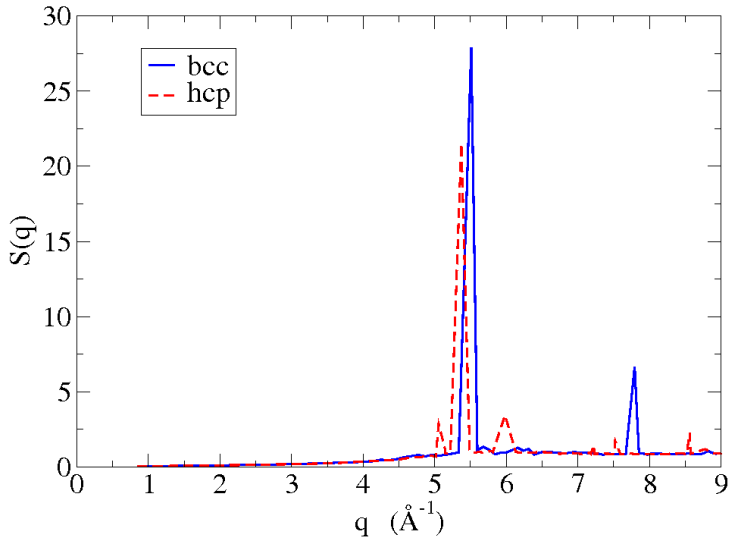

Figure 5.18: Static structure factor for the hcp and bcc phases of solid ^{4}He at $T = 1.5$ K.

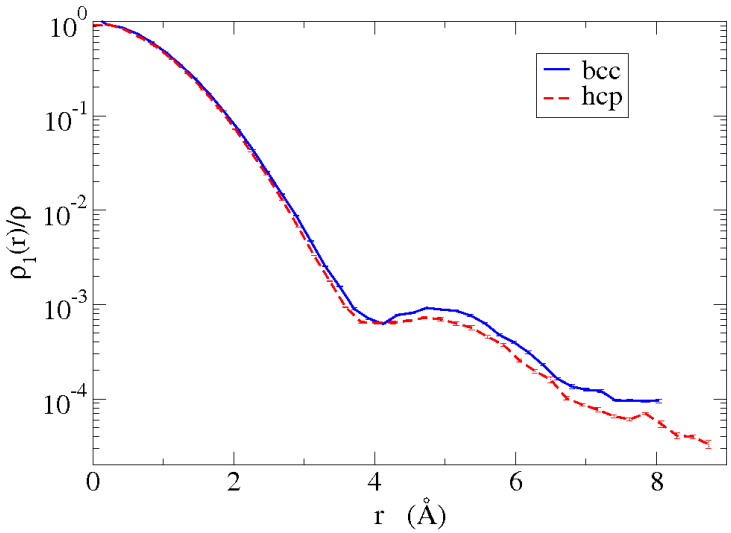

Figure 5.19: One-body density matrix for the hcp and bcc phases of solid ^{4}He at $T = 1.5$ K.

coexistence line at $T = 1.5$ K are shown in Fig. 5.18. Several Bragg peaks are clearly identified; they are located at the expected points for each type of lattice. As it is well known from solid state physics, the determination of the static structure factor is the best way for identifying the particular lattice of the crystal and, indeed, the x-ray measures by Schuch and Mills [107] were the definite prove of the existence of a stability region for bcc ^{4}He.

Much of our present interest in the bcc phase of solid ^{4}He lies on the unexpected results found by Eyal *et al.* [103] which point to disorder-induced mobility, that manifests in the torsional oscillator experiments as the typical mass decoupling observed in hcp at very low temperatures ($T < 200$ mK). This could open the possibility of a supersolid scenario at higher temperatures. Any signature of supersolidity would appear in off-diagonal properties of the system, like the one-body density matrix $\rho_1(r)$. In Fig. 5.19, we show results for $\rho_1(r)$ at $T = 1.5$ K calculated for the two lattices. The shape of the two results is very similar and coincides with previous estimations: a fast decay up to ~ 4 Å, a small increase near the position of the first neighbor, and finally a kind of exponential decay to zero. The most relevant feature of these results is the absence of off-diagonal long-range order. Therefore, neither the perfect hcp crystal nor the perfect bcc one show signals of supersolidity according to our PIMC results.

Chapter 6

Superfluidity of bulk $p\mathbf{H_2}$ at low temperature

Molecular para-hydrogen (pH$_2$) has been proposed theoretically as a possible candidate for superfluidity, but experimentally the eventual superfluid transition is hindered by the crystallization of the pH$_2$ system. In this work, we study a metastable non crystalline phase in bulk pH$_2$ by means of the Path Integral Monte Carlo method in order to investigate at which temperature this system can support superfluidity. Choosing accurately a "quantum liquid" initial configuration and using a non commensurate simulation box, we have been able to frustrate the formation of the crystal in the simulated system and to calculate the temperature dependence of the one-body density matrix and of the superfluid fraction, showing a transition to a superfluid phase at temperatures around 1 K.

6.1 Introduction

The search for elements exhibiting superfluid properties, in addition to helium isotopes, is a fundamental issue in the study of the phenomenon of superfluidity and has been a matter of continuous study in the scientific community for many decades.

Ginzburg and Sobyanin, in 1972, speculated that any Bose liquid should be superfluid below a certain temperature T_λ, unless it solidifies at temperature T_f higher than T_λ [8]. To give a first estimation of T_λ, they used the theory for the ideal Bose gas, obtaining

$$T_\lambda = 3.31 \, \frac{\hbar^2}{g^{2/3} m k_B} \rho^{2/3} \ , \tag{6.1}$$

where m is the atomic mass, g is the spin degeneracy, k_B is the Boltzmann constant and ρ is the density of the system. Ginzburg and Sobyanin proposed molecular para-hydrogen (pH$_2$) as a plausible candidate for superfluidity: being a spinless boson (with $g = 1$) with a small mass, pH$_2$ should undergo a superfluid transition at a relatively high temperature (according to Eq. 6.1, $T_\lambda \simeq 6$ K).

However, we can easily realize that the estimation of T_λ given by Eq. 6.1 is unsatisfactory in case of dense liquids because it cannot account for the observed dependence of T_λ with the density: in liquid ^{4}He, indeed, T_λ does not increase as $\rho^{2/3}$ but it slightly decreases when the sample is compressed. In order to provide a more reasonable estimation of T_λ, Apenko proposed a phenomenological criterion for the superfluid transition, similar to the Lindemann criterion for crystal melting

[118]. In this way, he has been able to take into account the quantum decoherence effects due to the strong interatomic potential and to relate the critical temperature for superfluidity with the mean kinetic energy per particle above the transition. For $p\mathrm{H}_2$, he obtained that T_λ should vary between 1.1 K and 2.1 K, depending on the density of the system.

The main obstacle for the experimental observation of superfluidity of $p\mathrm{H}_2$ is due to the freezing of the sample, which occurs at temperature $T_f = 13.8$ K, higher than the estimated T_λ. Several studies about crystal nucleation in $p\mathrm{H}_2$ have been performed in order to understand if the liquid can enter a supercooled phase, i.e., a metastable phase in which the liquid is cooled below its freezing temperature without forming a crystal. In Ref. [119], Maris *et al.* calculated the rate $\Gamma(T)$ of homogeneous nucleation of the solid phase from the liquid as a function of the temperature T, showing a maximum of Γ around $T = 7$ K and a rapid decrease at lower temperature. This suggests that, if it would be possible to supercool the liquid through the range where Γ is large, one in principle might be able to reach a low-temperature region where the liquid is essentially stable.

However, recent experiments have indicated that, even at $T \sim 9$ K, the rate of crystal growth is so high that the liquid phase freezes quickly into a metastable polymorph crystal [9].

Even though several supercooling techniques have been proposed so far to create a metastable liquid phase in bulk $p\mathrm{H}_2$ [120, 121, 122], none of them has proven to be successful and no direct evidence of superfluidity has been detected. Anyway, the interest in this topic is kept alive by some results pointing, at least indirectly, to a superfluid behavior of $p\mathrm{H}_2$ coming from spectroscopic studies of doped small clusters. In 2000, Grebenev *et al.* analyzed the rotational spectra of a linear carbonyl sulfide (OCS) surrounded by 14 to 16 $p\mathrm{H}_2$ molecules absorbed in a larger helium droplet which fixes the temperature of the cluster [10]. In the pure ^{4}He droplet ($T = 0.38$ K), the measured spectra shows a peak indicating the excitation of angular momentum around the OCS axis. When the small $p\mathrm{H}_2$ cluster is put inside a colder $^4\mathrm{He}/^3\mathrm{He}$ droplet ($T = 0.15$ K), the peak disappears: this indicates that the OCS molecule is able to rotate freely inside the hydrogen cluster, indicating thus the possibility for superfluidity effects to occur in $p\mathrm{H}_2$.

These results have been confirmed in a later experiment on small $p\mathrm{H}_2$ clusters doped with carbon dioxide [123]. From a precise analysis of the rotational spectra, it has been possible to measure the effective momentum of inertia of these small systems, and thus of their superfluid fraction ρ_s, providing a clear evidence of superfluidity in clusters made up of $N \leq 18$ $p\mathrm{H}_2$ molecules. However, authors do not answer the question whether or not larger cluster will exhibit the same behavior.

In spite of the relevance of these results, they are not able to provide a definitive answer in the debate of a possible superfluid transition in $p\mathrm{H}_2$. Indeed, it is questionable to speak about superfluidity when dealing with systems composed of few particles: in these very small systems, all the molecules reside essentially on the surface and their interaction with the impurity can, in principle, affect the experimental results. Larger pure clusters are more suitable to describe the bulk phase:

Kuyanov-Prozument and Vilesov have been able to stabilize the liquid phase in clusters with an average size of $N \approx 10^4$ $p\mathrm{H}_2$ molecules down to the temperature $T = 2$ K, but they do not see any evidence of superfluidity effects in the studied clusters [124].

From the theoretical point of view, the interaction between $p\mathrm{H}_2$ molecules at low temperature can be well described by a radial potential, thanks to the spherical symmetry of its rotational ground state [125]. This feature makes feasible an *ab-initio* study aimed to detect a possible superfluid phase in $p\mathrm{H}_2$ at low temperature. The PIMC method has been widely used to perform finite temperature simulations of $p\mathrm{H}_2$ films [126, 127] and small clusters, both doped with impurities [128, 129, 130] and pure ones [131, 132, 133, 134, 135]: all these simulations show the possibility for $p\mathrm{H}_2$ to become superfluid below a certain temperature and seem to point out also to a dependence of the superfluid fraction on the dimensions of the system, indicating that it goes to zero for large enough systems. Nevertheless, it is not clear to which extent these conclusions can be generalized to systems of infinite size.

The aim of the present chapter is to provide a microscopic description of a non crystalline phase in bulk $p\mathrm{H}_2$ at finite temperature. Such a microscopic study by means of the PIMC method is not easy since the deep attractive well in the intermolecular potential of $p\mathrm{H}_2$ makes rather hard the sampling of the coordinates and makes necessary the use of a very accurate sampling scheme in order to perform a reliable simulation of the system. To overcome these sampling issues, we have used the Chin factorization to approximate the thermal density matrix [20] and the worm algorithm for sampling the bosonic permutations [7]: with these improvements we have been able, for the first time, to simulate microscopic system with almost 100 $p\mathrm{H}_2$ molecules and with periodic boundary conditions at very low temperatures. Our main purpose is to estimate the temperature T_λ of the superfluid transition, in order to improve the result given by Apenko using a phenomenological description [118]. In this chapter, we will discuss at first the techniques we use to stabilize, inside the simulation box, a non crystalline configuration for $p\mathrm{H}_2$ at low temperature (Sec. 6.2). Later on, we will focus our attention on the superfluid properties, studying the temperature dependence of both the superfluid fraction and the one-body density matrix (Sec. 6.3).

6.2 Equilibration of the amorphous phase

The first difficulty we have to deal with when investigating computationally a disordered phase of $p\mathrm{H}_2$ at low temperature is to provide a good equilibration of the system. The PIMC method, indeed, is aimed at studying the thermodynamic properties of quantum systems at thermal equilibrium. On the contrary, our purpose here is to study a configuration different from the one of minimum free energy, which for $p\mathrm{H}_2$ at low temperature is the crystalline one.

In order to do that, it is fundamental to take care in the choice of the dimensions of the simulation box and of the number of particles, which must not be

commensurate with any crystalline lattice. Also, it is important to choose a good initial configuration which evolves, as the Monte Carlo simulation goes on, towards a non crystalline phase which remains metastable for a number of Monte Carlo steps large enough to get a good statistics of the relevant quantities of the system. In this equilibration process, special attention must be paid also to the thermalization of the polymers used within PIMC formalism to describe classically the quantum molecules. A bad choice of initial conditions, indeed, may cause the evolution of the system towards a configuration where the classical polymers are not allowed to spread and thus are not able to describe properly the zero-point motion of the molecules. This eventuality may represent a serious problem in our simulation, since we are mainly interested in the investigation of the superfluid properties of the $p\mathrm{H}_2$ system.

To check whether an equilibration scheme is efficient or not, it is important to monitor how the numerical estimations of the physical quantities change with the number of Monte Carlo steps. If we see that, as the simulation goes on, the computed variables do not show any evident trend but they fluctuate around a certain value, we can conclude that the system has reached the metastability. To check if this eventual metastable phase is crystalline or not, we can calculate the static structure factor $S(q)$ and observe if it presents the Bragg peaks typical of a crystalline configuration.

The simplest disordered configuration we can try for equilibrating the $p\mathrm{H}_2$ system is the one of a classical gas, where all the polymers are concentrated in a point and their position is chosen randomly inside the box: this is the typical initial condition used in the PIMC simulation of quantum liquids at equilibrium. Anyway, we can easily realize that, in the present case, such a configuration does not provide a good equilibration. At first, a completely random disposition of the atoms may present many superpositions, i.e. many pairs of particles at a distance lower than the hard-core of the interatomic potential, which make the configuration particularly unstable. Furthermore, since the polymers in the first steps are concentrated in a point, they can move quite easily and the system will relax to a non liquid configuration, structured at least on the short range, before the polymers have thermalized in a proper way.

A clever way to generate a better initial configuration is to equilibrate the $p\mathrm{H}_2$ system with the Diffusion Monte Carlo (DMC) method. An exhaustive description of DMC method can be found in Ref. [17]. Briefly, DMC is an established technique which has produced excellent results for a wide range of properties of quantum systems at zero temperature. It is capable of finding the ground state of bosonic systems solving the time-dependent Schrödinger equation in imaginary time. Although it can be considered an "exact" method, since it is able to make the systematic errors arbitrarily small, for practical purposes DMC needs the choice of a trial wave function describing accurately the real ground state of the quantum system to provide an efficient importance sampling. If the trial wave function differs from the ground state, the importance sampling of DMC can introduce correlations which can stabilize an off-equilibrium configuration in the simulation. Therefore,

DMC can be used for our purpose of equilibrating a non-crystalline phase for $p\mathrm{H}_2$ at low temperature.

Using this feature of the DMC method, we propose an equilibration process which consists of two steps. In the first part, we perform a DMC simulation using, for the importance sampling of the coordinates, a Jastrow trial wave function $\Psi_T = \prod_{i<j} f(r_{ij})$. This wave function is a product of two-body correlation factors and does not present any localization term, allowing thus for a good description of the liquid phase. Once the DMC simulation has equilibrated the liquid state, we construct the initial configuration for our PIMC simulation from the final DMC one. More precisely, we construct the PIMC configuration concentrating all the bead for each polymer in the coordinates of a walker obtained at the end of the DMC simulation. With respect to the classical gas equilibration scheme presented above, this procedure allows us to get a more "liquid" disposition of the molecules inside the box, where the pairs of neighbors will find themselves at distances of the order of the minimum of the interatomic potential and their superpositions become less probable. In this way, since the initial configuration is close to a local minimum of the many-body Hamiltonian, the global moves of the polymers should not displace them largely from the starting point and, in principle, the movements of the beads inside a single polymer should be able to allow for a good thermalization of the whole system before the system relaxes to a crystalline phase.

To test this equilibration scheme, we have performed a simulation of $N = 100$ $p\mathrm{H}_2$ molecules interacting through the Silvera-Goldman potential [136], inside a cubic box at the density $\rho = 0.0234\,\text{Å}^{-3}$. This density is the equilibrium density of the liquid phase at zero temperature as obtained in a DMC simulation [137]. For a preliminary test, we choose to perform the PIMC simulation at the temperature $T = 10$ K, that is an intermediate temperature below the freezing temperature, where the liquid phase should be unstable, but above the estimated superfluid transition temperature, in order to make the simulation easier. In Fig. 6.1 we plot how the total energy per particle changes during the PIMC simulation (black symbols). We can easily see that, during the simulation, the energy is oscillating around two different values (it is clear especially if we focus the part of the simulation between the Monte Carlo blocks 60 and 120). This trend indicates that this equilibration scheme may introduce some instabilities in the system and suggests us to follow a different way in order to metastabilize the liquid phase.

In particular, a weak point of the previous equilibration scheme is the starting of the PIMC simulation from a classical point configuration. It would be better, in order to get a better thermalization of the polymers, to begin the PIMC simulation from a configuration where the polymers are not concentrated in a point. To do that, we have followed a different equilibration process which consists in two parts. In the first part, we perform the simulation of a fictitious system of quantum particles with the mass equal to that of $p\mathrm{H}_2$ molecule, but interacting between each other through the Aziz potential, which describe the interaction between ^{4}He atoms [49]. Contrary to the Silvera-Goldman potential, the Aziz potential does not present a so deep attractive well and is not able to induce, at sufficiently low densities,

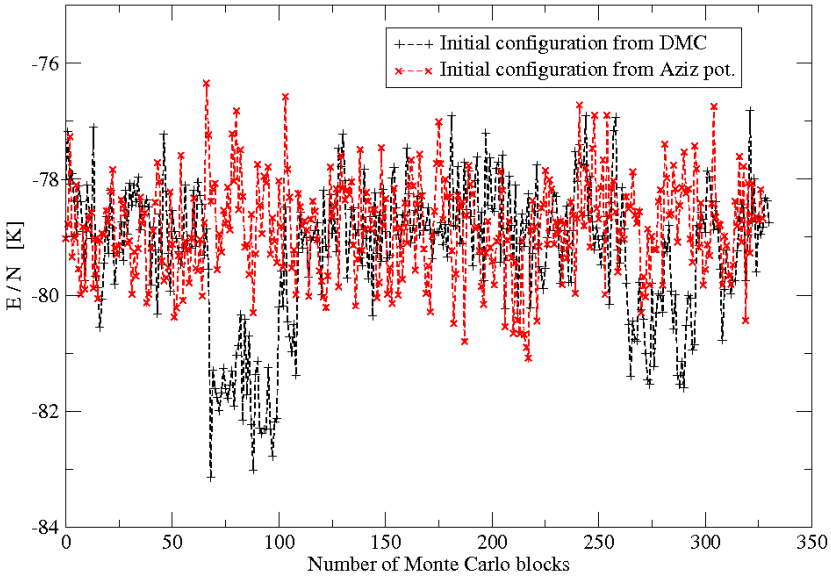

Figure 6.1: Mean values of the energy per particle E/N computed for consecutive blocks during a typical PIMC simulation of $p\mathrm{H}_2$ at temperature $T = 10$ K. The black + symbols represent the simulation started from a liquid configuration equilibrated with Diffusion Monte Carlo. The red $\times$ symbols represent the simulation started from a liquid configuration obtained in a fictitious PIMC simulation of $p\mathrm{H}_2$ molecules interacting with Aziz potential.

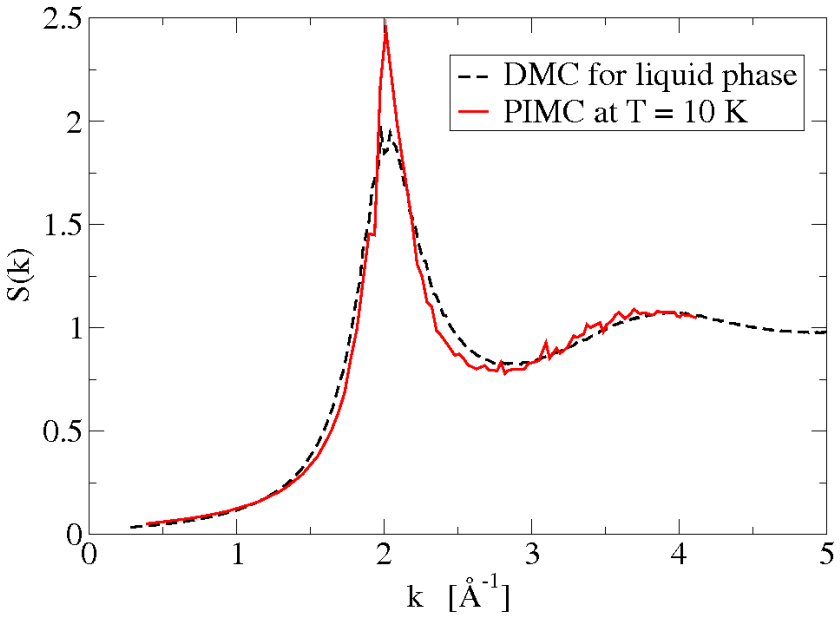

Figure 6.2: Static structure factor $S(k)$ of the metastable phase of bulk $p\mathrm{H}_2$ at $T = 10$ K obtained with PIMC (red straight line). Our result is compared with the static structure factor for liquid $p\mathrm{H}_2$ at zero temperature obtained with DMC (black dashed line)

a crystalline phase. Therefore, the new idea for equilibrating the $p\mathrm{H}_2$ system is to perform such a fictitious PIMC simulation starting from a classical gas configuration (point polymers put randomly inside the simulation box): in this fictitious PIMC simulation, thanks to the weaker interatomic potential, it is possible to create easily a "quantum liquid" configuration, where, in addition to the spatial correlations typical of the liquid phase, are taken into account also quantum effects due the zero-point motion of the quantum particles. Later, we use exactly the final configuration of this fictitious system to start the real simulation of the $p\mathrm{H}_2$ system.

To test this new equilibration procedure, we repeat the previous simulation of $N = 100$ $p\mathrm{H}_2$ molecules at the same density $\rho = 0.0234$ Å^{-3} and temperature $T = 10$ K: the results for the total energy per particle E/N as a function of the number of Monte Carlo blocks is plotted in Fig 6.1 (red symbols) and compared with the same quantity obtained following the previous equilibration scheme. In this case, E/N oscillates during the whole simulation around the same mean value $\langle E/N \rangle \simeq -78\,K$ indicating that the system has reached a metastable configuration. In Fig. 6.2, we have plotted the static structure factor $S(k)$ of the metastable phase and compared it with the same quantity computed for the liquid phase with DMC. We can easily see that the curve obtained at $T = 10$ K presents the first peak at the same k as the $S(k)$ of the liquid and follows more or less the same behavior up to the second maximum which is at $k \simeq 4$ Å^{-1}. Even though the PIMC calculation gives a peak

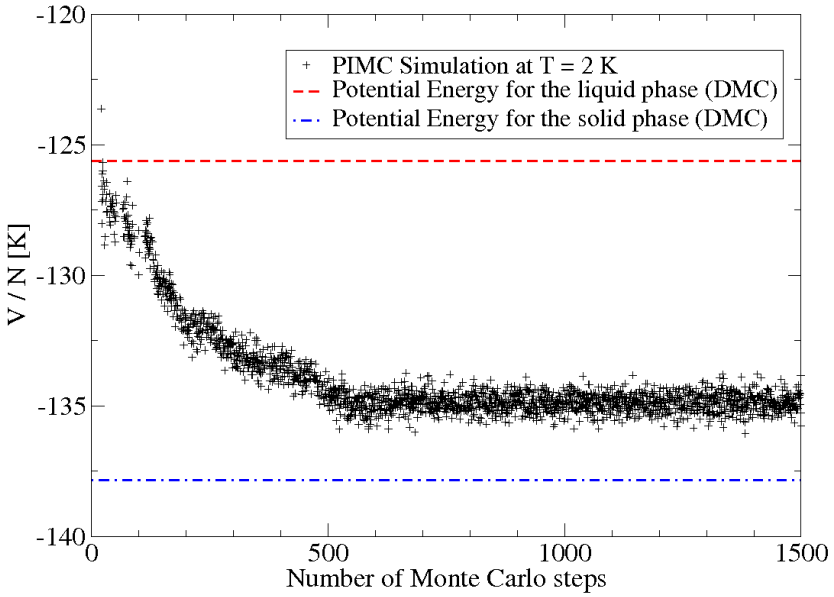

Figure 6.3: Mean values of the potential energy per particle V/N computed for consecutive steps during a typical PIMC simulation of $N = 90$ $p\mathrm{H}_2$ at temperature $T = 2$ K (black + symbols). The evolution of the potential energy during the simulation is compared with the mean value of the potential energy of a liquid (red dashed line) and of a crystalline (blue dot-dashed line) phase, obtained at zero temperature from a DMC simulation of the same system.

which is higher and narrower than the peak obtained with DMC and indicates that the PIMC configurations are slightly more structured than the DMC ones, we can safely conclude that our equilibration scheme is able to create a metastable liquid phase, at least in the range of intermediate temperature below the freezing point T_f and above the expected superfluid transition T_λ.

Nevertheless, since our main purpose is to localize the superfluid transition of this non crystalline phase, it is worth to test this equilibration scheme even at temperatures which are closer to the expected T_λ. For this reason we have performed the simulation of $N = 90$ $p\mathrm{H}_2$ molecules at same density $\rho = 0.0234\,\text{Å}^{-3}$ but at a lower temperature, $T = 2$ K. In Fig. 6.3 we show how the potential energy per particle V/N varies as the PIMC simulation follows. We choose to focus on the potential energy, rather than in total energy, since in this range of low temperature V/N is not strongly dependent on T and we can therefore compare it with the results for V/N at zero temperature obtained with DMC. From the analysis of the results, we can easily see that, after some Monte Carlo steps, the results of V/N reaches a plateau, indicating that the system has relaxed to a metastable configuration. However, this plateau appears at a value of the potential energy considerably lower

than the one obtained in DMC simulation of the liquid phase, indicating that the metastable regime we reach presents features which cannot be considered those of a liquid phase. We have performed also a DMC simulation of $N = 108$ $p\mathrm{H}_2$ molecules disposed according to a fcc lattice in order to understand if the metastable phase obtained in the PIMC simulation can be considered crystalline. In Fig. 6.3 we have shown the result for the potential energy per particle in the solid phase as obtained in the DMC calculation: we can realize that this result is not compatible with the value of V/N reached in the PIMC simulation after the equilibration, indicating that in the PIMC simulation we have reached a phase which cannot be considered crystalline.

To support this hypothesis, we have computed the static structure factor $S(k)$ for the system at $T = 2$ K after the equilibration, when the mean value of the energy is stable. The result is shown in Fig. 6.4, in comparison with the static structure factor for the liquid and crystalline configurations at zero temperature obtained with DMC. As we can see, the $S(k)$ obtained in the PIMC simulation presents narrow maxima in the range of small k and is quite different from the typical $S(k)$ of a liquid phase. However, these maxima tend to disappear at higher k and their height is much lower than the height of the Bragg peaks appearing in the $S(k)$ of a crystal. This indicates that the system simulated with PIMC has relaxed to a glassy phase, which is structured at short range but lacks of the long-range coordination typical of the crystalline structures.

6.3 Search for the superfluid transition

With a clever choice of the initial configuration we have been able to frustrate the formation of the crystal, making a glassy phase metastable at temperatures close to those expected for the superfluid transition. Even if a glassy configuration can make the diffusion of the particles harder, the lack of long range coordination makes possible the appearance of off-diagonal long range order and it is worth to study the superfluid properties of this phase.

To do that, we have studied the temperature dependence of the one-body density matrix $\rho_1(r)$ and of the superfluid fraction. The first simulation has been performed at the temperature $T = 2$ K, using $N = 90$ $p\mathrm{H}_2$ molecules interacting via the Silvera-Goldman potential inside a cubic box at the density $\rho = 0.0234\,\text{Å}^{-3}$. The result for the OBDM obtained in this simulation is shown in Fig. 6.5: at $T = 2$ K, we can clearly see an exponential decay of $\rho_1(r)$ at large r, indicating that Bose-Einstein condensation is not present in the system, resulting thus in a non-superfluid phase. In this simulation, indeed, we have noticed that the swap update has a very low acceptance rate and does not allow the formation of long-permutation cycles with a non-zero winding number. Nevertheless, we can think that the low acceptance of the swap update is a consequence of the difficulties in the sampling of the coordinates due to the strength of the intermolecular potential. We may therefore suspect that the system remains stuck in a configuration without permutation because of sampling

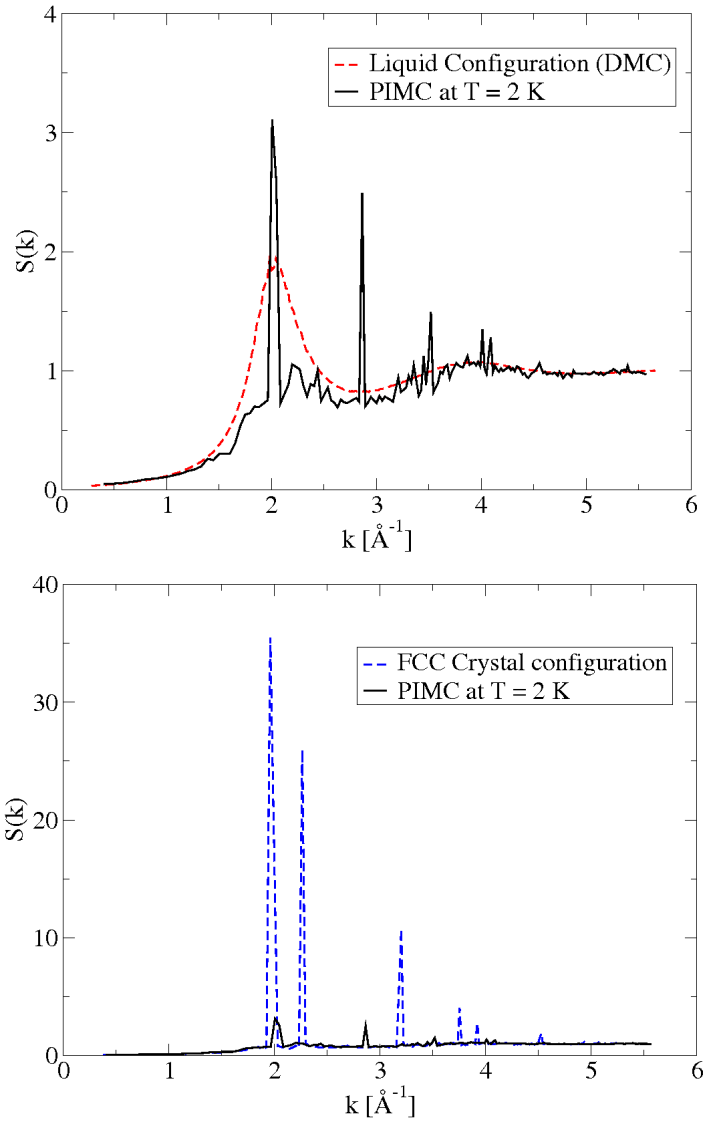

Figure 6.4: Static structure factor $S(k)$ of the metastable phase of bulk $p\mathrm{H}_2$ at $T = 2$ K obtained with PIMC (black straight line). Top figure: comparison of the PIMC result with the static structure factor for liquid $p\mathrm{H}_2$ at zero temperature obtained with DMC (red dashed line). Bottom figure: comparison of the PIMC result with the static structure factor for crystalline $p\mathrm{H}_2$ (fcc lattice) at zero temperature obtained with DMC (blue dashed line).

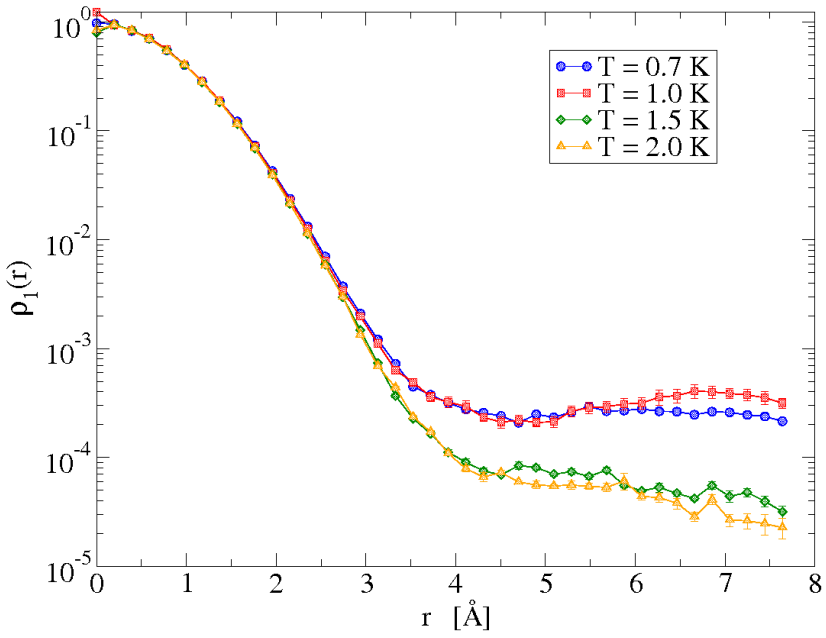

Figure 6.5: The one-body density matrix $\rho_1(r)$ for the glass $p\mathrm{H}_2$ at density $\rho = 0.0234\,\text{Å}^{-3}$ and at different temperatures: $T = 0.7\,\mathrm{K}$ (blue circles), $T = 1.0\,\mathrm{K}$ (red squares), $T = 1.5\,\mathrm{K}$ (green diamonds) and $T = 2.0\,\mathrm{K}$ (yellow triangles). Statistical errors, if not displayed, are below symbol size.

issues. To make sure about our result, we have performed another simulation of the same system but starting from an initial configuration presenting a non-zero winding number. To create this initial configuration, we have allowed particles to permute even in the fictitious simulation used to equilibrate the system. When we start the PIMC simulation of $p\mathrm{H}_2$ from the permutated configuration, we see that the percentage of particles involved in bosonic exchanges tends to decrease and, at the end of the equilibration, the system has relaxed to a phase presenting zero winding number. This last result confirms our conclusion that the $p\mathrm{H}_2$ glass we simulate is not superfluid at $T = 2$ K.

In Fig. 6.5 we have shown, together with the result at $T = 2$ K, also the OBDM obtained from the simulations at other different temperatures. At each of the temperatures studied, we have performed simulations starting both from a permutated and a non permutated configuration, observing that, once that the system has been equilibrated, the results for $\rho_1(r)$ does not depend on the initial configuration. From the comparison of the curves at different temperatures, we can easily see a change of the behavior of ρ_1 at large r as the temperature decreases: this indicates that, at temperature close to $T = 1$ K, the system presents a transition to a superfluid phase presenting off-diagonal long range order. The condensate fraction at low temperature is $n_0 \sim 3 \times 10^{-4}$. The evidence of a superfluid transition

T [K]	ρ_s/ρ
0.7	1.15 ± 0.14
1.0	0.53 ± 0.08
1.2	0.
1.5	0.
2.0	0.

Table 6.1: Superfluid density of the metastable glassy phase of $p\mathrm{H_2}$ at density $\rho = 0.0234\,\text{Å}^{-3}$ as a function of the temperature

is supported also by the results of the dependence of the superfluid fraction as a function of the temperature, which is indicated in Table 6.1. Notice that, at $T = 0.7$ K the mean value of the superfluid fraction is higher than one: this is a numerical effect due to the fact that the winding number estimator has no upper bound. However, we have to notice that the statistical error on this estimation is quite large and the result is compatible with $\rho_s/\rho = 1$. Therefore, this result has to be interpreted as an evidence of the fact that, at $T = 0.7$ K, the system is completely superfluid.

In order to give a more precise estimation of the superfluid transition temperature T_λ, it would be necessary to perform a pertinent finite size-scaling study. However, the difficulties of sampling the coordinates of the $p\mathrm{H_2}$ system make the simulation of system made up of more than 100 molecules quite hard. Nevertheless, considering the appearance of a non-zero winding number only at temperature below 1 K and the fact that at 0.7 K the system is completely superfluid, we can localize the superfluid transition close to $T_\lambda \sim 1\,\mathrm{K}$.

This estimation is somehow lower than the estimation given by the phenomenological theory of Apenko [118] for which, at the density $\rho = 0.0234\,\text{Å}^{-3}$ studied in our simulations, the temperature for the transition is estimated $T_\lambda \sim 1.7\,\mathrm{K}$. The reason of the discrepancy can be twofold. At first, we can attribute this difference to some lacks in the phenomenological theory, which may not be able to describe all the correlations arising between the molecules. Secondly, it is legitimate to doubt if the system studied according the two different approaches presents the same feature. Apenko in his work claims that the phenomenological theory applies to dense quantum liquid, while in the PIMC simulation we show that the system is more similar to an amorphous solid than to a liquid. We can therefore think that the lower PIMC estimate for T_λ is due to the fact the more structured configuration enhances the decoherence effects and lower the temperature at which quantum effects become important.

It is also interesting to notice that our estimation for T_λ is quite close to the temperatures at which, according to PIMC simulations, superfluid effects should appear in small $p\mathrm{H_2}$ clusters [131, 132]. These calculations, indeed, show that clusters made of $N \leq 20$ $p\mathrm{H_2}$ molecules exhibit a non-zero superfluid fraction below $T \sim 2$ K. This transition temperature depends on the dimension of the cluster, decreasing

when the number of molecules increases. However, it is difficult to make hypothesis on the superfluid behavior of large enough $p\mathrm{H}_2$ systems from the simulation of small clusters, because the calculated superfluid fraction ρ_s is significantly depressed when the number of molecules becomes $N \geq 30$. This unexpected behavior of ρ_s with N has been explained relating the changes in the superfluid properties to structural changes that make the molecules dispose according to a solidlike configuration when the dimension of the cluster becomes large. In our simulation of bulk $p\mathrm{H}_2$, we have been able to overcome this problem with a good equilibration of the system and we have shown that $p\mathrm{H}_2$ at low temperature may support a superfluid behavior also in systems with infinite dimensions.

Chapter 7

Conclusions and Outlook

In this thesis, we have performed numerical simulations of some of the most relevant quantum fluids and solids by means of the Path Integral Monte Carlo method (PIMC). PIMC is a very powerful method in the study of quantum many-body systems thanks to its capability of providing exact results setting the Hamiltonian as the only input of the simulation. We have developed an efficient code, implementing the most recent and most effective tools, such as the high-order Chin factorization for the thermal density matrix [19, 20] and the worm algorithm [7], in order to obtain in the simulation a reliable description of the properties shown by the system in the experiments. To test the code, we have applied it to the study of liquid ^{4}He, for which a large amount of experimental data is available. We have seen that, both at finite and zero temperature, the numerical results are in good agreement with the experimental measurements. Finally, we have applied the same methodology to the study of other very interesting physical systems, like the solid phase of ^{4}He or molecular parahydrogen at very low temperature.

Next on, we report the main conclusions reported in this thesis.

7.1 One-body density matrix, momentum distribution and condensate fraction of liquid ^{4}He

Motivated by recent accurate experimental data on the condensate fraction n_0 as a function of the pressure p in liquid ^{4}He at temperatures very close to absolute zero [71], in chapter 4, we have computed the one-body density matrix of liquid ^{4}He at different densities by means of the PIGS Monte Carlo method. Our calculations provide an improvement with respect to other ground state projection techniques used in the past, since the PIGS method allows us to remove completely the influence of any input trial wave function. Thanks to this feature of the PIGS method, we have been able to perform calculations of $\rho_1(r)$ and n_0 in liquid ^{4}He at zero temperature relying only on the Hamiltonian and on the symmetry properties of the system.

Although it is not easy to give an analytic model to fit the data for $\rho_1(r)$, because of the difficulty of describing the coupling between the condensate and the excited states in strongly correlated quantum systems such as ^{4}He, it is possible to extrapolate very precise estimates of the condensate fraction and of the kinetic energy of the system even from a simplified model for ρ_1.

At the equilibrium density of liquid ^{4}He, we have recovered the value of n_0 obtained with the unbiased PIMC method at temperature $T = 1\,\mathrm{K}$ [7]. Simulating the system at several densities, the dependence of n_0 with pressure p obtained from

the calculation agrees nicely with the recent experimental measurements of Ref. [71].

7.2 Supersolid phase of ^{4}He

In chapter 5, we have investigated the behavior of solid ^{4}He performing several simulations of condensed helium at high densities, with the atoms organized according to different microscopic configurations, such as perfect hcp crystals, crystals with vacancies and amorphous solids. The main objective was to find a model able to approach theoretically the properties measured experimentally in solid ^{4}He, especially in reference to the recent observation of a non classical rotational inertia (NCRI) in torsional oscillator experiment at low temperature [14, 15].

Concerning the perfect crystal, our results can reproduce the experimental data on the momentum distribution $n(k)$ obtained in neutron scattering experiments [116] and indicates that solid ^{4}He is highly anharmonic, even though its behavior approaches the classical one at high densities. Our results show that a prefect crystal does not present superfluidity effects at any temperature: this behavior is in agreement with previous numerical results [66, 65] and indicates that the model of a perfect crystal is not suitable for describing the NCRI effects observed in the torsional oscillator experiments.

On the other hand, our results shows superfluidity effects in the simulation of crystal presenting defects, such as vacancies. In this case, we show that the one-body density matrix $\rho_1(r)$ depends on the temperature and that, for sufficiently low temperatures, the system supports Bose-Einstein condensation. We have seen that the onset temperature T_0 of BEC in ^{4}He crystals presenting vacancies, calculated using the PIMC method, is comparable with the experimental measurements of the supersolid transition temperature when the concentration of vacancies is small enough ($X_v \sim 2 - 3 \times 10^{-3}$). Furthermore, PIMC simulations show clearly that when this onset temperature is reached the vacancies become completely delocalized objects, as hypothesized in the past [91, 93] and never microscopically observed so far.

In our work, we have also performed a microscopic study of amorphous configurations in solid ^{4}He at densities where the crystalline phase is stable. Our results shows that the glass at a density $\rho = 0.0294\,\text{Å}^{-3}$ becomes superfluid at temperature $T_0 = 0.8\,\text{K}$ (this phase has been referred as *superglass* [84]). This T_0 is a temperature higher than the ones at which NCRI appears experimentally. However, a comparison of our results with experimental ones is quite difficult since the amorphous states are shown to be particularly unstable in real samples above 100 mK [102].

Our work on the solid phase of ^{4}He can be followed studying the temperature dependence of the superfluid fraction with the temperature for crystals presenting other kinds of defects, like stacking faults or partial dislocations. It would be worth also an analysis of the effects of ^{3}He atoms in the microscopic systems simulated with PIMC, since the presence of ^{3}He impurities in real samples seems to affect sig-

nificantly the experimental measurement. In particular, it would be very interesting to study if a ^{3}He atom in a crystal with vacancies can modify the onset temperature of BEC.

In chapter 5, we have also performed a microscopic study of the coexistence hcp-bcc line in solid ^{4}He. Our goal has been to get an accurate view of the possible differences between both lattices along the measured coexistence line. Apart from the intrinsic interest on the study of the bcc phase, which has been scarcely studied in the past, we were stimulated by the recent activity of Polturak and collaborators [103] who have shown intriguing results using the torsional oscillator technique. Our results show a small influence of the lattice type when crossing the coexistence line. The internal energies are similar and the differences between both crystals are more attributable to the slight difference in density than to the particular crystal symmetry. Also the radial distribution functions show only very tiny differences. What is more significant is the drop in the kinetic energy from the hcp phase to the bcc one, that we have estimated to be 0.5 K, and that is in overall agreement with experimental findings [115]. The less compact structure of the bcc solid is also observed in the results obtained for the density profiles and the Lindemann ratios. Finally, we have calculated the one-body density matrix in both sides of the coexistence line without observing any relevant difference between them and, more importantly, without obtaining off-diagonal long-range order which allowed us to conclude that a perfect bcc crystal, at the temperatures where this phase is stable, is not a supersolid.

Further work is needed to determine if the introduction of point defects (vacancies) in the bcc crystal could induce supersolidity at these apparently too high temperatures.

7.3 Superfluidity in bulk $p\mathbf{H_2}$ at low temperature

In chapter 6, we have simulated bulk pH$_2$ at low temperatures, with the purpose of investigating if any condensed system other than helium may support superfluidity. The main difficulties we found in our simulation has been the stabilization of a liquid configuration. Contrarily to what happens in the simulation of bulk ^{4}He, where a overpressurized liquid phase can be made metastable quite easily with a proper choice of the initial configuration and of the dimensions of the simulation box, in pH$_2$ systems at the temperatures estimated for an eventual superfluid transition, the liquid phase presents a high energetic cost that makes it unstable even in short simulation runs. A liquid configuration, indeed, relaxes rather quickly to a glassy phase presenting a more structured configuration at short range but lacking of the long-range structure typical of crystalline systems. These results seem to reflect the difficulty of the experimental techniques to supercool liquid pH$_2$ at very low temperatures [9]. However, we have to remark that PIMC relies on the evolution of the system in imaginary time and cannot describe the real dynamics of the system observed in the experiment, so that our numerical results cannot provide any

information about the possibility to supercool a liquid phase in $p\mathrm{H}_2$ or about the existence of a *metastability limit*, that is a temperature below which crystallization becomes unavoidable.

Nevertheless, computing the one-body density matrix and the superfluid fraction of the glassy phase, we have been able to see clearly a change of the properties of the system, indicating a possible superfluid transition around $T_\lambda \sim 1\,\mathrm{K}$. This temperature is far from the minimum temperatures at which the liquid phase can be supercooled experimentally (in the most recent works, it has not been possible to avoid crystallization below $T \simeq 9\,\mathrm{K}$ [9]). However, our result confirms the hypothesis that $p\mathrm{H}_2$, i.e. a Bose liquid other than helium, shows BEC effects at sufficiently low temperature.

It is important to notice some aspects which can be taken into account in a future development of this study. At first, it would be interesting to study the dependence of the estimated T_λ with the density of the $p\mathrm{H}_2$ system. The phenomenological theory by Apenko predicts that T_λ can vary of about from $T_\lambda \sim 2.1$ K to $T_\lambda \sim 1.1$ K when the density change from $\rho \simeq 0.022\,\text{Å}^{-3}$ to $\rho \simeq 0.026\,\text{Å}^{-3}$ [118] (a similar change in density in liquid ^{4}He will lead to a change in T_λ of about 0.3 K). Some other PIMC calculations could be worth in order to investigate this apparently strong dependence of the transition temperature with the density in $p\mathrm{H}_2$ systems. Another relevant aspect of molecular hydrogen is the possibility of studying the effect of the mass on the superfluid properties of the system, comparing the results for para-hydrogen with the ones for ortho-deuterium ($o\mathrm{D}_2$). This different isotopic form, indeed, presents a mass which is twice the mass of $p\mathrm{H}_2$, but the intermolecular potential for the two species is nearly the same. To this purposes, PIMC simulation of bulk $o\mathrm{D}_2$ would be particularly intriguing.

7.4 Future perspectives

Even though in this thesis we have been able to achieve most of the objectives we proposed at the beginning of the work, there are still some aspects that require further work.

Apart from the natural continuation in the study of the different physical systems analyzed, that we presented in the previous sections of this chapter, we want to focus here to some possible improvement of the PIMC code implemented during this work of thesis.

The main disadvantage in the use of PIMC is the computational effort needed to carry out the simulations, which is particularly onerous with respect to other Quantum Monte Carlo methods. In particular, the computation of the one-body density matrix and of the superfluid fraction are heavy because of the low efficiency of the PIMC estimator for these quantities. It is therefore very important to develop well optimized codes which could reduce as much as possible the time needed for the computation. In our work, we could only develop an optimized serial code, neglecting, for lack of time, the implementation of a parallel version of the program.

Nonetheless, PIMC simulations are really suitable to be performed on parallel machines, both on distributed memory and on shared memory machines.

The simplest parallelization approach consists in a redistribution of the Monte Carlo steps on several nodes, in order to perform more independent simulations at the same time, whose results will be averaged at the end of the calculation. This approach can be easily implemented on parallel distributed memory machines, in which every processor has its own local memory and exchanging values of variables between the nodes involves explicit communication over the network. When developing a code on this particular class of parallel machines, it is important to make the number of communications between the nodes as little as possible, since the interchange of data between the nodes can reduce the performance of the parallel code, especially because of synchronization issues. Nevertheless, this limitation of the distributed memory machines does not involve many problems in the parallelization of the PIMC code. In this case, indeed, the communication between the nodes will be limited only at the beginning of the simulation, when the master node send the input data to all the processors, and at the end, when it receives from the different processors the output data. Furthermore, since all the nodes perform independent simulations whose execution time is very similar, the processors can be easily synchronized.

This approach is the one typically adopted to implement PIMC codes in the first parallel machines, using the Message Passing Interface (MPI) libraries. Nevertheless, in the last years, a new class of parallel computers has been developed and has achieved a certain success: the shared memory parallel machine. In these computers, multiple processors can operate independently sharing the same memory resources, so that changes in a memory location performed by one of the processors are visible to all the others. In this type of computers, thanks to the presence of a shared memory, the communication between the nodes is much easier than in distributed memory machines, making efficient also parallelization schemes which require a big interchange of data among the processors. For instance, in the case of PIMC, we can think to parallelize the calculation of the potential action in the sampling of the coordinates, which is the heaviest part of the simulation, redistributing different beads on different nodes. This approach is very effective if all the processors have easy access to the memory area where are stored the coordinates of the beads and can be implemented without difficulties making use of the most recent OpenMP libraries.

It is important to notice that the two approaches presented in this section can be implemented in the same code, since the part which has to be parallelized in the two schemes has a different extension. In the first approach, we want to parallelize the biggest cycle of the simulation, which is called just once and comprises a big amount of instruction. In the second approach, instead, we mean to parallelize an inner cycle of small extension but whose execution is onerous since it is called a huge amount of times during a typical run. Therefore, PIMC is particularly suitable for a parallelization according to a hybrid MPI/OpenMP scheme, which makes use both of MPI and OpenMP libraries and allows to achieve really high performances

especially in modern clusters made up of multicore processors.

Considering the high computational effort needed to perform a PIMC simulation (for instance, to calculate the one-body density matrix in a crystal containing 180 ^{4}He atoms at a fixed temperature and density, we typically average the results of at least 10 simulation, each of these will last about 80 hours), it is really worth to continue our work on the code, developing an efficient parallel algorithm which would allow to reduce considerably the time needed for the calculations.

Appendix A

The Worm Algorithm

In this appendix, we provide a detailed description of the worm algorithm (WA). In its first implementation within the PIMC formalism, discussed in Refs. [21, 7], WA performs the simulation of the quantum many-body system working in the grand canonical ensemble [43]. Here, we describe a different version, which is the one we used for all our simulations, and works in the canonical ensemble: the differences from the grand canonical algorithm are that the number of particles N, instead of the chemical potential μ, is fixed as input parameter and that the number of links (with the term *link* we refer to the ordered pair of two following beads in the same polymer), instead of being variable during the simulation, is kept constant and equal to $N \times M$, M being the number of beads.

A.1 Main features of the algorithm

The fundamental aspect of WA, which crucially distinguishes it from conventional PIMC, is that it operates in an extended configurational space. This new space can be divided into two sectors: the Z-sector, which is nothing but the full configurational space of classical ring polymers used in conventional PIMC, and the G-sector, which is formed by configurations where all the polymers are closed except one which is left open and is referred as the *worm*.

During the PIMC simulation, the system has to be able to fluctuate randomly from Z to G-sector and vice versa: however, at the moment of evaluating the properties of the system, not all the configurations contribute to the evaluation of all the quantities. In particular, configurations in Z-sector can provide estimations for the diagonal observables, such as the energy, the pair distribution function or the superfluid density: for this reason, Z-configurations are usually referred as *diagonal* configurations. On the other hand, the configurations in the G-sector can be used only in the evaluation of off-diagonal observables, such as the one-body density matrix, and are therefore called *off-diagonal* configurations.

As in all Path Integral calculation, each configuration $X = \{\mathbf{R}_1, \ldots, \mathbf{R}_M, \mathbf{R}_{M+1}\}$ has to be considered as an evolution of $\mathbf{R}_j$ in imaginary time, being $\mathbf{R}_j = \{\mathbf{r}_{1,j}, \ldots, \mathbf{r}_{N,j}\}$ a set of the spatial coordinates of all the N particles of the quantum system.

In the Z-sector, we impose the condition $\mathbf{R}_{M+1} = \mathcal{P}\mathbf{R}_1$, $\mathcal{P}$ being one of the $N!$ permutations of the particle index: thus, a diagonal configuration X_Z is defined by a $3 \times N \times M$ matrix indicating the coordinates $\mathbf{r}_{i,j}$ of all the beads of all the particles

(i, with $1 \leq i \leq N$, is the particle index and j, with $1 \leq j \leq M$, is the bead index) and by the table $p(i)$ indicating the permutation $\mathcal{P}$.

The probability distribution for the configuration X_Z is

$$p_Z(X_Z) = \frac{1}{Z} \prod_{j=1}^{M} \rho_F(\mathbf{R}_{j+1}, \mathbf{R}_j; \varepsilon) e^{-U(\mathbf{R}_{j+1}, \mathbf{R}_j; \varepsilon)} \ , \tag{A.1}$$

where

$$\rho_F(\mathbf{R}_{j+1}, \mathbf{R}_j; \varepsilon) = \frac{1}{(4\pi\lambda\varepsilon)^{3N/2}} e^{-\sum_{i=1}^{N} \frac{(\mathbf{r}_{i;j+1} - \mathbf{r}_{i;j})^2}{4\lambda\varepsilon}} \tag{A.2}$$

is the free propagator in the imaginary time ε from the configuration $\mathbf{R}_j$ to $\mathbf{R}_{j+1}$. The function $U(\mathbf{R}_{j+1}, \mathbf{R}_j; \varepsilon)$ is the potential action and incorporates correlations arising from the interactions among particles. In most of the approximation schemes, the evaluation of U reduces to the evaluation of an effective potential $W(\mathbf{R}_j; \varepsilon)$ between the particles (for instance, in the Primitive approximation $W(\mathbf{R}; \varepsilon) = V(\mathbf{R})$). In these cases, it is preferable to use a symmetrized form for the potential action

$$U(\mathbf{R}_{j+1}, \mathbf{R}_j; \varepsilon) = \frac{\varepsilon}{2} [W(\mathbf{R}_{j+1}; \varepsilon) + W(\mathbf{R}_j; \varepsilon)] \tag{A.3}$$

However, it is easy to notice that each configuration $\mathbf{R}_j$ appears twice in Eq. A.1 (both in $U(\mathbf{R}_j, \mathbf{R}_{j-1}; \varepsilon)$ and in $U(\mathbf{R}_{j+1}, \mathbf{R}_j; \varepsilon)$), even for the case $j = 1$ because of the condition $\mathbf{R}_{M+1} = \mathcal{P}\mathbf{R}_1$. This means that, being

$$\prod_{j=1}^{M} e^{-U(\mathbf{R}_{j+1}, \mathbf{R}_j; \varepsilon)} = \prod_{j=1}^{M} e^{-\varepsilon W(\mathbf{R}_j; \varepsilon)} \ , \tag{A.4}$$

the use of a symmetrized or non symmetrized form for the potential action is in the Z-sector formally equivalent.

The normalization factor in Eq. A.1 is

$$Z = \sum_{\mathcal{P}} \int d\mathbf{R}_1 \ldots d\mathbf{R}_M \prod_{j=1}^{M} \rho_F(\mathbf{R}_{j+1}, \mathbf{R}_j; \varepsilon) e^{-U(\mathbf{R}_{j+1}, \mathbf{R}_j; \varepsilon)} \tag{A.5}$$

and can be considered an approximation of the partition function of the quantum system.

In the G-sector, where there is a polymer which is not closed on itself, the condition $\mathbf{R}_{M+1} = \mathcal{P}\mathbf{R}_1$ holds for all the particles but one, namely the particle i_W. Since $\mathbf{r}_{i_W, M+1} \neq \mathbf{r}_{p(i_W), 1}$, an off-diagonal configuration X_G presents an additional point $\mathbf{r}_{i_W, M+1}$ (usually referred as the head of the worm) with respect to any diagonal configuration X_Z: therefore, to specify X_G we need a $3 \times (N \times M + 1)$ matrix of coordinates and the permutation table $p(i)$.

The probability distribution for the off-diagonal configurations is formally equivalent to that of the diagonal one, Eq. A.1,

$$p_G(X) = \frac{1}{Z_G} \prod_{j=1}^{M} \rho_F(\mathbf{R}_{j+1}, \mathbf{R}_j; \varepsilon) e^{-U(\mathbf{R}_{j+1}, \mathbf{R}_j; \varepsilon)} \ , \tag{A.6}$$

apart from the obvious difference is the normalization factor

$$Z_G = \sum_{\mathcal{P}} \int d\mathbf{R}_1 \dots d\mathbf{R}_M d\mathbf{r}_{i_W,M+1} \prod_{j=1}^{M} \rho_F(\mathbf{R}_{j+1}, \mathbf{R}_j; \varepsilon) e^{-U(\mathbf{R}_{j+1},\mathbf{R}_j;\varepsilon)} \tag{A.7}$$

It is worth to notice that, since the condition $\mathbf{R}_{M+1} = \mathcal{P}\mathbf{R}_1$ does not hold for all the particles, Eq. A.4 does not hold. This observation obliges us to take care in the choice of the potential action U, which has to be in a symmetrized form. In practice, if the potential action can be written as in Eq. A.3, we have to put a factor $1/2$ when computing the effective potential W for the bead $j = 1$, which is the one corresponding to the open extremities $\mathbf{r}_{i_W,M+1}$ and $\mathbf{r}_{p(i_W),1}$ of the worm:

$$\prod_{j=1}^{M} e^{-U(\mathbf{R}_{j+1},\mathbf{R}_j;\varepsilon)} = \prod_{j=2}^{M} e^{-\varepsilon W(\mathbf{R}_j;\varepsilon)} \times e^{-\frac{\varepsilon}{2}(W(\mathbf{R}_1;\varepsilon)+W(\mathbf{R}'_1;\varepsilon))} , \tag{A.8}$$

with $\mathbf{R}_1 = \{\mathbf{r}_{1,1}, \dots, \mathbf{r}_{p(i_W),1} \dots, \mathbf{r}_{N,1}\}$ and $\mathbf{R}'_1 = \{\mathbf{r}_{1,1}, \dots, \mathbf{r}_{i_W,M+1} \dots, \mathbf{r}_{N,1}\}$.

Formally, the configurational space of the WA corresponds to an ensemble with a generalized partition function

$$Z_W = Z + CZ_G . \tag{A.9}$$

The parameter $C > 0$ is a dimensionless quantity which remains constant during the whole simulation. Its effect is to control the relative statistics of the Z and G-sector, affecting only the efficiency of the simulation. If we indicate with N_Z and N_G respectively the number of diagonal and off-diagonal configurations sampled in the simulation (with $N_{tot} = N_Z + N_G$), one will have

$$\frac{N_Z}{N_{tot}} = \frac{Z}{Z_W} \tag{A.10}$$

and

$$\frac{N_G}{N_{tot}} = \frac{CZ_G}{Z_W} . \tag{A.11}$$

It follows that

$$\frac{N_G}{N_Z} = \frac{CZ_G}{Z} : \tag{A.12}$$

from the last equation, it is clear that the higher the parameter C the more frequently the system will be found in an off-diagonal configuration. It is worth to notice that Eq. A.12 can provide a good test on the sampling: if the ratio N_G/N_Z is not proportional to C, at least in the range where $N_G/N_Z \sim 1$, the sampling cannot allow for an equilibrated switching from Z to G-sector and vice versa.

A.2 Path sampling methods

In this section, we propose a set of local updates in order to sample the WA configurational space by means of the Metropolis algorithm, described in Sec. 2.1.1. We can divide these updates in three groups:

- Updates that can be performed both in Z and in G-sector (Translate and Staging). In the simulation of systems where it is possible to avoid safely the permutations between the particles, these two updates by themselves are able to produce an ergodic sampling of the coordinates.

- Updates switching from Z to G-sector and vice versa (Open and Close). These two updates form a *complementary pair* [138], that is a pair of updates that are essential one to each other in order to satisfy the detailed balance condition (see also the note at the end of this section).

- Updates sampling the G-sector (Movehead, Movetail and Swap). Among these updates, Swap assumes a particular interest since it is the responsible for the sampling of the bosonic permutations

Hereinafter, we describe one by one the updates we have implemented in our code.

- **Translate**: this update translates a whole polymer as a rigid body. We select at random a particle i_1 and we construct the list of all the particle $i_1, i_2, \ldots, i_{np}$ belonging to the same permutation cycle of i_1. We select a displacement vector $\mathbf{\Delta r} = \{\Delta x, \Delta y, \Delta z\}$, sampling its three coordinates uniformly between 0 and a maximum displacement Δr_{max} fixed as input. Then we perform the movement $\mathbf{r}_{i,j} \to \mathbf{r}'_{i,j} = \mathbf{r}_{i,j} + \mathbf{\Delta r}$ to all the beads of all the polymers in the list obtained previously. The movement is accepted with probability

$$P_{Translate} = \min\left\{1; \exp\left[\sum_{j=1}^{M} U(\mathbf{R}_{j+1}, \mathbf{R}_j; \varepsilon) - U(\mathbf{R}'_{j+1}, \mathbf{R}'_j; \varepsilon)\right]\right\} \ , \quad \text{(A.13)}$$

  with $\mathbf{R}_j = \{\mathbf{r}_{1,j}, \ldots, \mathbf{r}_{1,N}\}$ and $\mathbf{R}'_j = \{\mathbf{r}'_{1,j}, \ldots, \mathbf{r}'_{1,N}\}$. Notice that the kinetic action does not appear in the probability of accepting the update since the movement, translating rigidly the whole polymer, does not change the relative distances between the following beads. The parameter Δr_{max} is chosen in order to have an acceptance rate for the update close to 50%. A schematic representation of the update is shown in Fig. A.1.

- **Staging**: this update redraw a segment of a polymer included between two beads which are kept fixed. We select at random the index i_p of the particle we propose to move and the index j_0 of the first fixed bead. Then, the second fixed bead has index j_0+l, being $l \leq M$ an integer number given in input. Knowing the coordinates $\mathbf{r}_{i_p,j_0}$ and $\mathbf{r}_{i_p,j_0+l}$, we sample a new path $\mathbf{r}'_{i_p,j_0+1}, \ldots, \mathbf{r}'_{i_p,j_0+l-1}$ according to distribution

$$\prod_{j=j_0}^{j_0+l} \sqrt{\frac{m}{2\pi\hbar^2\varepsilon}} \exp\left(-\frac{m}{2\hbar^2\varepsilon}(\mathbf{r}'_{i_p,j+1} - \mathbf{r}'_{i_p,j})^2\right) \ , \quad \text{(A.14)}$$

  with $\mathbf{r}'_{i_p,j_0} = \mathbf{r}_{i_p,j_0}$ and $\mathbf{r}'_{i_p,j_0+l} = \mathbf{r}_{i_p,j_0+l}$. A sampling of the coordinates according to this probability distribution is not easy since all the points we

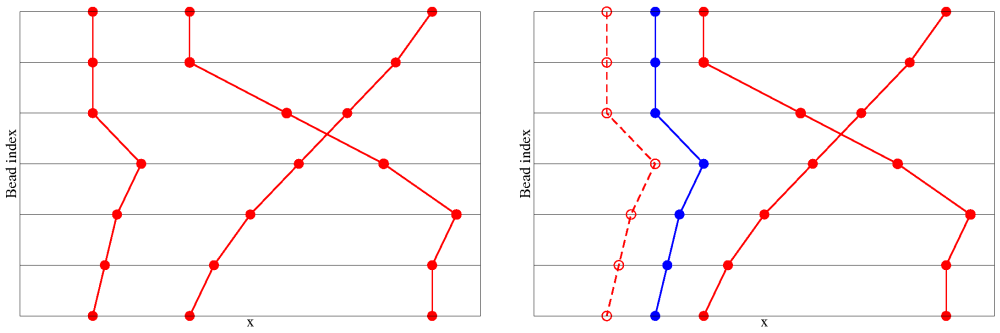

Figure A.1: Schematic representation of the Translation update. On the left, we show the initial configuration of a one-dimensional system of three quantum particles, plotting on the x axis the coordinate of the bead and on the y axis the bead index. On the right we show the configuration after the update: the dashed lines represent the previous configuration and the blue lines and symbols highlights the position of the beads moved in the update.

have to sample are coupled with each other via an effective harmonic potential. However, it is possible to rewrite the product in Eq. A.14 as

$$\begin{aligned}
&\prod_{j=j_0}^{j_0+l-1} \sqrt{\frac{m}{2\pi\hbar^2\varepsilon}} \exp\left(-\frac{m}{2\hbar^2\varepsilon}(\mathbf{r}'_{j+1}-\mathbf{r}'_j)^2\right) = \\
= \quad &\sqrt{\frac{m}{2\pi\hbar^2 l\varepsilon}} \exp\left(-\frac{m}{2\hbar^2 l\varepsilon}(\mathbf{r}_{j_0+l}-\mathbf{r}_{j_0})^2\right) \times \\
&\times \prod_{j=0}^{l-2} \sqrt{\frac{m_j}{2\pi\hbar^2 l\varepsilon}} \exp\left(-\frac{m_j}{2\hbar^2 l\varepsilon}(\mathbf{r}'_{i_p,j_0+j+1}-\mathbf{r}^*_{j_0+j+1})^2\right) ,
\end{aligned} \tag{A.15}$$

with

$$m_j = m\frac{l-j}{l-j-1} \tag{A.16}$$

and

$$\mathbf{r}^*_{j_0+j+1} = \frac{\mathbf{r}_{i_p,j_0+l} + \mathbf{r}'_{j_0+j}(l-j-1)}{l-j} . \tag{A.17}$$

The redefinition of the probability distribution A.14 as in Eq. A.15 is at the basis of the so called *staging* algorithm. This algorithm allow us to avoid the difficulties due to the sampling of coupled harmonic terms and provide easily a sampling of a given segment in a polymer according to a product of independent gaussians [139]. For practical purposes, it consists in a series of following steps in which the new coordinates of $\mathbf{r}'_{i_p,j}$, with $j_0 < j < j_0 + l$, are sampled according to a normal distribution centered in a point $\mathbf{r}^*_{i_p,j}$ depending on the point sampled in the previous step and with standard deviation different at every step. When we reconstruct the segment of the polymer according the

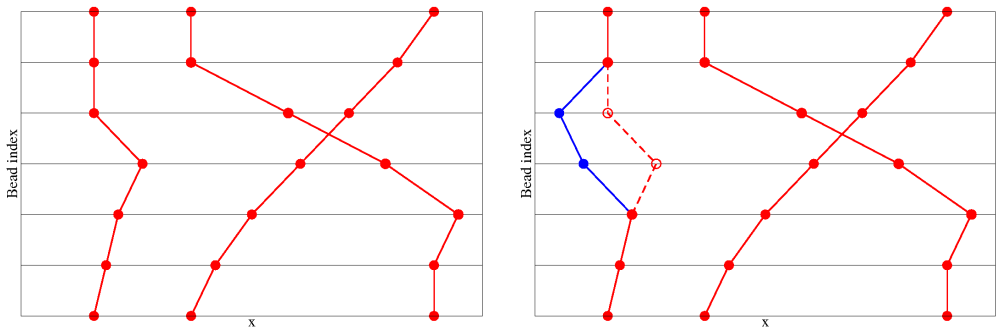

Figure A.2: Schematic representation of the Staging update. On the left, we show the initial configuration of a one-dimensional system of three quantum particles, plotting on the x axis the coordinate of the bead and on the y axis the bead index. On the right we show the configuration after the update: the dashed lines represent the previous configuration and the blue lines and symbols highlights the position of the beads moved in the update.

staging algorithm, the kinetic part of the distribution $p_Z(X_Z)$ or $p_G(X_G)$ is exactly sampled, and therefore in the acceptance probability for the update we have to consider only the potential part:

$$P_{staging} = \min\left\{1; \exp\left[\sum_{j=j_0+1}^{j_0+l-1} U(\mathbf{R}_{j+1}, \mathbf{R}_j; \varepsilon) - U(\mathbf{R}'_{j+1}, \mathbf{R}'_j; \varepsilon)\right]\right\} . \quad \text{(A.18)}$$

Notice that, if $j_0 + l > M$, we use the cyclicity of the closed polymer and define $\mathbf{r}_{i_p, j_0+l} = \mathbf{r}_{p(i_p), j_0+l-M}$. The same consideration has to be done for every sampled point $\mathbf{r}_{i_p,j}$ with $j > M$. However, if we are in the G-sector and we want to reconstruct a segment of the worm ($i_p = i_W$), the previous observation does not old since the open polymer has no cyclicity. In the case of having simultaneously $i_p = i_W$ and $j_0 + l > M$, we simply reject the move before performing any reconstruction.
The parameter l is chosen in order to have an acceptance rate for the update between 30% and 50%. A schematic representation of the update is shown in Fig. A.2.

- **Open**: this update open a closed polymer, allowing the configuration to switch from the Z to the G-sector. Thus, it can be performed only if the system is in the Z-sector. We select randomly a particle index i_p and an integer l, with $1 \leq l \leq l_{max}$, which represents the length, in number of beads, of the segment of the polymer we reconstruct in the update. The parameter $l_{max} < M$ is chosen as input and has to be equal to the value l_{max} used in the Close update. We sample a point $\mathbf{r}'_{i_p,M+1}$ according to a single particle free propagator on

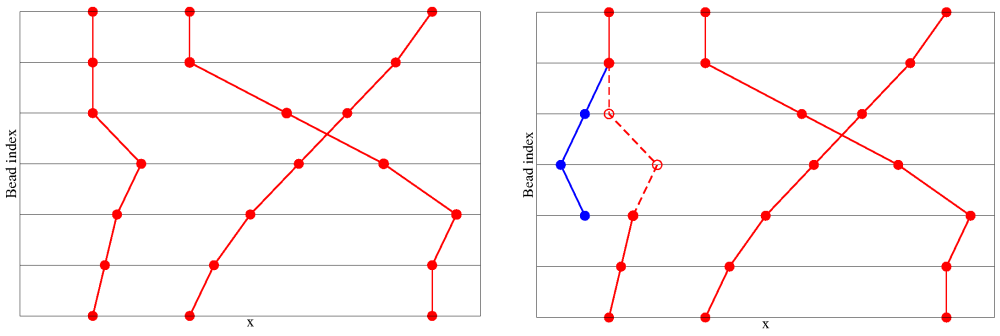

Figure A.3: Schematic representation of the Open update. On the left, we show the initial configuration of a one-dimensional system of three quantum particles, plotting on the x axis the coordinate of the bead and on the y axis the bead index. On the right we show the configuration after the update: the dashed lines represent the previous configuration and the blue lines and symbols highlights the position of the beads moved in the update.

imaginary time $l\varepsilon$ staring on the point $\mathbf{r}_{i_p,M-l+1}$:

$$\rho_{Fsp}(\mathbf{r}'_{i_p,M+1}, \mathbf{r}_{i_p,M-l+1}; l\varepsilon) = \sqrt{\frac{m}{2\pi\hbar^2 l\varepsilon}} \exp\left[-\frac{m}{2\hbar^2 l\varepsilon}(\mathbf{r}'_{i_p,M+1} - \mathbf{r}_{i_p,M-l+1})^2\right] . \tag{A.19}$$

This point $\mathbf{r}'_{i_p,M+1}$ represent the proposal for the new head of the worm. Once we have sampled $\mathbf{r}'_{i_p,M+1}$, we reconstruct with the staging algorithm a free particle path between the first fixed point $\mathbf{r}_{i_p,M-l+1}$ and the new head $\mathbf{r}'_{i_p,M+1}$. At this point, we accept the update with probability

$$P_{open} = \min\left\{1; \frac{C \exp\left[\sum_{j=M-l+1}^{M} U(\mathbf{R}_{j+1}, \mathbf{R}_j; \varepsilon) - U(\mathbf{R}'_{j+1}, \mathbf{R}'_j; \varepsilon)\right]}{\rho_{Fsp}(\mathbf{r}'_{i_p,M+1}, \mathbf{r}_{i_p,M-l+1}; l\varepsilon)}\right\} , \tag{A.20}$$

where $C > 0$ is the dimensionless constant we introduce in Eq. A.9. If the update is accepted, the new configuration is in the G-sector: the particle index of the worm is $i_W = i_p$ and we need to update the coordinate of the head $\mathbf{r}_{i_W,M+1}$. If the update is rejected, the system stays in the Z-sector and there is no need to specify the additional coordinate of the head of the worm. A schematic representation of the update is shown in Fig. A.3.

- **Close**: this update close an open polymer, allowing the configuration to switch from the G to the Z-sector. Thus, it can be performed only if the system is in the G-sector. We select randomly an integer l, with $1 \leq l \leq l_{max}$ which represents the length, in number of beads, of the segment of the polymer we reconstruct in this update. The parameter $l_{max} < M$ is chosen as input and has to be equal to the same parameter l_{max} used for the Open update. The

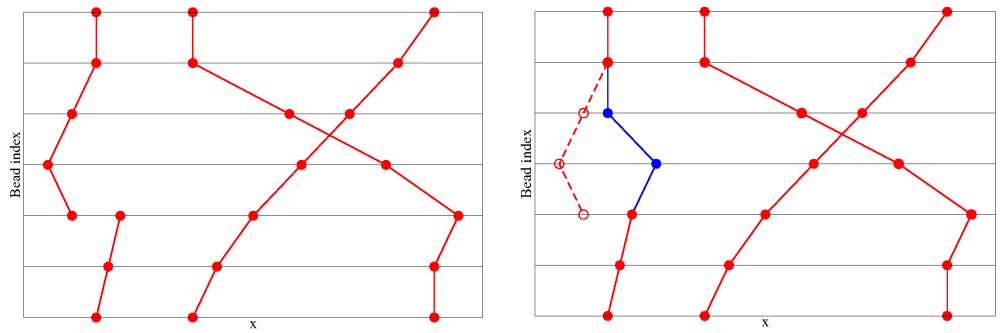

Figure A.4: Schematic representation of the Close update. On the left, we show the initial configuration of a one-dimensional system of three quantum particles, plotting on the x axis the coordinate of the bead and on the y axis the bead index. On the right we show the configuration after the update: the dashed lines represent the previous configuration and the blue lines and symbols highlights the position of the beads moved in the update.e

update consists in a reconstruction with the staging algorithm of the segment of the worm between the fixed point $\mathbf{r}_{i_W,M-l+1}$ and the tail of the worm $\mathbf{r}_{p(i_W),1}$. Once we have generated the new free particle path, we accept the update with probability

$$P_{close} = \min\left\{1; \frac{1}{C}\exp\left[\sum_{j=M-l+1}^{M} U(\mathbf{R}_{j+1},\mathbf{R}_j;\varepsilon) - U(\mathbf{R}'_{j+1},\mathbf{R}'_j;\varepsilon)\right]\times \right. \\ \left. \times\rho_{Fsp}(\mathbf{r}_{p(i_W),1},\mathbf{r}_{i_W,M-l+1};l\varepsilon)\right\}\ , \tag{A.21}$$

where $C > 0$ is the dimensionless constant appearing in Eq. A.9. If the update is accepted, the head of the worm is connected to the tail: thus the worm becomes a closed polymer and disappears, making the configuration of the system diagonal.

From the definition of the acceptance probability P_{open} (Eq. A.20) and P_{close} (Eq. A.21), respectively of the Open and of the Close updates, it is clear how the parameter C controls the relative frequencies of the Z and of the G-sector, as we already said in Sec. A.1. A larger C increase the probability of accepting the update Open and decreases the probability of accepting the update Close, making the system spending more time in the G than in Z-sector. Even if the results are independent of C for sufficiently long simulations, it might be important to control the relative frequency of diagonal and off-diagonal configurations with the parameter C in order to improve the efficiency of the sampling.

A schematic representation of the update is shown in Fig. A.4.

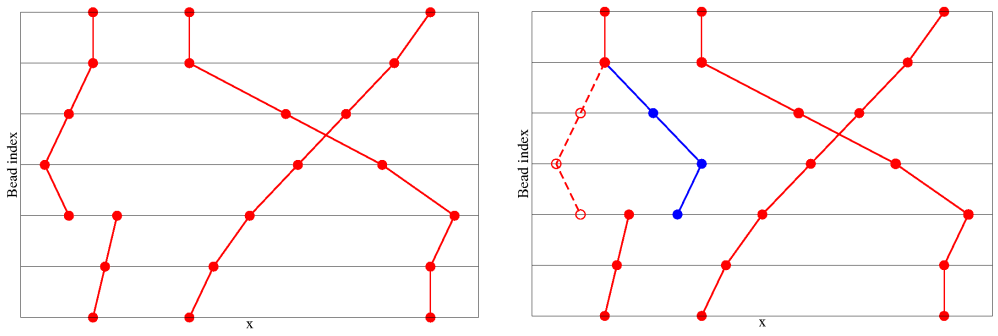

Figure A.5: Schematic representation of the Movehead update. On the left, we show the initial configuration of a one-dimensional system of three quantum particles, plotting on the x axis the coordinate of the bead and on the y axis the bead index. On the right we show the configuration after the update: the dashed lines represent the previous configuration and the blue lines and symbols highlights the position of the beads moved in the update.

- **Movehead and Movetail**: this updates move the beads close to the extremities of the worm and can be performed only when the system in the G-sector (here we describe just one of the two, that is Movehead: the update Movetail if formally equivalent). We select randomly an integer l, with $1 \leq l \leq l_{max}$ which represents the length, in number of beads, of the segment of the polymer we reconstruct in this update. The parameter $l_{max} < M$ is chosen as input in order to optimize the sampling efficiency. We sample a point $\mathbf{r}'_{i_p,M+1}$ according to a single particle free propagator on imaginary time $l\varepsilon$ staring on the point $\mathbf{r}_{i_p,M-l+1}$:

$$\rho_{Fsp}(\mathbf{r}'_{i_W,M+1}, \mathbf{r}_{i_W,M-l+1}; l\varepsilon) = \sqrt{\frac{m}{2\pi\hbar^2 l\varepsilon}} \exp\left[-\frac{m}{2\hbar^2 l\varepsilon}(\mathbf{r}'_{i_W,M+1} - \mathbf{r}_{i_W,M-l+1})^2\right] \quad . \tag{A.22}$$

  This point $\mathbf{r}'_{i_W,M+1}$ represent the proposal for the new head of the worm. Once we have sampled $\mathbf{r}'_{i_W,M+1}$, we reconstruct with the staging algorithm a free particle path from the first fixed point $\mathbf{r}_{i_W,M-l+1}$ and the new head $\mathbf{r}'_{i_W,M+1}$. At this point, we accept the update with probability

$$P_{move} = \min\left\{1; \exp\left[\sum_{j=M-l+1}^{M+1} U(\mathbf{R}_{j+1}, \mathbf{R}_j; \varepsilon) - U(\mathbf{R}'_{j+1}, \mathbf{R}'_j; \varepsilon)\right]\right\} \quad . \tag{A.23}$$

  A schematic representation of the update is shown in Fig. A.5.

- **Swap**: this update performs the permutations between the identical particles connecting beads belonging to different polymers. It requires the presence of the worm and therefore can be performed only in off-diagonal configurations.

We select randomly an integer l, with $1 \leq l \leq l_{max}$ which represents the length, in number of beads, of the segment of the polymer we reconstruct in this update. The parameter $l_{max} < M$ is chosen as input in order to optimize the sampling efficiency.
For every particle i_a, we compute the quantities

$$\begin{aligned} \Pi_p(i_a) &= \rho_{Fsp}(\mathbf{r}_{i_a,l+1}, \mathbf{r}_{i_W,M+1}; l\varepsilon) = \\ &= \sqrt{\frac{m}{2\pi\hbar^2 l\varepsilon}} \exp\left[-\frac{m}{2\hbar^2 l\varepsilon}(\mathbf{r}_{i_a,l+1} - \mathbf{r}_{i_W,M+1})^2\right] \end{aligned} \tag{A.24}$$

and

$$\Sigma_W = \sum_{i_a=1}^{N} \Pi_p(i_a) \tag{A.25}$$

Among all the particles, we select a particle i_K with probability $\Pi_p(i_K)/\Sigma_W$. The particle i_K represents the partner of the worm in the exchange process and the main idea of the update is to construct a free particle path from the head of the worm $\mathbf{r}_{i_W,M+1}$ and the bead $\mathbf{r}_{i_K,l+1}$ belonging to the partner polymer i_K. Nevertheless, before proceeding in the reconstruction, we have to perform two tests on the particle i_K.
At first, it is important that $i_K \neq p(i_W)$, otherwise the reconstruction of the path between $\mathbf{r}_{i_W,M+1}$ and $\mathbf{r}_{i_K,l+1}$ would lead to a situation where the worm would close on itself and therefore the configuration would change from an off-diagonal to a diagonal one. Such a movement is forbidden since the Swap update has to work only in the G-sector. Therefore, immediately after the random choice of the particle i_K we perform the first test: if $i_K = p(i_W)$ the update is rejected. Otherwise, we can proceed.
The second test has to be performed in order to ensure the detailed balance. Indeed the probability of choosing i_K as a partner of the exchange when the worm is i_W is not equal to the probability of choosing i_W as a partner of the exchange when the worm is i_K. Indeed, if in the first case the normalization factor of the probability table is Σ_W given in Eq. A.25, while in the second case the normalization factor of the probability table is

$$\Sigma_K = \sum_{i_a=1}^{N} \rho_{Fsp}(\mathbf{r}_{i_a,l+1}, \mathbf{r}_{i_K,1}; l\varepsilon) \ . \tag{A.26}$$

Therefore, to assure the detailed balance it is necessary to perform a second test: we accept the choice of i_K with probability

$$P_{swap1} = \min\left\{1; \frac{\Sigma_W}{\Sigma_K}\right\} \ . \tag{A.27}$$

If this test give a negative result, the whole update is rejected and the system is left in its initial configuration.
If the choice of the partner i_K has been accepted in the first two tests, we

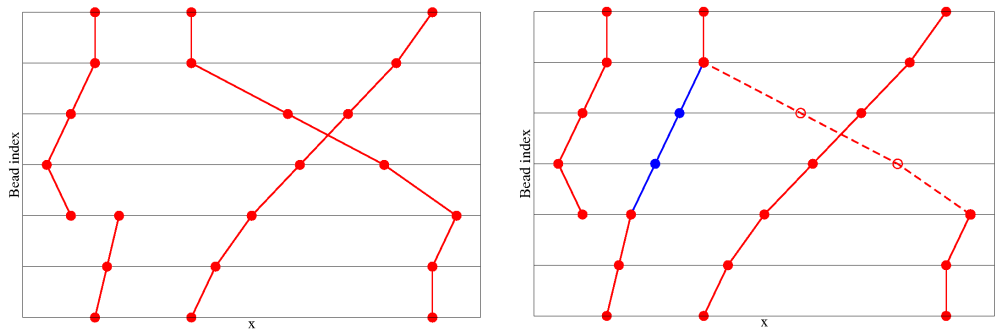

Figure A.6: Schematic representation of the Swap update. On the left, we show the initial configuration of a one-dimensional system of three quantum particles, plotting on the x axis the coordinate of the bead and on the y axis the bead index. On the right we show the configuration after the update: the dashed lines represent the previous configuration and the blue lines and symbols highlights the position of the beads moved in the update.

can proceed and reconstruct the free particle path $\{\mathbf{r}_{i_K,2}\ldots,\mathbf{r}_{i_K,l}\}$ between $\mathbf{r}_{i_W,M+1}$ and $\mathbf{r}_{i_K,l+1}$ by means of the staging algorithm and finally evaluate the change in the potential action as to perform the last test on the new configuration

$$P_{swap2} = \min\left\{1; \exp\left[\sum_{j=1}^{l+1} U(\mathbf{R}_{j+1},\mathbf{R}_j;\varepsilon) - U(\mathbf{R}'_{j+1},\mathbf{R}'_j;\varepsilon)\right]\right\} . \quad \text{(A.28)}$$

If the update is accepted, the final configuration is still off-diagonal but presents some different characteristics from the initial one. At first, the new configuration the head of the worm is no more in position $\mathbf{r}_{i_W,M+1}$ but has moved to the new position $\mathbf{r}_{i_k,1}$. Secondly, the swap update modify the permutation table: indeed, if we define i_A and i_T in order to have before the swap $p(i_W) = i_T$ and $p(i_A) = i_K$, when the update is accepted we will have $p(i_A) = i_T$ and $p(i_W) = i_K$.
As a final consideration, it is worth to notice that swap is a single particle update, in the sense that it redraws a segment of a single polymer. Although, sequences of swap updates can form cyclic permutations of macroscopic size and perform an ergodic and detailed balanced random walk in the space of permutations. A schematic representation of the update is shown in Fig. A.6

The updates we just described can be combined with a certain freedom in order to provide a suitable sampling scheme, according to the simulated system. In our simulation, the typical scheme of a given Monte Carlo step is the one presented in the following box, according to the formalism of Fortran programming language.

```
if (mod(iMCstep,nfreqCM).eq.0) then
   do ia = 1,Natoms
     CALL TRANSLATE(ia)
   enddo
endif
do irep = 1,Nrepstag
   do ia = 1,Natoms
     CALL STAGING(ia)
   enddo
enddo

iupdate = INT(random()*2)
if (iupdate.eq.0) then
   if (i_w.eq.0) then
     CALL OPEN
   endif
else
   if (i_w.ne.0) then
     CALL CLOSE
   endif
endif

if (i_W.ne.0) then
   do irep = 1,Nrepoffdiag
     CALL MOVEHEAD
     CALL MOVETAIL
     CALL SWAP
   enddo
endif

if (i_W.eq.0) then
   CALL compute_diagonal
else
   CALL compute_offdiagonal
endif
```

In the sampling of the coordinates, we can distinguish three parts, according to the three groups in which we divided the updates at the beginning of the section. In the first part of the sampling, we perform the Translate and the Staging updates. In a single step we propose a Translate and a Staging movement for every particle of the system, as indicated by the cycle on the parameter ia which change from 1 to the total number of particles Natoms.

The Translate update, which is the most onerous from the computational point of view, is not performed at every Monte Carlo step, but only once in every nfreqCM

steps. In our simulations, the parameter nfreqCM varies between 20 and 100. The suitable value for nfreqCM is chosen according the details of the simulation. In the simulation of a liquid phase, where it is important to take into account the diffusion of the particles, and of systems with a small number of particles ($N < 100$), for which the computational cost of the Translate update is not too onerous, it is preferable to perform the Translate movement with a higher frequency and therefore choosing a small nfreqCM. On the contrary, in the simulation of crystalline states with a high number of atoms, it is better to choose a higher value for nfreqCM.

On the contrary, it is preferable to perform the Staging update more than once at every Monte Carlo steps, especially when simulating systems at a low temperature. Indeed, the length l_s in number of beads of the portion of the chain rebuilt at every Staging update is limited (in a typical PIMC simulation with the Chin approximation for the thermal density matrix, it is not possible to perform a good sampling choosing l_s larger than 10). Therefore, if the polymer is made up of a big number of beads ($M > 50$), the fraction of the polymers which is modified at every step can be small. To overcome this problem, it is good to perform the Staging update Nrepstag times at every step: typically we vary Nrepstag from 1, in the simulations at high temperature, to 12, in the simulation at low temperature.

In the second part of the sampling, we propose a movement to switch the configuration from Z to G-sector or vice versa, calling the updates Open or Close. These two updates form a complementary pair. According to the theory of random walks in spaces with different dimensionality, such as the Z and the G-sector in the WA, a detailed balanced sampling can be provided only by means of coupled updates which are called with the same probability and without a predetermined order [138]. In order to accomplish this requirement, it is important, at every MC step, to select *at random* which of the two updates, Open or Close, has to be proposed, regardless of the configuration of the system at the moment of the random choice. If the update selected cannot be performed since the configuration is not in the correct sector (that is if we choose to apply Close to a diagonal configuration or Open to an off-diagonal one), we simply reject the move and leave the system in its initial configuration.

In our scheme, we choose which update has to be proposed using the integer iupdate, which is a random variable which can assume the value 0 or 1. We propose the Open update if iupdate is equal to 0 and the system is in a diagonal configuration (if the system is in the Z-sector, the parameter i_W which indicates the particle index of the worm is 0). We propose the Close update if iupdate is equal to 1 and the system is in an off-diagonal configuration. Notice that our sampling scheme does not perform any update if iupdate is equal to 0 the system is in an off-diagonal configuration or if iupdate is equal to 1 the system is in a diagonal configuration.

In the third part of the sampling, we perform the updates Movehead, Movetail and Swap. Notice that these update can be performed only if the system is in an off-diagonal configuration. Therefore, before proposing any movement, we have to control the parameter i_W to discriminate if the configuration is in the Z or in the G-sector. It can be useful, especially in system where the Swap update has a small

acceptance rate, to perform these updates Nrepoffdiag times at every Monte Carlo step. Our typical choice of Nrepoffdiag is 20.

Once the sampling of the coordinates is accomplished, in the last part of the Monte Carlo step, we estimate the physical observables. Notice that, before calculating any quantity, it is necessary to perform the control on the parameter i_W to discriminate if the system is in the Z or in the G-sector: in the first case, we calculate the diagonal observables (energy, pair distribution function, static structure factor and superfluid density), in the second case we calculate the off-diagonal observables (one-body density matrix).

A.3 Normalization of the one-body density matrix

The one-body density matrix

$$\rho_1(r) = \frac{1}{\rho Z} \int dX_G \, \delta(r - |\mathbf{r}_{i_W,M+1} - \mathbf{r}_{p(i_W),1}|) \prod_{j=1}^{M} \rho_F(\mathbf{R}_{j+1}, \mathbf{R}_j; \varepsilon) e^{-U(\mathbf{R}_{j+1}, \mathbf{R}_j; \varepsilon)} \, , \tag{A.29}$$

where $dX_G = d\mathbf{R}_1 \ldots d\mathbf{R}_M d\mathbf{r}_{i_W,M+1}$ and ρ is the density of the system, is a fundamental quantity since from its asymptotic behavior it is possible to get an estimation of the condensate fraction n_0. From its definition, it is easy to realize that it satisfies the normalization condition $\rho_1(0) = 1$.

In subsec. 2.5.4 we discussed the PIMC estimator for $\rho_1(r)$, seeing that, to evaluate $\rho_1(r)$ for a fixed r, it is necessary to evaluate the number $N(r)$ of off-diagonal configurations in which the two extremities of the worm are separated by a distance $r_{HT} = |\mathbf{r}_{i_W,M+1} - \mathbf{r}_{p(i_W),1}|$, with $r - \Delta r/2 < r_{HT} < r + \Delta r/2$, Δr being a small distance fixed as input of the simulation.

For a number N_G of off-diagonal configurations sufficiently large to get a good statistic, we can write

$$\frac{N(r)}{N_G V_{sh}(r)} = \int dX_G \, \delta(r - r_{HT}) \, p_G(X_G) \, . \tag{A.30}$$

with $p_G(X_G)$ defined in Eq. A.6 and $V_{sh}(r) = 4\pi[(r + \Delta r/2)^3 - (r - \Delta r/2)^3]/3$ the volume of the spherical shell corresponding to the possible values of r_{HT} at the fixed r. Comparing the integral in Eq. A.29 with Eq. A.30, we can easily realize that

$$\rho_1(r) = \frac{1}{\rho Z} \frac{N(r) Z_G}{N_G V_{sh}(r)} \tag{A.31}$$

The WA, being able to sample both diagonal and off-diagonal configuration, is able to give an estimation of the ratio Z_G/Z, as we saw in Eq. A.12. This important feature makes possible the computation of an automatically normalized one-body density matrix, by means of the formula

$$\rho_1(r) = \frac{1}{\rho C N_Z V_{sh}(r)} N(r) \, . \tag{A.32}$$

Appendix B

The virial estimator of the energy

In this appendix, we provide the whole derivation of the virial estimator of the energy per particle. Here, we consider the general case of arbitrary actions, periodic boundary conditions and particle exchange. The formalism and the definitions used in this appendix are the same as in Chap 2.

Let us recall the definition of the thermal density matrix with L links

$$\begin{aligned}\rho(\mathbf{R}_{j+L},\mathbf{R}_j;L\varepsilon) &= \int\prod_{k=1}^{L-1} d\mathbf{R}_{j+k}\,\rho(\mathbf{R}_{j+k},\mathbf{R}_{j+k-1};\varepsilon) = \\ &= \int\prod_{k=1}^{L-1} d\mathbf{R}_{j+k}\,\frac{1}{(4\pi\lambda\varepsilon)^{3N/2}}\,\exp\left(-S(\mathbf{R}_{j+k},\mathbf{R}_{j+k-1};\varepsilon)\right)\ ,\end{aligned} \tag{B.1}$$

where the total action

$$S(\mathbf{R}_{j+1},\mathbf{R}_j;\varepsilon) = \frac{1}{4\lambda\varepsilon}(\mathbf{R}_{j+1}-\mathbf{R}_j)^2 + U(\mathbf{R}_{j+1},\mathbf{R}_j;\varepsilon) \tag{B.2}$$

is split into two terms: a kinetic contribution, which is independent on the approximation scheme, and a potential term $U(\mathbf{R}_{j+1},\mathbf{R}_j;\varepsilon)$ which depends on the approximation used in the simulation.

From the definition of the partition function

$$Z = \int d\mathbf{R}\,\rho(\mathbf{R},\mathbf{R};\beta) = \int\prod_{j=1}^{M} d\mathbf{R}_j\,\frac{1}{(4\pi\lambda\varepsilon)^{3N/2}}\,\exp\left(-S(\mathbf{R}_{j+1},\mathbf{R}_j;\varepsilon)\right)\ , \tag{B.3}$$

we recover the thermodynamic estimator of the total energy

$$\begin{aligned}\frac{E_T}{N} &= -\frac{1}{NZ}\frac{\partial Z}{\partial\beta} = \\ &= \left\langle\frac{3M}{2\beta} - \frac{M}{4\lambda\beta^2 N}\sum_{j=1}^{M}(\mathbf{R}_{j+1}-\mathbf{R}_j)^2 + \frac{1}{M}\sum_{j=1}^{M}\frac{\partial U(\mathbf{R}_{j+1},\mathbf{R}_j;\varepsilon)}{\partial\varepsilon}\right\rangle\end{aligned} \tag{B.4}$$

The main problem with this estimator is that it behaves poorly at large M. Indeed, when M increases, the first two terms of the sum increase and we have to evaluate a small difference between two large quantities, reducing thus the efficiency of this estimator. We need therefore to rewrite the whole expression in order to eliminate the highly fluctuating terms.

Let us consider the quantity

$$\begin{aligned} E_{1;L+1} &= -\frac{1}{\rho(\mathbf{R}_{L+1},\mathbf{R}_1;L\varepsilon)}\frac{\partial\rho(\mathbf{R}_1,\mathbf{R}_{L+1};L\varepsilon)}{\partial\varepsilon} = \\ &= \frac{1}{\rho(\mathbf{R}_{L+1},\mathbf{R}_1;L\varepsilon)}\int d\mathbf{R}_2\ldots d\mathbf{R}_L\,\rho(\mathbf{R}_{L+1},\mathbf{R}_L;\varepsilon)\ldots\rho(\mathbf{R}_2,\mathbf{R}_1;\varepsilon)\times \\ &\quad\times\left[\frac{3NL}{2\varepsilon}-\frac{1}{4\lambda\varepsilon^2}\sum_{l=1}^{L}(\mathbf{R}_{l+1}-\mathbf{R}_l)^2+\sum_{l=1}^{L}\frac{\partial U(\mathbf{R}_{l+1},\mathbf{R}_l;\varepsilon)}{\partial\varepsilon}\right], \end{aligned} \tag{B.5}$$

with $1\le L\le M$: an estimator of the total energy of the system can be recovered integrating $E_{1;L+1}/L$ over the coordinates $\mathbf{R}_1$ and $\mathbf{R}_{L+1}$.

To rewrite the expression of $E_{1;L+1}$, we make use of the following quantity:

$$G=-\frac{1}{\rho(\mathbf{R}_{L+1},\mathbf{R}_1;L\varepsilon)}\int d\mathbf{R}_2\ldots d\mathbf{R}_L\,\frac{1}{\varepsilon}\sum_{l=2}^{L}(\mathbf{R}_l-\mathbf{R}_1)\frac{\partial}{\partial\mathbf{R}_l}e^{-\sum_{j=1}^{L}S(\mathbf{R}_{j+1},\mathbf{R}_j;\varepsilon)}. \tag{B.6}$$

The integral in the definition of G can be computed in two ways: computing directly the derivative appearing inside the integral or integrating by parts.

Let us consider the first way and compute

$$\begin{aligned} \frac{\partial}{\partial\mathbf{R}_l}e^{-\sum_{j=1}^{L}S(\mathbf{R}_{j+1},\mathbf{R}_j;\varepsilon)} &= \exp\left(-\sum_{j=1}^{L}S(\mathbf{R}_{j+1},\mathbf{R}_j;\varepsilon)\right)\times \\ &\times\left[\frac{1}{2\lambda\varepsilon}(\mathbf{R}_l-\mathbf{R}_{l+1})+\frac{\partial U(\mathbf{R}_{l+1},\mathbf{R}_l;\varepsilon)}{\partial\mathbf{R}_l}+\right. \\ &\left.+\frac{1}{2\lambda\varepsilon}(\mathbf{R}_l-\mathbf{R}_{l-1})+\frac{\partial U(\mathbf{R}_l,\mathbf{R}_{l-1};\varepsilon)}{\partial\mathbf{R}_l}\right]. \end{aligned} \tag{B.7}$$

It follows that

$$\begin{aligned} G &= \frac{1}{\rho(\mathbf{R}_{L+1},\mathbf{R}_1;L\varepsilon)}\int d\mathbf{R}_2\ldots d\mathbf{R}_L\,e^{-\sum_{j=1}^{L}S(\mathbf{R}_{j+1},\mathbf{R}_j;\varepsilon)}\times \\ &\times\sum_{l=2}^{L}(\mathbf{R}_l-\mathbf{R}_1)\left[\frac{1}{2\lambda\varepsilon^2}[(\mathbf{R}_l-\mathbf{R}_{l+1})+(\mathbf{R}_l-\mathbf{R}_{l-1})]+\frac{\partial\gamma_l}{\partial\mathbf{R}_l}\right], \end{aligned} \tag{B.8}$$

where we have use the definition $\gamma_l=(U(\mathbf{R}_{l+1},\mathbf{R}_l;\varepsilon)+U(\mathbf{R}_l,\mathbf{R}_{l-1};\varepsilon))/\varepsilon$.

Let us now consider the term

$$\alpha=\sum_{l=2}^{L}(\mathbf{R}_l-\mathbf{R}_1)[(\mathbf{R}_l-\mathbf{R}_{l+1})+(\mathbf{R}_l-\mathbf{R}_{l-1})]. \tag{B.9}$$

Expanding the terms in the sum, we have

$$\begin{aligned} \alpha &= (\mathbf{R}_2-\mathbf{R}_1)[(\mathbf{R}_2-\mathbf{R}_1)+(\mathbf{R}_2-\mathbf{R}_3)]+ \\ &+(\mathbf{R}_3-\mathbf{R}_1)[(\mathbf{R}_3-\mathbf{R}_2)+(\mathbf{R}_3-\mathbf{R}_4)]+ \\ &+\ldots+(\mathbf{R}_L-\mathbf{R}_1)[(\mathbf{R}_L-\mathbf{R}_{L-1})+(\mathbf{R}_L-\mathbf{R}_{L+1})]. \end{aligned} \tag{B.10}$$

If we collect all the terms multiplied by $\mathbf{R}_1$, we have

$$\begin{aligned}
\alpha &= -\mathbf{R}_1[(\mathbf{R}_2-\mathbf{R}_1)+\cancel{(\mathbf{R}_2-\mathbf{R}_3)}+\cancel{(\mathbf{R}_3-\mathbf{R}_2)}+\cancel{(\mathbf{R}_3-\mathbf{R}_4)}+ \\
&\quad +\ldots+\cancel{(\mathbf{R}_L-\mathbf{R}_{L-1})}+(\mathbf{R}_L-\mathbf{R}_{L+1})]+ \\
&\quad +\mathbf{R}_2(\mathbf{R}_2-\mathbf{R}_1)+\mathbf{R}_2(\mathbf{R}_2-\mathbf{R}_3)+ \\
&\quad +\mathbf{R}_3(\mathbf{R}_3-\mathbf{R}_2)+\mathbf{R}_3(\mathbf{R}_3-\mathbf{R}_4)+ \\
&\quad +\ldots+\mathbf{R}_L(\mathbf{R}_L-\mathbf{R}_{L-1})+\mathbf{R}_L(\mathbf{R}_L-\mathbf{R}_{L+1})= \\
&= (\mathbf{R}_2-\mathbf{R}_1)^2+(\mathbf{R}_3-\mathbf{R}_2)^2+\ldots+(\mathbf{R}_L-\mathbf{R}_{L-1})^2+ \\
&\quad +(\mathbf{R}_L-\mathbf{R}_1)(\mathbf{R}_L-\mathbf{R}_{L+1})\ . \qquad \text{(B.11)}
\end{aligned}$$

If we add and subtract $\mathbf{R}_{L+1}$ in the last term in the sum, we get

$$\begin{aligned}
\alpha &= (\mathbf{R}_2-\mathbf{R}_1)^2+(\mathbf{R}_3-\mathbf{R}_2)^2+\ldots+(\mathbf{R}_L-\mathbf{R}_{L-1})^2+ \\
&\quad +(\mathbf{R}_L-\mathbf{R}_{L+1}+\mathbf{R}_{L+1}-\mathbf{R}_1)(\mathbf{R}_L-\mathbf{R}_{L+1})= \\
&= (\mathbf{R}_2-\mathbf{R}_1)^2+\ldots+(\mathbf{R}_L-\mathbf{R}_{L-1})^2+(\mathbf{R}_{L+1}-\mathbf{R}_L)^2+ \\
&\quad +(\mathbf{R}_{L+1}-\mathbf{R}_1)(\mathbf{R}_L-\mathbf{R}_{L+1})= \\
&= \sum_{l=1}^{L}(\mathbf{R}_{l+1}-\mathbf{R}_l)^2+(\mathbf{R}_{L+1}-\mathbf{R}_1)(\mathbf{R}_L-\mathbf{R}_{L+1})\ . \qquad \text{(B.12)}
\end{aligned}$$

Putting the result for α in the expression for G, Eq. B.8, we get:

$$\begin{aligned}
G &= \frac{1}{\rho(\mathbf{R}_{L+1},\mathbf{R}_1;L\varepsilon)}\int d\mathbf{R}_2\ldots d\mathbf{R}_L\, e^{-\sum_{j=1}^{L}S(\mathbf{R}_{j+1},\mathbf{R}_j;\varepsilon)}\times \\
&\quad \times\left[\frac{1}{2\lambda\varepsilon^2}\sum_{l=1}^{L}(\mathbf{R}_{l+1}-\mathbf{R}_l)^2+\frac{1}{2\lambda\varepsilon^2}(\mathbf{R}_{L+1}-\mathbf{R}_1)(\mathbf{R}_L-\mathbf{R}_{L+1})+\right. \\
&\quad \left.+\sum_{l=1}^{L}(\mathbf{R}_l-\mathbf{R}_1)\frac{\partial\gamma_l}{\partial\mathbf{R}_l}\right]\ . \qquad \text{(B.13)}
\end{aligned}$$

Let us now consider the second way to compute G, that is integrating by parts the integral in Eq. B.6. Considered that the surface term vanishes provided that $\varepsilon\lambda \ll V^{2/3}$ (that is true for sufficiently small time step), we obtain

$$\begin{aligned}
G &= \frac{1}{\rho(\mathbf{R}_{L+1},\mathbf{R}_1;L\varepsilon)}\int d\mathbf{R}_2\ldots d\mathbf{R}_L\,\frac{1}{\varepsilon}\sum_{l=2}^{L}\underbrace{\frac{\partial(\mathbf{R}_l-\mathbf{R}_1)}{\partial\mathbf{R}_l}}_{3N}\,e^{-\sum_{j=1}^{L}S(\mathbf{R}_{j+1},\mathbf{R}_j;\varepsilon)} \\
&= \frac{3N(L-1)}{\varepsilon\,\cancel{\rho(\mathbf{R}_{L+1},\mathbf{R}_1;L\varepsilon)}}\cancel{\int d\mathbf{R}_2\ldots d\mathbf{R}_L\,e^{-\sum_{j=1}^{L}S(\mathbf{R}_{j+1},\mathbf{R}_j;\varepsilon)}} \\
&= \frac{3N(L-1)}{\varepsilon}\ . \qquad \text{(B.14)}
\end{aligned}$$

Equalizing the two results for G, Eq. B.13 and Eq. B.14,

$$\begin{aligned}\frac{3N(L-1)}{\varepsilon} &= \frac{1}{\rho(\mathbf{R}_{L+1},\mathbf{R}_1;L\varepsilon)}\int d\mathbf{R}_2\ldots d\mathbf{R}_L e^{-\sum_{j=1}^{L}S(\mathbf{R}_{j+1},\mathbf{R}_j;\varepsilon)}\times \\ &\times\left[\frac{1}{2\lambda\varepsilon^2}\sum_{l=1}^{L}(\mathbf{R}_{l+1}-\mathbf{R}_l)^2+\frac{1}{2\lambda\varepsilon^2}(\mathbf{R}_{L+1}-\mathbf{R}_1)(\mathbf{R}_L-\mathbf{R}_{L+1})+\right. \\ &\left.+\sum_{l=1}^{L}(\mathbf{R}_l-\mathbf{R}_1)\frac{\partial\gamma_l}{\partial\mathbf{R}_l}\right]\ . \end{aligned} \tag{B.15}$$

From the last equation, it is better to separate the term

$$\begin{aligned}&\frac{1}{\rho(\mathbf{R}_{L+1},\mathbf{R}_1;L\varepsilon)}\int d\mathbf{R}_2\ldots d\mathbf{R}_L\, e^{-\sum_{j=1}^{L}S(\mathbf{R}_{j+1},\mathbf{R}_j;\varepsilon)}\frac{1}{2\lambda\varepsilon^2}\sum_{l=1}^{L}(\mathbf{R}_{l+1}-\mathbf{R}_l)^2 = \\ =\ &\frac{3N(L-1)}{\varepsilon}-\frac{1}{\rho(\mathbf{R}_{L+1},\mathbf{R}_1;L\varepsilon)}\int d\mathbf{R}_2\ldots d\mathbf{R}_L\, e^{-\sum_{j=1}^{L}S(\mathbf{R}_{j+1},\mathbf{R}_j;\varepsilon)}\times \\ &\times\left[\frac{1}{2\lambda\varepsilon^2}(\mathbf{R}_{L+1}-\mathbf{R}_1)(\mathbf{R}_L-\mathbf{R}_{L+1})+\sum_{l=1}^{L}(\mathbf{R}_l-\mathbf{R}_1)\frac{\partial\gamma_l}{\partial\mathbf{R}_l}\right]\ . \end{aligned} \tag{B.16}$$

Indeed, this term, a part for a multiplicative factor, appears also in the definition of $E_{1;L+1}$, Eq. B.5:

$$\begin{aligned}&\frac{1}{\rho(\mathbf{R}_{L+1},\mathbf{R}_1;L\varepsilon)}\int d\mathbf{R}_2\ldots d\mathbf{R}_L\, e^{-\sum_{j=1}^{L}S(\mathbf{R}_{j+1},\mathbf{R}_j;\varepsilon)}\frac{1}{4\lambda\varepsilon^2}\sum_{l=1}^{L}(\mathbf{R}_{l+1}-\mathbf{R}_l)^2 = \\ =\ &-E_{1;L+1}+\frac{3NL}{2\varepsilon}+\frac{1}{\rho(\mathbf{R}_{L+1},\mathbf{R}_1;L\varepsilon)}\int d\mathbf{R}_2\ldots d\mathbf{R}_L\, e^{-\sum_{j=1}^{L}S(\mathbf{R}_{j+1},\mathbf{R}_j;\varepsilon)}\times \\ &\times\sum_{l=1}^{L}\frac{\partial U(\mathbf{R}_{l+1},\mathbf{R}_l;\varepsilon)}{\partial\varepsilon}\ . \end{aligned} \tag{B.17}$$

Multiplying Eq. B.16 by 1/2 and equalizing it to B.17, we get

$$\begin{aligned}&\frac{3N(L-1)}{2\varepsilon}-\frac{1}{\rho(\mathbf{R}_{L+1},\mathbf{R}_1;L\varepsilon)}\int d\mathbf{R}_2\ldots d\mathbf{R}_L e^{-\sum_{j=1}^{L}S(\mathbf{R}_{j+1},\mathbf{R}_j;\varepsilon)}\times \\ &\times\left[\frac{1}{4\lambda\varepsilon^2}(\mathbf{R}_{L+1}-\mathbf{R}_1)(\mathbf{R}_L-\mathbf{R}_{L+1})+\frac{1}{2}\sum_{l=1}^{L}(\mathbf{R}_l-\mathbf{R}_1)\frac{\partial\gamma_l}{\partial\mathbf{R}_l}\right] = \\ =\ &-E_{1;L+1}+\cancel{\frac{3NL}{2\varepsilon}}+\frac{1}{\rho(\mathbf{R}_{L+1},\mathbf{R}_1;L\varepsilon)}\int d\mathbf{R}_2\ldots d\mathbf{R}_L e^{-\sum_{j=1}^{L}S(\mathbf{R}_{j+1},\mathbf{R}_j;\varepsilon)}\times \\ &\times\sum_{l=1}^{L}\frac{\partial U(\mathbf{R}_{l+1},\mathbf{R}_l;\varepsilon)}{\partial\varepsilon}\ , \end{aligned} \tag{B.18}$$

that is

$$E_{1;L+1} = \frac{3N}{2\varepsilon} + \frac{1}{\rho(\mathbf{R}_{L+1}, \mathbf{R}_1; L\varepsilon)} \int d\mathbf{R}_2 \dots d\mathbf{R}_L e^{-\sum_{j=1}^{L} S(\mathbf{R}_{j+1}, \mathbf{R}_j; \varepsilon)} \times$$
$$\times \left[\frac{(\mathbf{R}_{L+1} - \mathbf{R}_1)(\mathbf{R}_L - \mathbf{R}_{L+1})}{4\lambda\varepsilon^2} + \sum_{l=1}^{L} \left(\frac{\partial U(\mathbf{R}_{l+1}, \mathbf{R}_l; \varepsilon)}{\partial \varepsilon} + (\mathbf{R}_l - \mathbf{R}_1) \frac{\partial \gamma_l}{\partial \mathbf{R}_l} \right) \right] . \tag{B.19}$$

We have thus deduced a new estimator for the total energy per particle:

$$\begin{aligned} \frac{E_L}{N} &= \frac{1}{NL} \int d\mathbf{R}_1 d\mathbf{R}_{L+1} \, E_{1;L+1} = \\ &= \left\langle \frac{3}{2L\varepsilon} + \frac{(\mathbf{R}_{L+1} - \mathbf{R}_1)(\mathbf{R}_L - \mathbf{R}_{L+1})}{4\lambda\varepsilon^2 LN} + \frac{1}{NL} \sum_{l=1}^{L} \frac{\partial U(\mathbf{R}_{l+1}, \mathbf{R}_l; \varepsilon)}{\partial \varepsilon} + \right. \\ &\quad \left. + \frac{1}{NL\varepsilon} \sum_{l=1}^{L} (\mathbf{R}_l - \mathbf{R}_1) \frac{\partial}{\partial \mathbf{R}_l} (U(\mathbf{R}_{l+1}, \mathbf{R}_l; \varepsilon) + U(\mathbf{R}_l, \mathbf{R}_{l-1}; \varepsilon)) \right\rangle . \end{aligned} \tag{B.20}$$

We have to emphasize here the importance of introducing a reference configuration in the definition of G. Eq. B.6 (in our case we chose $\mathbf{R}_1$) to obtain the correct expression. A derivation without this reference configuration will lead to an expression which is ill defined with periodic boundary conditions or permutations. However the choice of this reference configuration, as well as the direction in imaginary time, is totally arbitrary; it is worth to average the result over the reference configuration and over the direction of time:

$$\begin{aligned} \frac{E_L}{N} &= \left\langle \frac{3}{2L\varepsilon} + \frac{1}{MLN} \sum_{j=1}^{M} \frac{(\mathbf{R}_{L+j} - \mathbf{R}_j)(\mathbf{R}_{L+j-1} - \mathbf{R}_{L+j})}{4\lambda\varepsilon^2} + \right. \\ &\quad + \frac{1}{2N\beta} \sum_{j=1}^{M} (\mathbf{R}_j - \mathbf{R}_j^C) \frac{\partial}{\partial \mathbf{R}_j} (U(\mathbf{R}_{j+1}, \mathbf{R}_j; \varepsilon) + U(\mathbf{R}_j, \mathbf{R}_{j-1}; \varepsilon)) + \\ &\quad \left. + \sum_{j=1}^{M} \frac{\partial U(\mathbf{R}_{j+1}, \mathbf{R}_j; \varepsilon)}{\partial \varepsilon} \right\rangle . \end{aligned} \tag{B.21}$$

where $\mathbf{R}_j^C = \frac{1}{2L} \sum_{l=0}^{L-1} (\mathbf{R}_{j+l} + \mathbf{R}_{j-l})$

The last formula represent an estimator for the energy for any value of L, with $1 \leq L \leq M$. For $L = 1$, indeed, we recover exactly the thermodynamic estimator, Eq. B.4. Nevertheless, increasing the number L, we reduce the fluctuations of the first two terms in the sum and, thus, the statistical error. The maximum value for L is equal to the number of beads M: putting $L = M$ in Eq. B.21 is the conventional choice, being the one which allow for the minimum statistical error.

We can, at this point, define the *virial estimator* for the total energy:

$$\begin{aligned}\frac{E_V}{N} &= \left\langle \frac{3}{2\beta} + \frac{1}{4\lambda N\beta^2}\sum_{j=1}^{M}(\mathbf{R}_{M+j}-\mathbf{R}_j)(\mathbf{R}_{M+j-1}-\mathbf{R}_{M+j})+\right.\\ &+\frac{1}{2N\beta}\sum_{j=1}^{M}(\mathbf{R}_j-\mathbf{R}_j^C)\frac{\partial}{\partial\mathbf{R}_j}(U(\mathbf{R}_{j+1},\mathbf{R}_j;\varepsilon)+U(\mathbf{R}_j,\mathbf{R}_{j-1};\varepsilon))+\\ &\left.+\sum_{j=1}^{M}\frac{\partial U(\mathbf{R}_{j+1},\mathbf{R}_j;\varepsilon)}{\partial\varepsilon}\right\rangle . \qquad \text{(B.22)}\end{aligned}$$

Let us conclude this appendix giving some interesting observations. Notice that the first term in Eq. B.22 represent the energy per particle of a classical ideal gas. Furthermore, if no particle exchanges are present in the system, the second term drops out, being $\mathbf{R}_{j+M} = \mathbf{R}_j$. For these reasons, the virial estimator is very effective at computing quantum corrections to a nearly classical system. Another important thing to notice is that in the computation of the distances in $\mathbf{R}_{j+M} - \mathbf{R}_j$ one has to follow a continuous path. Periodic boundary conditions must be applied between subsequent slices only: $\mathbf{R}_{j+M} - \mathbf{R}_j$ might therefore be larger than the size of the simulation box. For a detailed comparison between the different estimators of the total energy, we refer the readers to Ref. [18]

Bibliography

[1] J. F. Allen, *Nature*, **141**, 75 (1938).

[2] P. Kapitza, *Nature*, **141**, 74 (1938).

[3] H. Glyde, *Excitations in liquid and solid helium*, Oxford series on neutron scattering in condensed matter (Clarendon Press, 1994).

[4] J. Boronat and J. Casulleras, *Phys. Rev. B*, **49**, 8920 (1994).

[5] S. Moroni, G. Senatore and S. Fantoni, *Phys. Rev. B*, **55**, 1040 (1997).

[6] S. Moroni and M. Boninsegni, *J. Low Temp. Phys.*, **136**, 129 (2004).

[7] M. Boninsegni, N. V. Prokof'ev and B. V. Svistunov, *Phys. Rev. E*, **74**, 036701 (2006).

[8] V. L. Ginzburg and A. A. Sobyanin, *JEPT Lett.*, **15**, 242 (1972).

[9] M. Kühnel, J. M. Fernández, G. Tejeda, A. Kalinin, S. Montero and R. E. Grisenti, *Phys. Rev. Lett.*, **106**, 245301 (2011).

[10] S. Grebenev, B. Sartakov, J. P. Toennies and â. A. F. Vilesov, *Science*, **289**, 1532 (2000).

[11] O. Penrose and L. Onsager, *Phys. Rev.*, **104**, 576 (1956).

[12] A. F. Andreev and I. M. Lifshtiz, *Sov. Phys. JETP*, **29**, 1107 (1969).

[13] G. V. Chester, *Phys. Rev. A*, **2**, 256 (1970).

[14] E. Kim and M. H. W. Chan, *Nature*, **427**, 225 (2004).

[15] E. Kim and M. H. W. Chan, *Science*, **305**, 1941 (2004).

[16] W. L. McMillan, *Phys. Rev. A*, **138**, 442 (1965).

[17] B. L. Hammond, W. A. Lester and P. J. Reynolds, *Monte Carlo Methods in Ab Initio Quantum Chemistry* (World Scientific, 1994).

[18] D. M. Ceperley, *Rev. Mod. Phys.*, **67**, 279 (1995).

[19] S. A. Chin and C. R. Chen, *J. Chem. Phys*, **117**, 1409 (2002).

[20] K. Sakkos, J. Casulleras and J. Boronat, *J. Chem. Phys*, **130**, 204109 (2009).

[21] M. Boninsegni, N. Prokof'ev and B. Svistunov, *Phys. Rev. Lett.*, **96**, 070601 (2006).

[22] M. Kalos and P. Whitlock, *Monte Carlo methods* (Wiley, 1986).

[23] W. H. Press, B. P. Flannery, S. A. Teukolsky and W. T. Vetterling, *Numerical Recipes in Fortran 77: The Art of Scientific Computing* (Cambridge University Press, 1992).

[24] N. Metropolis, A. W. Rosenbluth, M. N. Rosenbluth, A. H. Teller and E. Teller, *J. Chem. Phys*, **21**, 1087 (1953).

[25] R. Feynman, *Statistical mechanics: a set of lectures*, Frontiers in physics (W. A. Benjamin, 1972).

[26] H. Trotter, *Proc. Am. Math.*, **10**, 545 (1959).

[27] J. A. Barker, *J. Chem. Phys.*, **70**, 2914 (1979).

[28] D. Chandler and P. G. Wolynes, *J. Chem. Phys*, **74**, 4078 (1981).

[29] E. L. Pollock and D. M. Ceperley, *Phys. Rev. B*, **30**, 2555 (1984).

[30] H. De Raedt and B. De Raedt, *Phys. Rev. A*, **28**, 3575 (1983).

[31] M. Takahashi and M. Imada, *J. Phys. Soc. Jpn.*, **53**, 963 (1984).

[32] M. Takahashi and M. Imada, *J. Phys. Soc. Jpn.*, **53**, 3765 (1984).

[33] X. P. Li and J. Q. Broughton, *J. Chem. Phys*, **86**, 5094 (1987).

[34] Q. Sheng, *IMA Journal of Numerical Analysis*, **9**, 199 (1989).

[35] M. Suzuki, *J. Math. Phys*, **32**, 400 (1991).

[36] S. A. Chin, *Phys. Rev. E*, **73**, 026705 (2006).

[37] F. Casas, *J. Chem. Phys*, **133**, 154114 (2010).

[38] S. R. Scuro and S. A. Chin, *Phys. Rev. E*, **71**, 056703 (2005).

[39] P. J. Reynolds, D. M. Ceperley, B. J. Alder and W. A. Lester, *J. Chem. Phys.*, **77**, 5593 (1982).

[40] D. M. Ceperley, *Phys. Rev. Lett.*, **69**, 331 (1992).

[41] M. Boninsegni, *J. Low Temp. Phys.*, **141**, 27 (2005).

[42] N. V. Prokof'ev, B. V. Svistunov and I. S. Tupitsyn, *Physics Letters A*, **238**, 253 (1998).

[43] S. Pilati, *Studies of ultracold gases using quantum Monte Carlo techniques*, Ph.D. thesis, Università degli studi di Trento (2008).

[44] M. F. Herman, E. J. Bruskin and B. J. Berne, *J. Chem. Phys*, **76**, 5150 (1982).

[45] F. R. Krajewski and M. H. Müser, *Phys. Rev. B*, **65**, 174304 (2002).

[46] A. Leggett, *Physica Fennica*, **8**, 125 (1973).

[47] E. L. Pollock and D. M. Ceperley, *Phys. Rev. B*, **36**, 8343 (1987).

[48] R. Pathria, *Statistical mechanics* (Butterworth-Heinemann, 1996).

[49] R. A. Aziz, F. R. McCourt and C. C. Wong, *Mol. Phys.*, **61**, 1487 (1987).

[50] J. Wilks, *The properties of liquid and solid helium* (Clarendon P., 1967).

[51] R. K. Crawford, in *Rare gas solids* (edited by M. Klein and J. Venables), chap. 11, pp. 663–728 (Academic Press, London, 1977).

[52] E. C. Svensson, V. F. Sears, A. D. B. Woods and P. Martel, *Phys. Rev. B*, **21**, 3638 (1980).

[53] R. J. Donnelly, *Experimental superfluidity* (University of Chicago, 1967).

[54] E. L. Pollock and K. J. Runge, *Phys. Rev. B*, **46**, 3535 (1992).

[55] S. Baroni and S. Moroni, *Phys. Rev. Lett.*, **82**, 4745 (1999).

[56] A. Sarsa, K. E. Schmidt and W. R. Magro, *J. Chem. Phys*, **113**, 1366 (2000).

[57] D. E. Galli and L. Reatto, *Molecular Physics*, **101**, 1697 (2003).

[58] J. E. Cuervo, P.-N. Roy and M. Boninsegni, *J. Chem. Phys*, **122**, 114504 (2005).

[59] M. Rossi, M. Nava, L. Reatto and D. E. Galli, *J. Chem. Phys*, **131**, 154108 (2009).

[60] R. Rota, J. Casulleras, F. Mazzanti and J. Boronat, *Phys. Rev. E*, **81**, 016707 (2010).

[61] J. Casulleras and J. Boronat, *Phys. Rev. B*, **52**, 3654 (1995).

[62] S. Vitiello, K. Runge and M. H. Kalos, *Phys. Rev. Lett.*, **60**, 1970 (1988).

[63] L. Reatto and G. L. Masserini, *Phys. Rev. B*, **38**, 4516 (1988).

[64] S. O. Diallo, J. V. Pearce, R. T. Azuah and H. R. Glyde, *Phys. Rev. Lett.*, **93**, 075301 (2004).

[65] D. E. Galli and L. Reatto, *J. Phys. Soc. Jpn.*, **77**, 111010 (2008).

[66] B. K. Clark and D. M. Ceperley, *Phys. Rev. Lett.*, **96**, 105302 (2006).

[67] D. Tilley, D. Tilley, J. Tilley, J. Tilley and J. Tilley, *Superfluidity and superconductivity*, Graduate student series in physics (Institute of Physics Publishing, 1994).

[68] R. Silver and P. Sokol, *Momentum distributions* (Plenum Press, 1989).

[69] E. C. Svensson and V. F. Sears, in *Frontiers of neutron scattering* (edited by R. Birgenau, D. Moncton and A. Zeilinger), Physica B + C (North-Holland, 1986).

[70] H. R. Glyde, R. T. Azuah and W. G. Stirling, *Phys. Rev. B*, **62**, 14337 (2000).

[71] H. R. Glyde, S. O. Diallo, R. T. Azuah, O. Kirichek and J. W. Taylor, *Phys. Rev. B*, **83**, 100507 (2011).

[72] D. M. Ceperley and E. L. Pollock, *Can. J. Phys.*, **65**, 1416 (1987).

[73] L. Vranješ, J. Boronat, J. Casulleras and C. Cazorla, *Phys. Rev. Lett.*, **95**, 145302 (2005).

[74] E. Manousakis, V. R. Pandharipande and Q. N. Usmani, *Phys. Rev. B*, **31**, 7022 (1985).

[75] R. Rota and J. Boronat, *J. Low Temp. Phys.*, **162**, 146 (2011).

[76] Y. Aoki, J. C. Graves and H. Kojima, *Phys. Rev. Lett.*, **99**, 015301 (2007).

[77] M. Kondo, S. Takada, Y. Shibayama and K. Shirahama, *J. Low Temp. Phys.*, **148**, 695 (2007).

[78] A. S. C. Rittner and J. D. Reppy, *Phys. Rev. Lett.*, **98**, 175302 (2007).

[79] A. Penzev, Y. Yasuta and M. Kubota, *J. Low Temp. Phys.*, **148**, 677 (2007).

[80] A. C. Clark, J. T. West and M. H. W. Chan, *Phys. Rev. Lett.*, **99**, 135302 (2007).

[81] D. M. Ceperley and B. Bernu, *Phys. Rev. Lett.*, **93**, 155303 (2004).

[82] D. E. Galli and L. Reatto, *Phys. Rev. Lett.*, **96**, 165301 (2006).

[83] L. Pollet, M. Boninsegni, A. B. Kuklov, N. V. Prokof'ev, B. V. Svistunov and M. Troyer, *Phys. Rev. Lett.*, **98**, 135301 (2007).

[84] M. Boninsegni, N. Prokof'ev and B. Svistunov, *Phys. Rev. Lett.*, **96**, 105301 (2006).

[85] F. Pederiva, G. V. Chester, S. Fantoni and L. Reatto, *Phys. Rev. B*, **56**, 5909 (1997).

[86] M. Boninsegni, A. B. Kuklov, L. Pollet, N. V. Prokof'ev, B. V. Svistunov and M. Troyer, *Phys. Rev. Lett.*, **97**, 080401 (2006).

[87] B. K. Clark and D. M. Ceperley, *Comput. Phys. Commun.*, **179**, 82 (2008).

[88] C. Cazorla, G. E. Astrakharchik, J. Casulleras and J. Boronat, *New J. Phys.*, **11**, 013047 (2009).

[89] Y. Lutsyshyn, C. Cazorla, G. E. Astrakharchik and J. Boronat, *Phys. Rev. B*, **82**, 180506 (2010).

[90] B. A. Fraass, P. R. Granfors and R. O. Simmons, *Phys. Rev. B*, **39**, 124 (1989).

[91] C. A. Burns and J. M. Goodkind, *J. Low Temp. Phys.*, **95**, 695 (1994).

[92] P. W. Anderson, W. F. Brinkman and D. A. Huse, *Science*, **310**, 1164 (2005).

[93] P. W. Anderson, *Science*, **324**, 631 (2009).

[94] R. Simmons and R. Blasdell, *APS March Meeting* (2007), (unpublished).

[95] M. Rossi, E. Vitali, D. Galli and L. Reatto, *J. Low Temp. Phys.*, **153**, 250 (2008).

[96] R. Pessoa, M. de Koning and S. A. Vitiello, *Phys. Rev. B*, **80**, 172302 (2009).

[97] Y. Lutsyshyn, C. Cazorla and J. Boronat, *J. Low Temp. Phys.*, **158**, 608 (2010).

[98] J. Day and J. Beamish, *Nature*, **450** (2007).

[99] H. Maris and S. Balibar, *J. Low Temp. Phys.*, **162**, 12 (2011).

[100] D. Y. Kim, H. Choi, W. Choi, S. Kwon, E. Kim and H. C. Kim, *Phys. Rev. B*, **83**, 052503 (2011).

[101] E. J. Pratt, B. Hunt, V. Gadagkar, M. Yamashita, M. J. Graf, A. V. Balatsky and J. C. Davis, *Science*, **332**, 821 (2011).

[102] B. Hunt, E. Pratt, V. Gadagkar, M. Yamashita, A. V. Balatsky and J. C. Davis, *Science*, **324**, 632 (2009).

[103] A. Eyal, O. Pelleg, L. Embon and E. Polturak, *Phys. Rev. Lett.*, **105**, 025301 (2010).

[104] T. Markovich, E. Polturak, J. Bossy and E. Farhi, *Phys. Rev. Lett.*, **88**, 195301 (2002).

[105] N. Gov, *Phys. Rev. B*, **67**, 052301 (2003).

[106] J. H. Vignos and H. A. Fairbank, *Phys. Rev. Lett.*, **6**, 265 (1961).

[107] A. F. Schuch and R. L. Mills, *Phys. Rev. Lett.*, **8**, 469 (1962).

[108] E. Grilly and R. Mills, *Ann. Phys.*, **18**, 250 (1962).

[109] D. O. Edwards and R. C. Pandorf, *Phys. Rev.*, **144**, 143 (1966).

[110] J. K. Hoffer, W. R. Gardner, C. G. Waterfield and N. E. Phillips, *J. Low Temp. Phys.*, **23**, 63 (1976).

[111] E. R. Grilly, *J. Low Temp. Phys.*, **11**, 33 (1973).

[112] B. Chaudhuri, F. Pederiva and G. V. Chester, *Phys. Rev. B*, **60**, 3271 (1999).

[113] D. E. Galli, M. Rossi and L. Reatto, *Phys. Rev. B*, **71**, 140506 (2005).

[114] D. M. Ceperley, in *Momentum Distribution* (edited by R. N. Silver and P. E. Sokol), p. 71 (Plenum Press, New York, 1989).

[115] R. C. Blasdell, D. M. Ceperley and R. O. Simmons, *Z. Naturforsch.*, **48a**, 433 (1993).

[116] S. O. Diallo, J. V. Pearce, R. T. Azuah, O. Kirichek, J. W. Taylor and H. R. Glyde, *Phys. Rev. Lett.*, **98**, 205301 (2007).

[117] C. Cazorla and J. Boronat, *J. Phys.: Condensed Matter*, **20**, 015223 (2008).

[118] S. M. Apenko, *Phys. Rev. B*, **60**, 3052 (1999).

[119] H. J. Maris, G. M. Seidel and T. E. Huber, *J. Low Temp. Phys.*, **51**, 471 (1983).

[120] H. J. Maris, G. M. Seidel and F. I. B. Williams, *Phys. Rev. B*, **36**, 6799 (1987).

[121] V. S. Vorob'ev and S. P. Malyshenko, *J. Phys. Condensed Matter*, **12**, 5071 (2000).

[122] R. E. Grisenti, R. A. C. Fraga, N. Petridis, R. Dörner and J. Deppe, *EPL (Europhysics Letters)*, **73**, 540 (2006).

[123] H. Li, R. J. Le Roy, P. N. Roy and A. R. W. McKellar, *Phys. Rev. Lett.*, **105**, 133401 (2010).

[124] K. Kuyanov-Prozument and A. F. Vilesov, *Phys. Rev. Lett.*, **101**, 205301 (2008).

[125] I. F. Silvera, *Rev. Mod. Phys.*, **52**, 393 (1980).

[126] M. C. Gordillo and D. M. Ceperley, *Phys. Rev. Lett.*, **79**, 3010 (1997).

[127] M. Boninsegni, *New J. of Phys.*, **7**, 78 (2005).

[128] Y. Kwon and K. B. Whaley, *Phys. Rev. Lett.*, **89**, 273401 (2002).

[129] F. Paesani, R. E. Zillich, Y. Kwon and K. B. Whaley, *J. Chem. Phys*, **122**, 181106 (2005).

[130] Y. Kwon and K. B. Whaley, *J. Low Temp. Phys.*, **140**, 227 (2005).

[131] P. Sindzingre, D. M. Ceperley and M. L. Klein, *Phys. Rev. Lett.*, **67**, 1871 (1991).

[132] F. Mezzacapo and M. Boninsegni, *Phys. Rev. Lett.*, **97**, 045301 (2006).

[133] F. Mezzacapo and M. Boninsegni, *Phys. Rev. A*, **75**, 033201 (2007).

[134] S. A. Khairallah, M. B. Sevryuk, D. M. Ceperley and J. P. Toennies, *Phys. Rev. Lett.*, **98**, 183401 (2007).

[135] F. Mezzacapo and M. Boninsegni, *Phys. Rev. Lett.*, **100**, 145301 (2008).

[136] I. F. Silvera and V. V. Goldman, *J. Chem. Phys*, **69**, 4209 (1978).

[137] O. Osychenko, R. Rota and J. Boronat, *in preparation.*

[138] N. V. Prokof'ev and B. V. Svistunov, *Phys. Rev. Lett.*, **81**, 2514 (1998).

[139] L. Brualla, *Path Integral Monte Carlo - Algorithms and application to quantum fluids*, Ph.D. thesis, Universitat Politècnica de Catalunya (2002).